

Modeling optical properties of non-cubical sea salt particles

Franz Kanngießer¹ and Michael Kahnert²

¹Chalmers University of Technology

²Swedish Meteorological and Hydrological Institute

November 22, 2022

Abstract

Dried sea salt aerosol is commonly represented in aerosol-optics models by ideal cubical particles, while samples reveal that marine aerosol particles frequently display distorted cubical shapes, and they can have more or less rounded edges. In this study three types of non-ideal cuboidal model geometries are investigated, namely, convex polyhedra, Gaussian random cubes, and superellipsoids. Optical calculations were performed at a wavelength of 532 nm using the discrete dipole approximation and the T-matrix method. The main focus is on optical properties relevant to lidar remote sensing, namely, the linear depolarization ratio in the backscattering direction, and the extinction-to-backscatter or lidar ratio. Gaussian random distortions tend to increase the depolarization ratio in relation to that of perfect cubes, while superellipsoids mimicking cubes with rounded edges generally decrease the depolarization ratio. Convex polyhedra can describe randomly distorted cubes. Their computed depolarisation ratios display random fluctuations about those computed for ideal cubes. The results suggest that Gaussian random cubes and superellipsoids are most consistent with the observations if the geometries deviate only mildly from that of an ideal cube. Gaussian random cubes that strongly diverge from cubical shape pose a risk of overestimating both depolarization and extinction-to-backscatter ratio. Superellipsoids that approach octahedral shape yield unrealistically high depolarization ratios. Investigation of size-averaged optical properties of superellipsoids demonstrate that the presence of absorbing material in marine aerosols can have a dramatic effect on the lidar ratio, and its effect on the depolarization ratio can be of comparable magnitude as that caused by rounding of edges.

Modeling optical properties of non-cubical sea salt particles

Franz Kanngießer¹, Michael Kahnert^{1,2}

¹Department of Space, Earth and Environment, Chalmers University of Technology, SE-416 96
Gothenburg, Sweden

²Research Department, Swedish Meteorological and Hydrological Institute, Folkborgsvägen 17, SE-601 76
Norrköping, Sweden

Key Points:

- The optical properties of dried sea salt aerosol were studied using three different types of model geometries, convex polyhedra, Gaussian random cubes, and superellipsoids.
- Both Gaussian random cubes and superellipsoids were found to provide sufficient flexibility to bring model results in agreement with laboratory measurements of the linear backscatter depolarisation ratio.
- Model geometries strongly deviating from a cubical shape pose the risk of overestimating the linear depolarization ratio and the extinction-to-backscatter ratio.

Corresponding author: F. Kanngießer, franz.kanngiesser@chalmers.se

Abstract

Dried sea salt aerosol is commonly represented in aerosol-optics models by ideal cubical particles, while samples reveal that marine aerosol particles frequently display distorted cubical shapes, and they can have more or less rounded edges. In this study three types of non-ideal cuboidal model geometries are investigated, namely, convex polyhedra, Gaussian random cubes, and superellipsoids. Optical calculations were performed at a wavelength of 532 nm using the discrete dipole approximation and the T-matrix method. The main focus is on optical properties relevant to lidar remote sensing, namely, the linear depolarization ratio in the backscattering direction, and the extinction-to-backscatter or lidar ratio. Gaussian random distortions tend to increase the depolarization ratio in relation to that of perfect cubes, while superellipsoids mimicking cubes with rounded edges generally decrease the depolarization ratio. Convex polyhedra can describe randomly distorted cubes. Their computed depolarisation ratios display random fluctuations about those computed for ideal cubes. The results suggest that Gaussian random cubes and superellipsoids are most consistent with the observations if the geometries deviate only mildly from that of an ideal cube. Gaussian random cubes that strongly diverge from cubical shape pose a risk of overestimating both depolarization and extinction-to-backscatter ratio. Superellipsoids that approach octahedral shape yield unrealistically high depolarization ratios. Investigation of size-averaged optical properties of superellipsoids demonstrate that the presence of absorbing material in marine aerosols can have a dramatic effect on the lidar ratio, and its effect on the depolarization ratio can be of comparable magnitude as that caused by rounding of edges.

1 Introduction

Marine aerosol is one of the most abundant aerosol types in the atmosphere (Boucher, 2015). It consists mainly of more or less hydrated sea salt particles as well as biological material (Boucher, 2015; Patterson et al., 2016; Zieger et al., 2017). The aerosol is emitted into the atmosphere by bursting air bubbles in the oceans and by wind tearing off wave crests (Boucher, 2015). Sea water (e.g. Wells, 2011) contains a mixture of different salts in solution, with sodium chloride being the largest salt component. As a consequence sea salt aerosol particles consist of a mixture of different salts, which is dominated by sodium chloride (NaCl) (Pósfai et al., 1995; Tang et al., 1997; Irshad et al., 2009; King et al., 2012; Ueda et al., 2014; Chi et al., 2015).

Marine aerosol provides large surface areas for heterogeneous chemical reactions. It further influences the climate both directly and indirectly, namely, by directly scattering radiation (Murphy et al., 1998; Buseck & Pósfai, 1999; King et al., 2012), and by acting as cloud condensation nuclei, hence impacting cloud reflectivity and precipitation (Boucher, 2015). Furthermore, sea salt aerosol plays an important role in corrosion processes of metals and reinforced concrete structures in coastal areas (Meira et al., 2008).

Large-scale transport models typically contain sea-salt modules that describe the generation, hydration or dehydration, transport, and deposition of marine aerosol (e.g. Foltescu et al., 2005). Evaluation of such models requires the use of long-term data sets with global coverage, which can be obtained from remote sensing observations. The analyses of remote sensing observations, in turn, requires a thorough understanding of the connection between aerosol microphysical properties and optical properties.

Especially in the tropics crystalline sea salt aerosol can play a significant role. The tropical troposphere is commonly characterised by the trade wind inversion, which has a lower boundary within the lowest two kilometres. Please note, that the trade wind inversion does not necessarily coincide with the top of the atmospheric boundary layer, as discussed by Carrillo et al. (2016) and references therein. Within this inversion layer the moisture content rapidly decreases, so that the troposphere above that inversion layer is extremely dry (Krishnamurti et al., 2013). Aerosol lifted into or above the inversion

68 layer dries out; as a consequence, sea salt aerosol particles may crystallise as proposed
 69 in (Haarig et al., 2017). But even measurements performed in extra-tropical latitudes
 70 indicate the potential presence of dried sea salt aerosol (Sakai et al., 2000).

71 Dried sea salt particles come in cubical or cuboidal shapes, or in shapes deviating
 72 slightly from such a reference shape, as images of particle samples indicate (Peart & Evans,
 73 2011; Gwaze et al., 2007; Patterson et al., 2016; King et al., 2012; Zeng et al., 2013; McInnes
 74 et al., 1994). Measurements of the dynamic shape factor of artificial sea salt, reported
 75 by Zieger et al. (2017), indicate aspherical, cube-like shapes. Less common are irregu-
 76 lar shapes, which were reported in (Sakai et al., 2010; Peart & Evans, 2011; Zeng et al.,
 77 2013). The shape of salt crystals differs for different salts (Pósfai et al., 1995; Wise et
 78 al., 2005). In case of mixtures, such as sea salt, already small amounts of non-NaCl com-
 79 ponents can alter the shape of the sea salt aerosol particles compared to pure NaCl crys-
 80 tals (Zieger et al., 2017). Thus the chemical composition of sea salt aerosol particles in-
 81 fluences both the particle shape and the dielectrical properties, both of which impact the
 82 optical properties.

83 The optical properties, and more specifically the linear depolarization ratio of sea
 84 salt aerosol particles have previously been measured in laboratory studies and during li-
 85 dar field observations. Lab measurements of the linear depolarization ratio in the near-
 86 backscattering direction of pure NaCl crystals yielded values of $\delta_{l,179^\circ} = 21\%$ at 532
 87 nm wavelength (Sakai et al., 2010), and $\delta_{l,178^\circ} \approx 25\%$ at 488 nm (Järvinen et al., 2016).
 88 For crystalline sea salt at 532 nm a value of $\delta_{l,179^\circ} = 8\%$ was reported (Sakai et al., 2010).
 89 Further, the depolarization ratio is dependent on the relative humidity (RH) of the am-
 90 bient air. At 632.8 nm values of δ_l ranging from 5.6–11.1% for $77\% < RH < 92\%$ and
 91 $\delta_l \approx 20\%$ for $RH < 12\%$ for NaCl particles in a lab environment have been reported
 92 in the near-backscattering direction, i.e. $\vartheta > 177^\circ$ (Cooper et al., 1974).

93 While there are various lidar field observations of marine or sea salt aerosol, there
 94 are only a limited number of reported measurements of the linear depolarization ratio
 95 in combination with reported values of the relative humidity. The combination of mea-
 96 suring the linear depolarization ratio of marine aerosol particles and the relative humid-
 97 ity in the same layer can indicate the presence of dried sea salt aerosol particles. In Ta-
 98 ble 1 values of linear depolarization ratio and extinction-to-backscatter ratio at 532 nm
 99 obtained from lidar field measurements of dried marine aerosol are shown. The classi-
 100 fication as marine aerosol is taken from each reference and usually based on backward
 101 trajectory analyses.

102 Sea salt aerosol particles grow with increasing relative humidity by water vapour
 103 condensing onto the crystal (Shettle & Fenn, 1979). The crystal gets increasingly dis-
 104 solved by the condensed water. If the deliquescence point, which for sea salt crystals is
 105 at a relative humidity of approximately 70–74% (Tang et al., 1997; Zieger et al., 2017),
 106 is reached, the salt crystal becomes fully dissolved in a liquid droplet. A liquid droplet
 107 containing dissolved sea salt remains liquid until the relative humidity is below 45–50% (Tang
 108 et al., 1997; Zieger et al., 2017), at which point the salt recrystallises. Between values
 109 of the relative humidity of ~ 50 and $\sim 70\%$ both crystalline, aspherical and dissolved,
 110 spherical sea salt aerosol particles may coexist as a consequence of this hysteresis effect.
 111 Therefore, aerosol layers with reported values of relative humidity below 50% (Zieger et
 112 al., 2017) are considered to be dried and hence crystalline.

113 The values reported by Sakai et al. (2000) should be taken with a grain of salt, as
 114 they can be partially contaminated by continental aerosol particles. For the measure-
 115 ments conducted on the Atlantic Ocean near Cape Town (Bohlmann et al., 2018) two
 116 values of RH were reported. The value of $RH \approx 50\%$ was obtained by a radiosonde and
 117 the value of $RH < 40\%$ was taken from the Global Data Assimilation System (GDAS1).
 118 Values of δ_l up to 11% for marine aerosol as reported by Groß et al. (2013) indicate the
 119 presence of dried sea salt particles, however the lack of reported RH measurements makes

Table 1. Depolarization ratios and extinction-to-backscatter ratios of dried sea salt aerosol particles from lidar measurements at 532 nm and the corresponding relative humidity (RH) of the aerosol layer

location	δ_l (%)	S_p (sr)	RH	reference
Husbands, Barbados	14.8 ± 3.5	25 ± 3	40%	(Haarig et al., 2017)
Atlantic Ocean (near Cape Town)	9	13 ± 3	< 40% (50%)	(Bohmann et al., 2018)
Atlantic Ocean (west of Western Sahara)	8	–	~10%	(Yin et al., 2019)
Tokyo, Japan	10	–	< 50%	(Murayama et al., 1999)
Hagoya, Japan	10 – 20	–	25 – 45%	(Sakai et al., 2000)

120 it difficult to assess this. For a relative humidity of $RH > 80\%$ values of the linear de-
 121 polarization ratio of 6–7% were reported by Sakai et al. (2012). Based on these field
 122 observations as well as the laboratory experiments linear depolarization ratios of up to
 123 20–25% and extinction-to-scatter ratios of up to 25 sr particles can be considered plau-
 124 sible for dried (sea) salt aerosol.

125 Compared to mineral dust and soot aerosol (see e.g. the studies by Nousiainen and
 126 Kandler (2015); Kahnert and Kanngießer (2020) and references therein) the approaches
 127 to modeling optical properties of sea salt particles are less studied. Sea salt aerosol par-
 128 ticles have been modeled by using spheres (Chamailard et al., 2006) and cubes (Murayama
 129 et al., 1999; Chamailard et al., 2006; Sakai et al., 2010; David et al., 2013; Haarig et al.,
 130 2017). In (Adachi & Buseck, 2015) spheres, cubes, and elongated and flattened cuboids
 131 are use as model particles to assess effects on light scattering. In order to model depo-
 132 larization ratios, cubes were used by Murayama et al. (1999); Sakai et al. (2010); David
 133 et al. (2013); Haarig et al. (2017). (Bi, Lin, Wang, et al., 2018) demonstrated the ap-
 134 plicability of superellipsoids to model the depolarization of sea salt aerosol particles. In
 135 that study superellipsoids resembling rounded cubes, spheres, and rounded octahedra
 136 as well as distortions of these base solids by changing the aspect ratio were considered.
 137 Sea salt aerosol with a water coating was investigated in regard to the depolarization ra-
 138 tio (Bi, Lin, Wang, et al., 2018), and in regard to the impact on radiative forcing (Wang
 139 et al., 2019).

140 The values of the near-backscattering linear depolarization ratio for pure, crystalline
 141 NaCl reported from laboratory measurements by Cooper et al. (1974); Sakai et al. (2010);
 142 Järvinen et al. (2016) (note, that the measurements by Cooper et al. (1974); Järvinen
 143 et al. (2016) were not performed at $\lambda = 532$ nm) are larger than the depolarization ra-
 144 tio for crystalline sea salt, as reported from both laboratory measurements (Sakai et al.,
 145 2010) and from most lidar field observations listed in Tab. 1. The images of the salt par-
 146 ticles, analysed by Sakai et al. (2010), indicate, that sea salt particles have an irregular,
 147 non-cubical shape, whereas pure NaCl particles have regular geometries with sharper edges.
 148 The laboratory measurements for pure NaCl with a mode radius of $r = 0.12 \mu\text{m}$ could
 149 be reproduced using cubes with an effective radius of $r_{eff} = 0.5 \mu\text{m}$ (Sakai et al., 2010).
 150 By modeling size averaged linear depolarization ratio, it was found, that cubes, follow-
 151 ing the same size distribution as the measurements, underestimate the measured depo-
 152 larization ratio (Bi, Lin, Wang, et al., 2018) by about a factor of 2.

153 Here the impact of sharp edges and shape distortions on the backscatter linear de-
 154 polarization ratio and the extinction-to-backscatter ratio (or lidar ratio) of sea salt aerosol
 155 particles are investigated. To our knowledge the impact of morphological changes of sea
 156 salt particles on the extinction-to-backscatter ratio has not yet been studied.

2 Particle geometries

We want to study to what extent deviations from an ideal cubical shape impact the optical properties. To this end, we perform light-scattering computations for ideal cubes, convex polyhedra, Gaussian random cubes, and superellipsoids. In the latter case, we consider both a cubical and an octahedral reference shape.

2.1 Convex polyhedra

Based on irregularly shaped dust model particles used for radiative forcing calculations by Torge et al. (2011), convex polyhedra were created. N_c points were randomly placed in a Cartesian coordinate system, and around these points a convex hull is placed. This results in an irregular shape with a surface composed of plane faces. The convex hull is constructed using the quickhull algorithm (Barber et al., 1996) as implemented in the SciPy library for Python (Virtanen et al., 2020). As the points are randomly placed in a Cartesian coordinate system the shape of the convex polyhedron converges to a cubical shape for a sufficiently large number of points N_c . Here $N_c = 10$, $N_c = 100$, and $N_c = 1000$ were used. For each value of N_c five different particle realisations were constructed to capture the variability associated with the random placement of the N_c points, when creating the convex polyhedra. Strictly speaking shapes like cubes or octahedra are convex polyhedra, too. For brevity we use the term "convex polyhedra" to refer to the irregular convex polyhedra, which are neither cubical, nor octahedral.

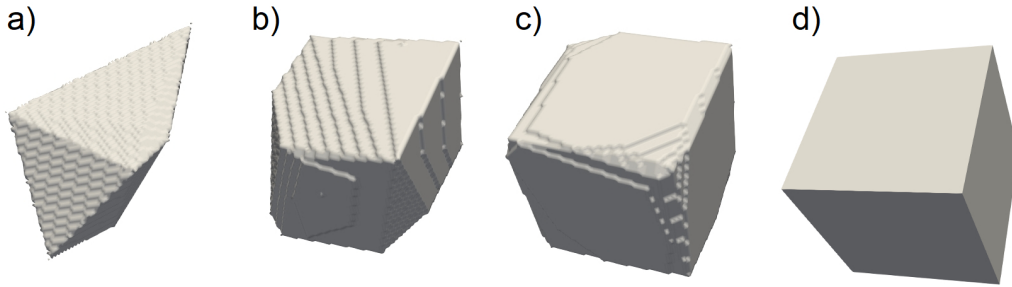


Figure 1. Convex polyhedra with different number of points included in the convex hull N (a–c) and a cube for comparison (d). The number of points increases from left to right: $N_c = 10$ (a), $N_c = 100$ (b) and $N_c = 1000$ (c). The cube corresponds to $N_c \rightarrow \infty$

Figure 1 shows examples for such convex polyhedra with a different number of points inside the convex hull. The number of points inside the convex hulls are 10 (Fig. 1a), 100 (Fig. 1b), and 1000 (Fig. 1c). With growing number of points the shape increasingly resembles a cube. For comparison Fig. 1d shows a cube, which corresponds to $N_c \rightarrow \infty$.

2.2 Gaussian random cubes

By Gaussian random cubes we refer to shapes obtained by superimposing Gaussian random perturbations onto a cube using a modified version of the G-sphere algorithm (Muinonen et al., 1996). The Gaussian random perturbations are described by two different parameters, the relative radial standard deviation σ_r , which determines the magnitude of the perturbations, and the correlation angle Γ , which determines the angular scale of the fluctuations. The smaller Γ , the larger the angular frequency of the random

188 surface perturbations (Muinonen et al., 1996). More specifically, given a surface param-
 189 eterisation $r_{\text{cube}}(\theta, \phi)$ of the surface of a cube in spherical coordinates, and given the sur-
 190 face parameterisation $r_{\text{GRS}}(\sigma_r, \Gamma; \theta, \phi)$ of a *unit* Gaussian random sphere with radial rel-
 191 ative standard deviation σ_r and correlation angle Γ (Muinonen et al., 1996), we define
 192 the surface parameterisation $r(\theta, \phi)$ of the Gaussian random cube by

$$193 \quad r(\theta, \phi) = r_{\text{cube}}(\theta) \cdot r_{\text{GRS}}(\sigma_r, \Gamma; \theta, \phi). \quad (1)$$

194 For the radial standard deviation of the perturbations we chose $\sigma_r = 0.05, 0.1, 0.15,$
 195 $0.2,$ and for the correlation angle $\Gamma = 10^\circ, 20^\circ, 30^\circ,$ and 90° . For each of the configu-
 196 rations five different stochastic realisations were created to capture the variation due to
 197 the random nature of the perturbations. The chosen values were based on the theoret-
 198 ical study on Gaussian random spheres by Muinonen et al. (1996).

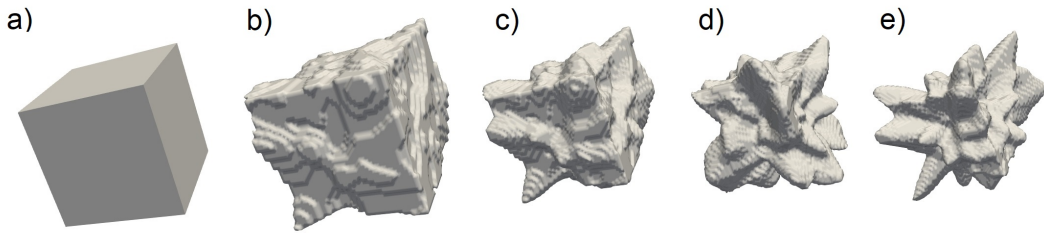


Figure 2. Example of Gaussian random cubes with $\Gamma = 10^\circ$ and increasing radial standard deviation σ_r . b) $\sigma_r = 0.05$, c) $\sigma_r = 0.1$, d) $\sigma_r = 0.15$, and e) $\sigma_r = 0.2$ compared to a cube (a)

199 Figure 2 shows Gaussian random cubes with a fixed correlation angle $\Gamma = 10^\circ$ (b
 200 – e) and a cube (a) for comparison. The relative standard deviation of the radius increases
 201 by steps of $\Delta\sigma_r = 0.05$ from $\sigma_r = 0.05$ (b) to $\sigma_r = 0.2$ (e).

202 Comparing with reported images of dried sea salt aerosol (McInnes et al., 1994; Gwaze
 203 et al., 2007; Sakai et al., 2010; Peart & Evans, 2011; King et al., 2012; Zeng et al., 2013;
 204 Patterson et al., 2016; Sakai et al., 2010) radial standard deviations of $\sigma_r > 0.1$ appear
 205 not to be representative of typical atmospheric and laboratory samples. Nevertheless,
 206 we include these values here to study the effect of more extreme deviations from cubi-
 207 cal shape.

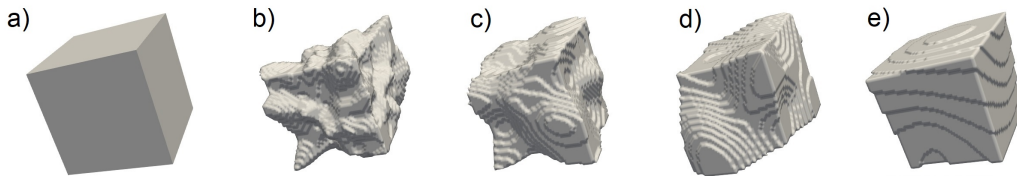


Figure 3. Example of Gaussian random cube with $\sigma_r = 0.1$ and increasing correlation angle Γ . b) $\Gamma = 10^\circ$, c) $\Gamma = 20^\circ$, d) $\Gamma = 30^\circ$, and e) $\Gamma = 90^\circ$ compared to a cube (a)

208 Figure 3 is analogous to Fig. 2, but showing different values of the correlation angle
 209 Γ at a fixed radial standard deviation $\sigma_r = 0.1$ (b–e). The correlation angle is $\Gamma =$
 210 10° (b), $\Gamma = 20^\circ$ (c), $\Gamma = 30^\circ$ (d), and $\Gamma = 90^\circ$ (e).

211

2.3 Superellipsoids

212

213

214

215

216

217

218

219

Superellipsoids are three dimensional shapes represented by the product super-quadratic curves and can be considered generalisations of ellipsoids (Barr, 1981; Wriedt, 2002). The suitability of superellipsoids for modeling depolarization ratios of mineral dust (Bi, Lin, Liu, & Zhang, 2018) and sea salt aerosol (Bi, Lin, Wang, et al., 2018) were previously demonstrated. Various different solids ranging from cuboids, cylinders, spheres to octahedra can be obtained as realisations of superellipsoids (for examples see (Wriedt, 2002)). The superellipsoidal equation for a Cartesian coordinate system with coordinates x , y , and z is (Barr, 1981; Wriedt, 2002)

220

$$\left[\left(\frac{x}{a} \right)^{\frac{2}{e}} + \left(\frac{y}{b} \right)^{\frac{2}{e}} \right]^{\frac{e}{n}} + \left(\frac{z}{c} \right)^{\frac{2}{n}} = 1 \quad (2)$$

221

222

223

224

225

226

The particle's extent along the three Cartesian axes x , y and z is determined by a , b , and c , respectively. n and e are the roundness parameters in north-south (or polar) and east-west (or azimuthal) direction, respectively, which specify the shape. Variation of n and e allows for flexible modeling of a particle's roundness. Here we follow the approach in (Bi, Lin, Liu, & Zhang, 2018; Bi, Lin, Wang, et al., 2018) by assuming $a = b$ and $n = e$.

227

228

229

230

231

232

233

234

235

To investigate the impact of sharp edges we consider a cube (corresponding to $n = 0$) and slightly rounded cubes ($n = 0.1$ and $n = 0.2$), as well as an octahedron ($n = 2.0$) and rounded octahedra ($n = 1.9$ and $n = 1.8$). A spheroid would have a roundness parameter of $n = e = 1$. The aspect ratio was assumed to be 1, i.e., $a = c$. The superellipsoids used for modeling are shown in Fig. 4. The cube and the rounded cubes are shown in the top row (a-c) and the octahedron and the rounded octahedra are shown the the bottom row (d-f). In both rows the roundness increases from left to right. The sharp-edged shapes are in the left column (a,d), the middle column (b,e) and the right column (c,f) show shapes with slightly rounded shapes.

236

2.4 Size distribution of marine aerosol

237

238

239

240

241

242

243

We investigate most optical properties for randomly oriented particles of a definite size. However, atmospheric aerosol particles are typically distributed over a range of sizes. The computation of size-averaged optical properties can become very time consuming. For this reason, we limit our investigation of size-averaged optical properties to cube-like superellipsoids with $e = n = 0, 0.1, \text{ and } 0.2$. For these geometries we can employ the T-matrix method, which is faster than the DDA, but much more limited in the range of possible particle shapes.

244

We use two different types of size distributions.

245

1. We consider a monomodal log-normal size distribution

246

$$n_{\text{mono}}(r_{ve}; N, r_0, \sigma_n) = \frac{N}{r_{ve} \ln \sigma_n \sqrt{2\pi}} \exp \left[-\frac{\ln^2(r_{ve}/r_0)}{2 \ln^2 \sigma_n} \right], \quad (3)$$

247

248

249

250

251

252

253

254

where N is the particle number density, n describes the number of particles per volume element per size interval, r_{ve} is the volume-equivalent radius of the particles, r_0 is the median radius, and σ_n represents the geometric standard deviation. In our calculations we use $\sigma_n = 1.5$ and $r_0 = 0.1, 0.2, \dots, 1.5 \mu\text{m}$. Size averaging of the optical properties involves integration of the scattering matrix elements, weighted by the scattering cross section and the size distribution. Numerically, we perform the integration by use of 146 equally spaced particle sizes $0.050, 0.067, \dots, 2.509 \mu\text{m}$.

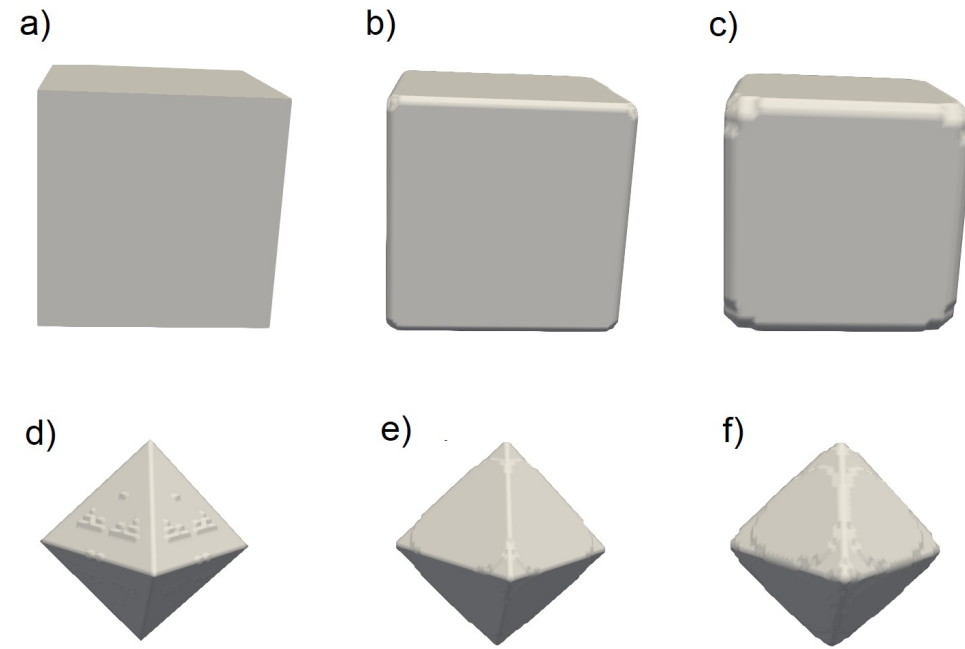


Figure 4. Examples of cube-like superellipsoids (top row) and octahedron-like superellipsoids (bottom row). The roundness increases from left to right. a) and d) show sharp-edged geometries with $n = 0$ and $n = 2$, respectively. b) and c) show geometries with $n = 0.1$, and $n = 1.9$, respectively; and c) and f) show geometries with $n = 0.2$, and $n = 1.8$.

2. Marine aerosol are often best described by a bimodal size distribution. Thus, as a more realistic case, we consider a bimodal log-normal size distribution given by

$$n_{\text{bimodal}}(r_{ve}; N_1, r_{0,1}, \sigma_{n,1}, N_2, r_{0,2}, \sigma_{n,2}) = n_{\text{mono}}(r_{ve}; N_1, r_{0,1}, \sigma_{n,1}) + n_{\text{mono}}(r_{ve}; N_2, r_{0,2}, \sigma_{n,2}). \quad (4)$$

For the median radii, geometric standard deviations, and number densities in each mode we use twelve different combinations of parameters given in Table 2 in the study by Porter and Clarke (1997). They are based on observations in the marine boundary layer at winds speed varying between 0.4 to more than 33 m/s. Note, however, that marine aerosol populations at high wind speeds would contain considerable number densities of coarse aerosol. We are limited by computational constraints to particles radii not exceeding $2.509\mu\text{m}$. Thus our computation cannot be regarded as covering a similar range of wind speeds as the size distributions given by Porter and Clarke (1997).

For either size distribution, we present the size-averaged optical properties as functions of the effective radius

$$r_{\text{eff}} = \frac{\int_0^\infty n(r_{ve}) r_{ve} \pi r_{ve}^2 dr_{ve}}{\int_0^\infty n(r_{ve}) \pi r_{ve}^2 dr_{ve}}, \quad (5)$$

where n denotes either the monomodal or the bimodal log-normal size distribution. Thus the effective radius represents the ratio of the third and the second moment of the size distribution. It is a quantity frequently employed for characterising the size of polydisperse particles in light-scattering processes (e.g. (Mishchenko et al., 2002)).

3 Optical modeling

The optical calculations were performed for a wavelength of 532 nm. This is the second harmonic of neodymium-doped yttrium aluminium garnett (Nd:YAG) lasers, which are commonly used in lidar instruments (Wandinger, 2005; Eloranta, 2005).

The refractive index of NaCl as given by Eldridge and Palik (1997) was used in this study, as sea salt is dominated by sodium chloride. Thus we assume $m = 1.5484 + i0$. Note that the imaginary part of the refractive index is zero, i.e., the particles are assumed to be non-absorbing.

(Hänel, 1976) reported slightly different values for dried marine aerosol ($m = 1.55 + i0.059$) and dried sea spray aerosol ($m = 1.55 + i0$). Since Hänel (1976) reported values not directly at $\lambda = 0.532 \mu\text{m}$, the values given here were obtained from linear interpolation. The latter value underscores that the refractive index of NaCl closely agrees with that of sea salt aerosol. In addition to the chemical composition of the dry sea salt the refractive index of sea salt aerosol has a weak dependence on the relative humidity (Shettle & Fenn, 1979; Cotterell et al., 2017).

The calculations were performed at three different volume-equivalent radii $r_{ve} = 0.25 \mu\text{m}$, $0.5 \mu\text{m}$, and $1.0 \mu\text{m}$. This covers a large part of the typical size range for this kind of aerosol, although particles up to radii of $5 \mu\text{m}$ are not uncommon. However, the upper end of our size range is constrained by computational capabilities of light-scattering software.

Optical calculations for all particle geometries were performed using the discrete dipole approximation (DDA) code ADDA (Yurkin & Hoekstra, 2007, 2011). The DDA can treat arbitrary geometries, as the scatterer is divided into multiple, fully polarisable volume-elements called dipoles, which are much smaller than the wavelength. The dipoles interact with each other and the incident field, resulting in a set of linear equations, which are solved using standard numerical methods. As a consequence of dividing the scatterer into fully polarisable dipoles arbitrary geometries and inhomogeneous scatterers can be treated.

We also performed T-matrix calculations on superellipsoids. We employed the Tsym code (Kahnert, 2013). This code is highly efficient for particles with discrete symmetries, such as superellipsoids, as it makes use of commutation relations (Schulz et al., 1999) and irreducible representations (Kahnert, 2005) of finite symmetry groups. Here, we extended the Tsym version described by Kahnert (2013) by including the surface parameterisation of superellipsoids into the code. The details are described in the appendix. The Tsym computations serve two main purposes. (i) We employ the T-matrix results for comparison with DDA computations (see below). (ii) DDA computations are prohibitively time consuming for computing optical properties for an entire size distribution. For this reason, we employ the T-matrix method for investigating size-averaged optical properties of superellipsoids (see Sec. 2.4).

The light scattering computations give out the optical cross sections and the full scattering matrix, from which other optical parameters can be calculated. For instance, the extinction-to-backscatter ratio S_p , which, in the context of lidar remote sensing, is frequently referred to as the lidar ratio, can be calculated for a distinct particle size r as (Gasteiger et al., 2011)

$$S_p(r) = 4\pi \frac{C_{\text{ext}}(r)}{C_{\text{sca}}(r)F_{11}(r)} \Big|_{\vartheta=180^\circ} \quad (6)$$

C_{ext} is the particle's extinction cross section, C_{sca} the particle's scattering cross section, and F_{11} denotes the phase function, which is the (11) element of the normalised Stokes scattering matrix.

323 The linear backscattering depolarization ratio can be calculated by (Mishchenko
324 & Hovenier, 1995):

$$325 \quad \delta_l = \frac{F_{11} - F_{22}}{F_{11} + F_{22}} \Big|_{\vartheta=180^\circ}, \quad (7)$$

326 where F_{22} denotes the (22) element of the normalised Stokes scattering matrix, and ϑ
327 represents the scattering angle. The expression is evaluated in the backscattering direc-
328 tion ($\vartheta = 180^\circ$).

329 The discrete dipole approximation is derived from the volume-integral equation of
330 electromagnetic scattering under the assumption that the volume elements are much smaller
331 than the wavelength of light. Thus, the dipole spacing is the main parameter that con-
332 trols the numerical accuracy of the results. To estimate the related numerical uncertainty,
333 the dipole spacing for a superellipsoid with $r_{ve} = 0.5 \mu\text{m}$ and $n = e = 0.2$ is varied.
334 In the ADDA code we express the dipole spacing as dipoles per wavelength (dpl). The
335 larger we set the value of dpl, the finer the dipole grid.

336 Another measure to control the dipole spacing is $|m|kd$, with m being the complex
337 refractive index of the scatterer, $k = 2\pi/\lambda$ the wavenumber in vacuum, and d the dipole
338 spacing. dpl and $|m|kd$ can be converted into each other by $|m|kd = 2|m|\pi/dpl$ (Yurkin
339 et al., 2006).

340 To estimate the impact of the dipole spacing, calculations for a superellipsoid with
341 a roundness parameter $n = e = 0.2$ (i.e., a lightly rounded cube) were performed with
342 different dipole spacing ranging between $dpl = 19$ and $dpl = 160$; the results were com-
343 pared to T-matrix calculations. The (11), (22), and (12) elements for such a superellip-
344 soid with four different dipole spacings are shown in Fig. 5. The rather coarse dipole spac-
345 ing of $dpl = 19$ is indicated in dark blue, $dpl = 42$ is depicted by the green line, $dpl =$
346 92 in purple, and the finest dipole spacing of $dpl = 160$ is represented by the yellow line.
347 The T-matrix results are shown by the light-blue line.

348 The (11) element of the Stokes scattering matrix shows only comparatively little
349 variation with changing dipole spacing. The different lines for the F_{11} elements are nearly
350 indistinguishable by visual inspection. The (12) and (22) element of the Stokes scatter-
351 ing matrix converge toward the T-matrix results with increasing dpl . However, the vari-
352 ation of the DDA results with dpl is rather weak. For instance, the 12 and 22 elements
353 for $dpl = 92$ (purple) are hardly distinguishable from $dpl = 160$ (yellow), or from the
354 T-matrix results (light blue).

355 Figure 6 shows the extinction-to-backscatter ratio S_p (top panel) and the linear de-
356 polarization ratio δ_l (bottom panel) of a superellipsoid with $n = e = 0.2$ and $r_{ve} =$
357 $0.5 \mu\text{m}$ as a function of dipoles per wavelength. The last value, which is separated by the
358 vertical black line from the previous values, shows the T-matrix results. To highlight the
359 changes with increasing dpl, the y-axes in Fig. 6 do not start at zero. Both extinction-
360 to-backscatter ratio and linear depolarization ratio show a weak dependence on the dipole
361 spacing. The extinction-to-backscatter ratio converges with increasing dpl to the T-matrix
362 result. In case of the depolarization ratio the values from the DDA calculations converge
363 more slowly towards the T-matrix result. The values cover a range less than 1 sr in case
364 of S_p and less than 0.015 in case of δ_l . This small variation is in line with the rather small
365 effect of the dipole spacing on the scattering matrix elements.

366 In order to not overly increase the computational burden we chose a dipole spac-
367 ing corresponding to $|m|kd \leq 0.4$, or $dpl \geq 25$ respectively. As a consequence differ-
368 ences smaller than $\Delta\delta_l = 0.015$ and $\Delta S_p = 1$ sr, respectively, cannot be distinguished
369 from artefacts due to dipole spacing. The calculations were performed assuming totally
370 random orientations, by averaging over 1024 different orientations. The orientational av-
371 eraging is performed internally within ADDA.

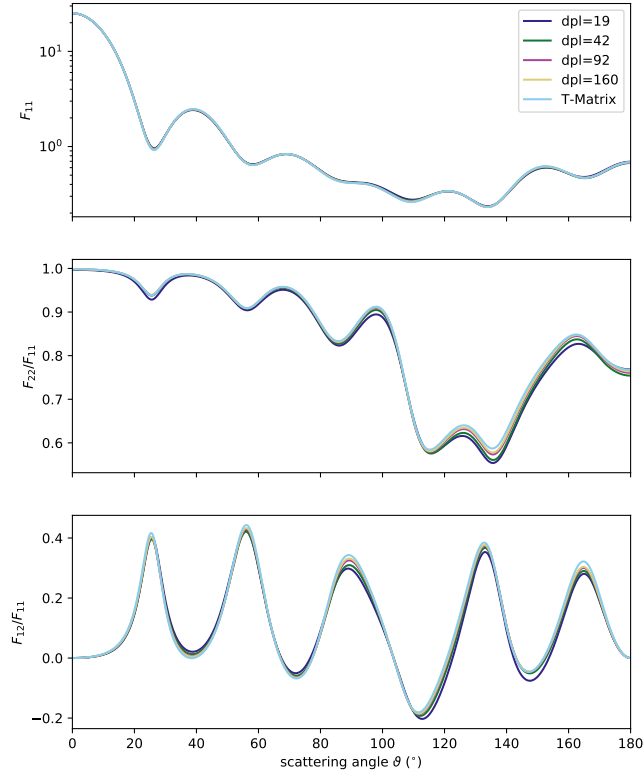


Figure 5. F_{11} (top), F_{22}/F_{11} (middle), and F_{12}/F_{11} (bottom) for different dipole spacing, expressed as dipoles per wavelength dpl ; $dpl = 19$ in dark blue, $dpl = 42$ in green, $dpl = 92$ in purple, and $dpl = 160$ in yellow. The light-blue line indicates the Matrix elements obtained from T-matrix calculations.

4 Results

4.1 Convex Polyhedra

The ensemble-averaged (11), (22), and (12) elements of the normalised scattering matrix for the different convex polyhedra are shown in Fig. 7. The rows correspond to the matrix elements and the columns to the different volume-equivalent radii. The matrix elements for convex polyhedra based on $N_c = 10$ randomly placed points are shown in dark blue, for shapes with $N_c = 100$ in green, $N_c = 1000$ and for a cube, which corresponds to $N \rightarrow \infty$ in cyan.

The values of both the convex polyhedra with $N_c = 100$ and $N_c = 1000$ are close to the values from the cubes ($N_c \rightarrow \infty$), whereas the values for $N_c = 10$ deviate more strongly from the values for the cubes. As the example geometries shown in Fig. 1 indicate, the solids with $N_c = 10$ deviate most from a cubical shape.

Figure 8 shows the size-dependent backscattering cross section C_{bak} , extinction-to-backscatter ratio S_p , and linear backscattering depolarization ratio δ_l for convex poly-

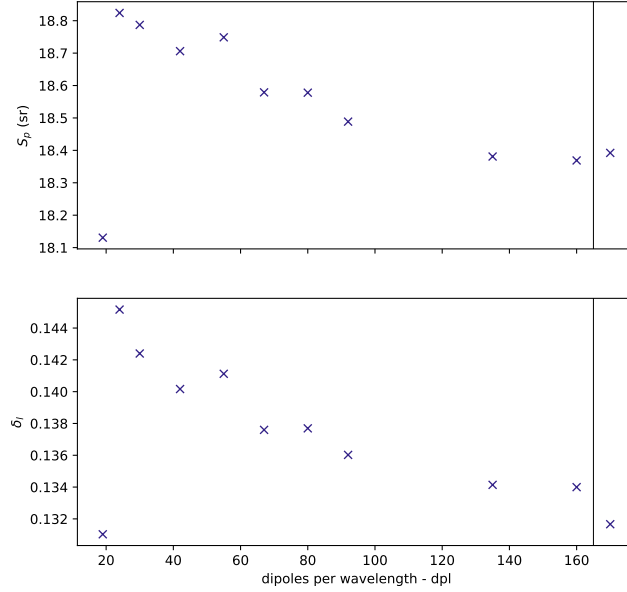


Figure 6. Extinction-to-backscatter ratio (S_p , top panel) and linear depolarization ratio (δ_l , bottom panel) of a superellipsoid with $n = e = 0.2$ and a volume-equivalent radius of $r_{ve} = 0.5 \mu\text{m}$ at $\lambda = 0.532 \mu\text{m}$ as a function of dipoles per wavelength (dpl). Note the different scales of the y-axes.

386 hedra with $N_c = 10$ (dark-blue), $N_c = 100$ (green), $N_c = 1000$ (purple), and $N \rightarrow \infty$
 387 (cyan), which is represented by a cube. With the exception of the cube, the crosses de-
 388 note the arithmetic mean over five different geometric realisations, and the bars indicate
 389 the range between the maximum and minimum of each quantity in the ensemble. To al-
 390 low for an easier visual inspection the points in Fig. 8, as well as in Figs. 12, and 14 are
 391 slightly shifted with respect to the x-axis. With increasing number of points, the vari-
 392 ation in the backscattering cross section and in the extinction-to-backscatter ratio is re-
 393 duced, so that for $N_c = 1000$ the spread in the ensemble is very small. However, this
 394 does not hold for δ_l , for which the range for $N_c = 100$ with $r_{ve} > 0.5 \mu\text{m}$ is larger than
 395 the range for $N_c = 10$. Possibly five different stochastic realisations per N_c do not suf-
 396 ficiently sample from the variety of possible shapes for $N_c = 10$ and hence potentially
 397 underestimate the full range of possible values.

398 The larger deviations in the F_{22} -element in backscattering direction for $N_c = 10$
 399 compared to the cube ($N \rightarrow \infty$), especially for $r_{ve} = 0.5 \mu\text{m}$ and $r_{ve} = 1.0 \mu\text{m}$, are
 400 mirrored in the comparatively large differences in the linear depolarization ratio. Com-
 401 pared to the cubical shape the convex polyhedra with $N_c = 10$ give consistently higher
 402 δ_l values. For instance, for $r_{ve} = 1 \mu\text{m}$, the depolarization ratio modeled with the con-
 403 vex particles with $N_c = 10$ is around 0.45, which is about twice as high as that obtained
 404 with $N_c \geq 100$.

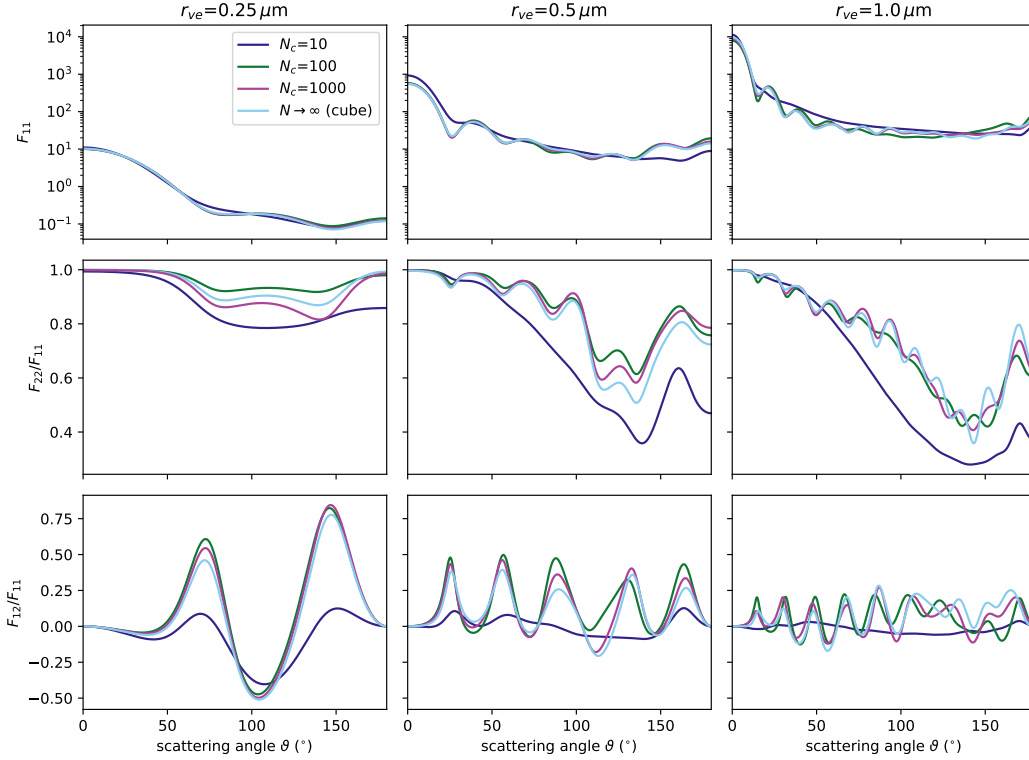


Figure 7. (11), (22), and (12) elements of the normalised scattering matrix for convex polyhedral shapes with $N_c = 10$ (dark blue), $N_c = 100$ (green), $N_c = 1000$ (purple), and for a cube, corresponding to $N \rightarrow \infty$ (cyan). The (22) and (12) elements are normalised with respect to the (11) element. The matrix elements, with exception for the ones of the cube were averaged over five different geometrical realisations. The columns represent the three different volume-equivalent radii $r_{ve} = 0.25 \mu\text{m}$ (left column), $r_{ve} = 0.5 \mu\text{m}$ (centre column), and $r_{ve} = 1.0 \mu\text{m}$ (right column).

405

4.2 Gaussian random cubes

406

407

408

409

410

411

412

413

414

415

416

417

As explained in Sec. 2.2 Gaussian random cubes are created by superimposing Gaussian distortions characterised by the correlation angle Γ and the radial standard deviation σ_r on a cube. Figs. 9 – 11 show the (11), (22), and (12) normalised scattering matrix elements for Gaussian random cubes. Each figure shows the matrix elements for a different volume-equivalent radius (Fig. 9 for $r_{ve} = 0.25 \mu\text{m}$, Fig. 10 for $r_{ve} = 0.5 \mu\text{m}$, and Fig. 11 for $r_{ve} = 1.0 \mu\text{m}$). As in Fig. 7 the rows indicate the respective mean matrix elements. The columns in all three figures indicate the radial standard deviation σ_r . The left-most column showed matrix elements for $\sigma_r = 0.05$, the centre-left column for $\sigma_r = 0.10$, the centre-right for $\sigma_r = 0.15$, and the right-most column for $\sigma_r = 0.20$. The colors indicate the correlation angle. The results for a correlation angle of $\Gamma = 10^\circ$ are shown in dark blue, the results for $\Gamma = 20^\circ$ in green, for $\Gamma = 30^\circ$ in light red and for $\Gamma = 90^\circ$ in yellow.

418

419

For comparison the corresponding matrix elements of a cube of the same volume-equivalent radius, shown in purple, were added in each panel.

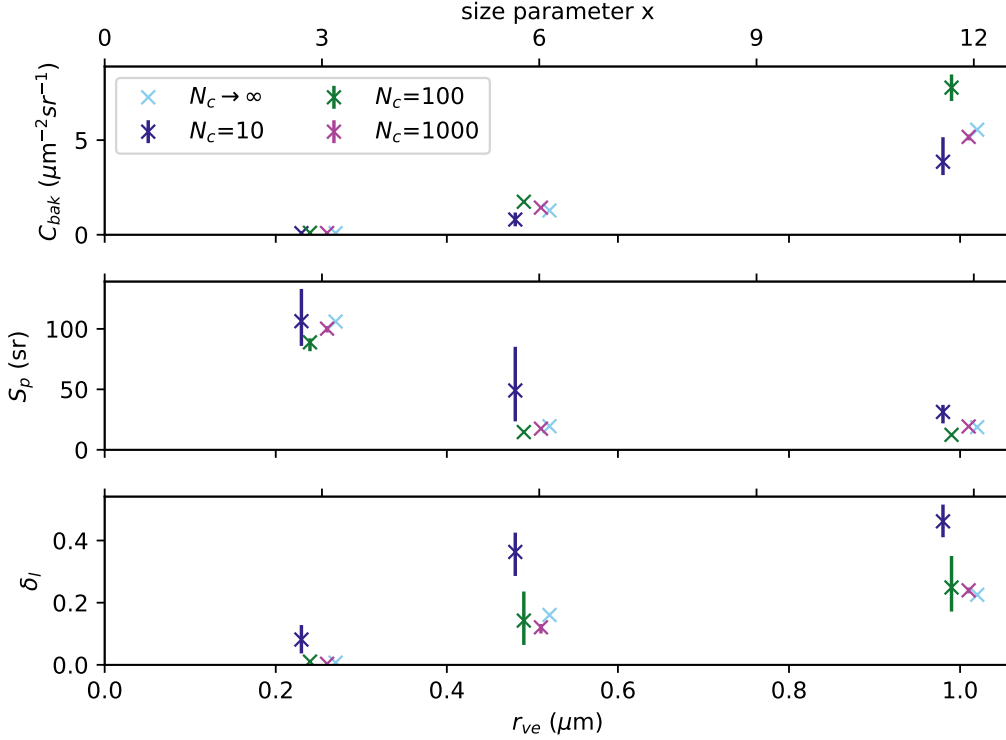


Figure 8. Size-dependent backscattering cross section C_{bak} (top row), extinction-to-backscatter ratio S_p (middle row), linear backscattering depolarization ratio δ_l (bottom row) for cubes, corresponding to $N_c \rightarrow \infty$ (cyan), $N_c = 10$ (dark blue), $N_c = 100$ (green), and $N_c = 1000$ (purple). Crosses denote the arithmetic mean over five geometric realisations (except for the cube) and the bars indicate the range between the minimum and the maximum value.

420 Inspection of Figs. 9–11 reveals several interesting features related to the random
 421 surface perturbations. Among the more predictable phenomena is a steadily increasing
 422 deviation from the scattering matrix elements of the cube with increasing radial stan-
 423 dard deviation σ_r (moving from left to right through the columns). Further, by compar-
 424 ing the three figures, we clearly see that the effect of surface perturbations becomes more
 425 pronounced for larger particles. For the largest particles (see Fig. 11) it becomes par-
 426 ticularly apparent that the impact of the surface perturbation is most pronounced for
 427 the shortest correlations angles. For small angles of Γ and high values of σ_r the Gaus-
 428 sian random perturbations of the reference geometry tend to smooth out some of the os-
 429 cillations in the (12) and (22) elements of the scattering matrix. Finally, we see in all
 430 three figures that, overall, the surface perturbation impacts the polarisation and depolarization-
 431 related scattering matrix elements S_{12} and S_{22} more dramatically than the phase func-
 432 tion S_{11} . While the (11) and (22) elements are fairly sensitive in the backscattering di-
 433 rection, the (12) element is mostly perturbed at angles away from the exact forward and
 434 backward-scattering directions.

435 Figure 12 shows the size-dependent backscattering cross section (left column), extinction-to-
 436 backscatter ratio (centre column), and the linear depolarization ratio (right column)
 437 for different correlation angles (colors as in Figs. 9–11) and radial standard deviations.
 438 The different radial standard deviations are represented in the different rows. The top

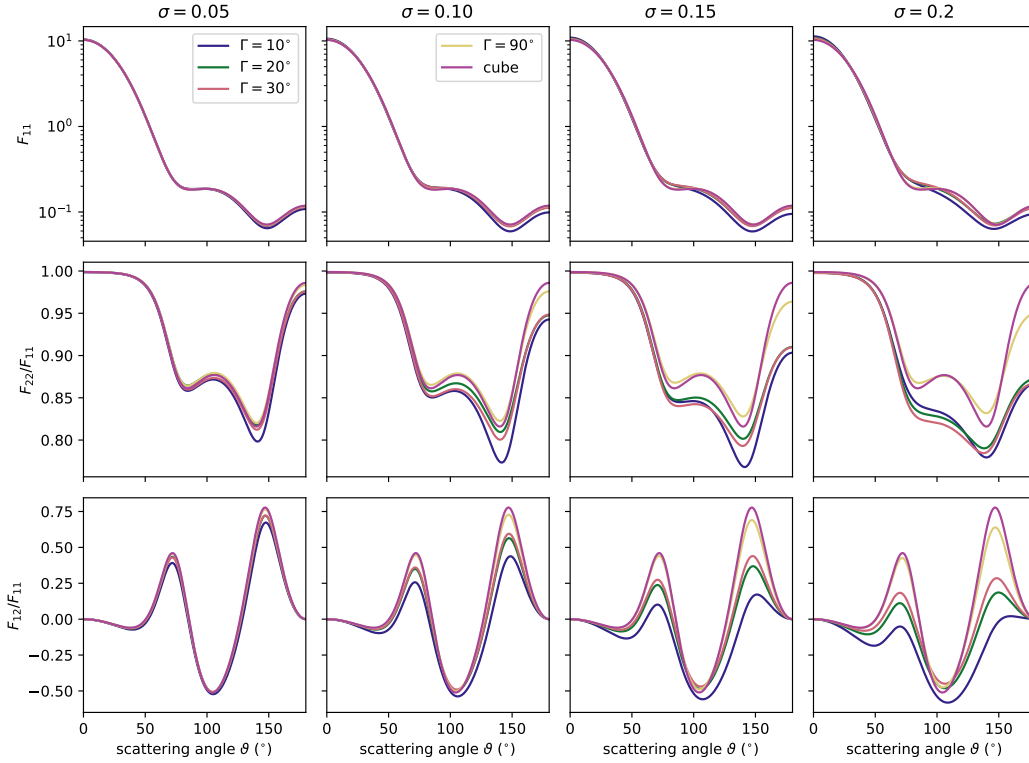


Figure 9. Ensemble-mean of F_{11} (top row), F_{22} (centre row), and F_{12} (bottom row) scattering matrix elements for Gaussian random cubes with a volume equivalent radius of $r_{ve} = 0.25 \mu\text{m}$ and different correlation angle Γ (indicated by the colors) and radial standard deviation σ_r (columns). In each plot the corresponding elements of a cube (purple line) were added for comparison. The left columns shows results for $\sigma_r = 0.05$, the centre left for $\sigma_r = 0.1$, the centre right for $\sigma_r = 0.15$, and the right column for $\sigma_r = 0.2$. A correlation angle of $\Gamma = 10^\circ$ is indicated by the dark blue lines, $\Gamma = 20^\circ$ by green, $\Gamma = 30^\circ$ by light red, and $\Gamma = 90^\circ$ by yellow.

439 row corresponds to $\sigma_r = 0.05$, the second to top row $\sigma_r = 0.1$, the third row $\sigma_r = 0.15$,
 440 and the the bottom row to $\sigma_r = 0.2$.

441 Compared to the cubical shape all Gaussian random cubes introduce a bias in the
 442 linear depolarization ratio; they all increase δ_l . The small scale distortions ($\Gamma = 10^\circ, 20^\circ, 30^\circ$)
 443 result in depolarization ratios, which deviate stronger from the values obtained for cubes,
 444 than the depolarization ratios stemming from the large scale distortion ($\Gamma = 90^\circ$).

445 4.3 Superellipsoids

446 Fig. 13 shows the (11) (top row), (22) (middle row), and (12) (bottom row) ele-
 447 ments of the scattering matrix F for superellipsoids with different roundness, namely $n =$
 448 $e = 0.0$, (cyan), $n = e = 0.1$ (dark green), $n = e = 0.2$ (light green), $n = e = 1.8$
 449 (light red), $n = e = 1.9$ (purple), and $n = e = 2.0$ (wine). The (22) and (12) ele-
 450 ments are normalised with respect to the (11) element. The columns indicate the dif-
 451 ferent sizes, with the results for $r_{ve} = 0.25 \mu\text{m}$ shown in the left column, for $r_{ve} = 0.5 \mu\text{m}$
 452 in the middle column, and for $r_{ve} = 1.0 \mu\text{m}$ in the right column.

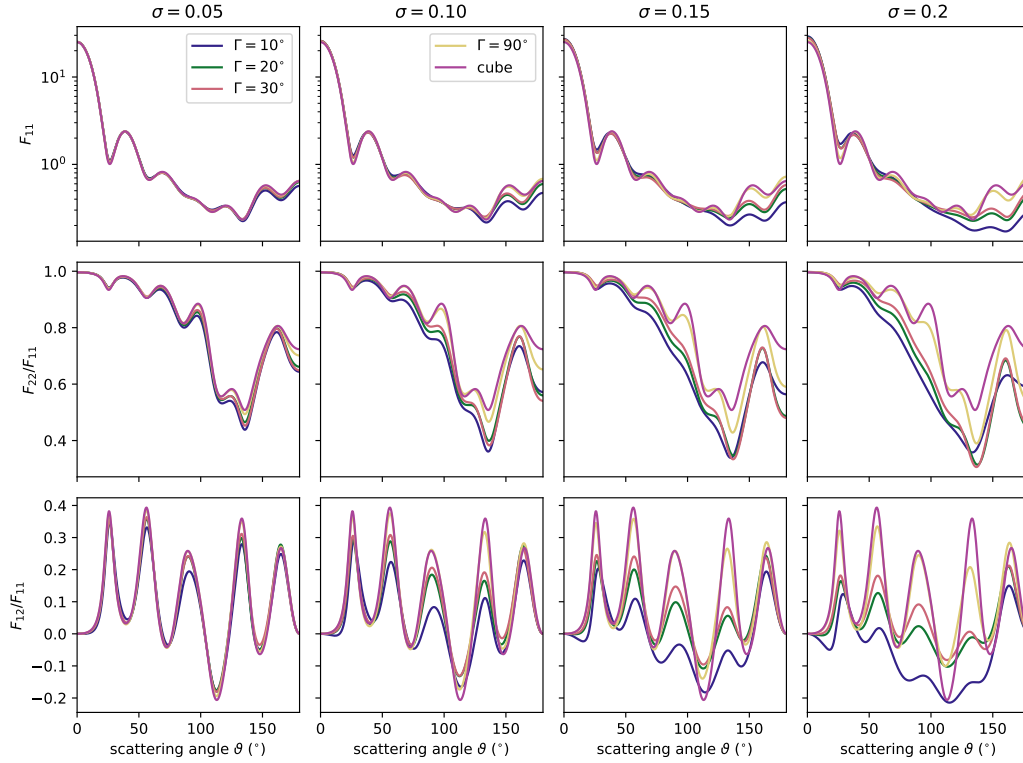


Figure 10. As Fig. 9, but for a volume-equivalent radius of $r_{ve} = 0.5 \mu\text{m}$

453 Scattering matrix elements for cubes with sharp edges do not strongly differ from
 454 those with rounded edges. Similarly, octahedra with sharp and with rounded edges display
 455 many similarities. The differences between cube-like and octahedra-like particles
 456 are generally larger than the corresponding differences among particles with different degrees
 457 of roundness in each of these two groups. However, there is one notable exception.
 458 The variability of the (22) element for the octahedron and the rounded octahedra ($n =$
 459 $e = 2.0$, $n = e = 1.8$, $n = e = 1.9$) is larger than that for the cube and rounded cubes
 460 ($n = e = 0.0$, $n = e = 0.1$, $n = e = 0.2$).

461 Analogous to Fig. 8, Fig. 14 shows the size-dependent backscattering cross section
 462 C_{bak} (top row), the size-dependent extinction-to-backscatter ratio S_p (middle row), and
 463 the linear backscattering depolarization ratio δ_l (bottom row). The different colors refer
 464 to the superellipsoids with different roundness parameters n with colors as in Fig. 13.

465 For $r_{ve} = 1.0 \mu\text{m}$ (rounded) octahedra have a higher backscattering cross section
 466 than (rounded) cubes, which results in a lower extinction-to-backscatter ratio. Further-
 467 more, the values of the linear depolarization ratio from (rounded) cubes ($\delta_l \approx 0.22$) and
 468 (rounded) octahedra ($\delta_l \sim 0.35 - 0.4$) for $r_{ve} = 1.0 \mu\text{m}$ deviate stronger from each
 469 other, than for the other two sizes. Increasing roundness, i.e. values of the roundness pa-
 470 rameter closer to 1, generally decreases the linear depolarization ratio. With exception
 471 of the octahedron-like superellipsoids with $r_{ve} = 1.0 \mu\text{m}$, for which the depolarization
 472 ratio was increased with increasing roundness.

473 The results, so far, provide us with valuable information on the importance of over-
 474 all shape and roundness for modeling optical properties of marine aerosol. However, they
 475 are based on comparing model particles with a definite size. We now want to turn our

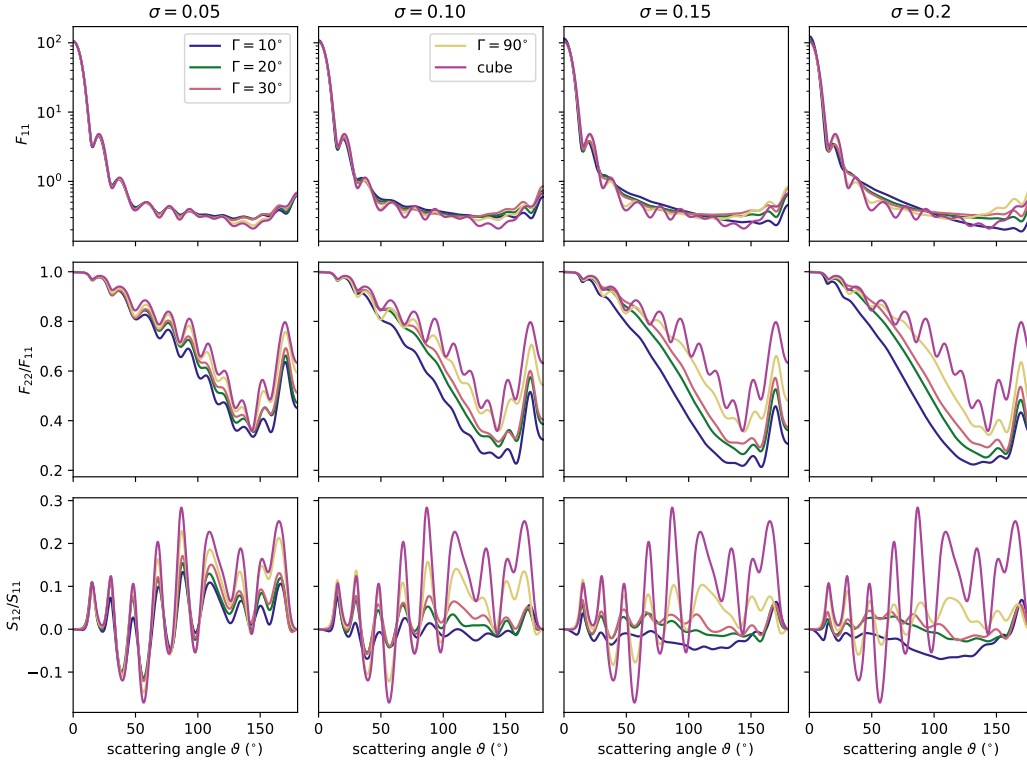


Figure 11. As Fig. 9, but for a volume-equivalent radius of $r_{ve} = 1.0 \mu\text{m}$

476 attention to size-averaged optical properties of ensembles of randomly oriented cubes with
 477 varying degrees of roundness. We also consider two different refractive indices. These
 478 results have been computed with the T-matrix program Tsym.

479 Figure 15 shows the backscattering cross section (top), the lidar ratio (centre), and
 480 the linear backscattering depolarization ratio (bottom) as a function of the effective radi-
 481 us. The lines represent different model particles as indicated in the legend and figure
 482 caption. Comparison of the left and right column shows that the results hardly depend
 483 on whether we assume a monomodal or a bimodal size distribution. (Note the different
 484 ranges on the x-axis in either column.)

485 Most prominently, we see that the impact of roundness on C_{bak} and S_p is dwarfed
 486 by that of the imaginary part κ of the refractive index. Increasing the κ from 0 to 0.06
 487 results in a dramatic decrease in C_{bak} , which causes a strong increase in S_p . The strength
 488 of this effect grows with increasing r_{eff} . By contrast, the corresponding impacts on δ_l are
 489 considerably more complex. The impact of roundness is, generally, of comparable mag-
 490 nitude as that of absorption. While roundness generally lowers δ_l for $r_{\text{eff}} \leq 1.3, \mu\text{m}$ rela-
 491 tive to cubes with sharp edges, it can have a lowering effect for $r_{\text{eff}} > 1.3, \mu\text{m}$ and $e =$
 492 $n = 0.1$, and an enhancing effect for $e = n = 0.2$. An increase of κ from 0 to 0.06 has
 493 little effect for $r_{\text{eff}} \leq 0.9, \mu\text{m}$, after which δ_l strongly drops with growing r_{eff} .

494 A possible explanation for the latter effect is this. Depolarization by nonspherical
 495 particles is strongly influenced by internal resonances induced inside the particle by the
 496 incident electromagnetic field. In absorbing particles, these resonances can become quenched.
 497 With growing size the absorption cross sections increases, which gradually diminishes
 498 the impact of the internal resonance modes. This mainly leaves induced surface currents

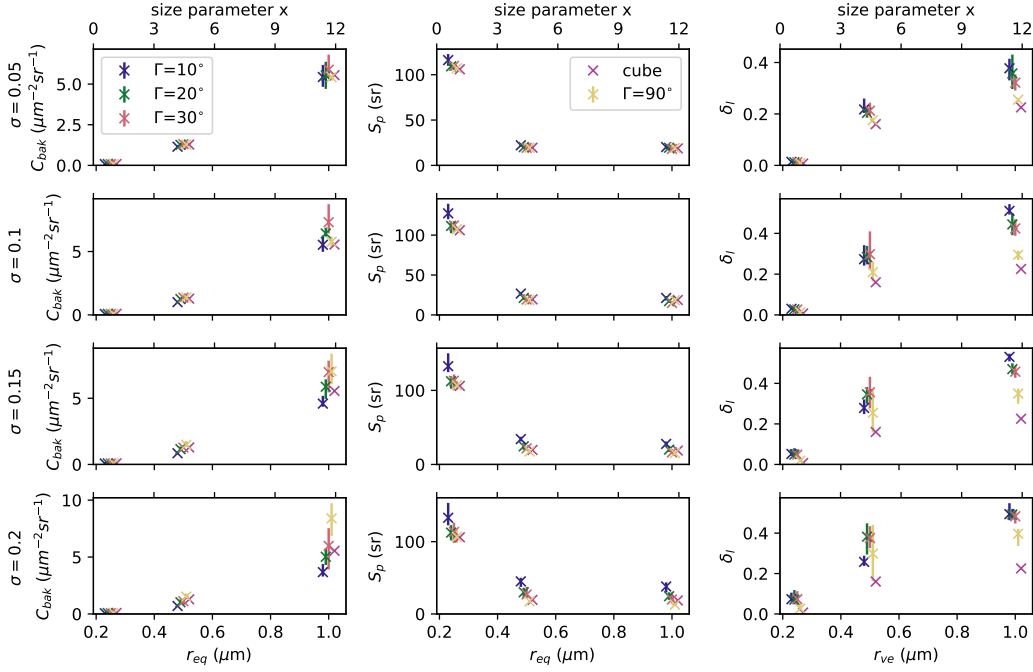


Figure 12. Size-dependent backscattering cross sections C_{bak} (left column), extinction-to-backscatter ratios S_p (middle column), and linear depolarization ratio δ_l (right column) of Gaussian random cubes with different correlation angle Γ and radial standard deviation σ_r . The different values of Γ are indicated by color (with colors as in Fig. 9), and the different values of σ_r are presented in different rows (first row: $\sigma_r = 0.05$, second row: $\sigma_r = 0.1$, third row: $\sigma_r = 0.15$, and bottom row: $\sigma_r = 0.2$). For comparison, each panel shows the corresponding values of cubes in purple.

499 on the particle surface to impact the depolarization properties of the particle. It is conceivable that the effect of these currents is weaker than that of the resonant modes inside the particle, which would explain the decrease in δ_l with growing particle size.

502 Figure 16 shows elements of the size-averaged Stokes scattering matrix as a function of scattering angle (x-axis) and effective radius (y-axis). A comparison with Fig. 13 shows that size-averaging smooths out many of the resonance features encountered for monodisperse particles, especially for larger particles. Comparison of rows 1–3 reveals that the rounding of the edges has a rather small effect on both the (11) element (left) and the (12) element (right), and a marginally more pronounced effect on the (22) element (centre column), especially around scattering angles around 100° – 150° . By contrast, comparison of rows 1 and 4 shows that an increase in the imaginary part κ of the refractive index has a dramatic effect on the (22) and (12) elements. In the (22) element the deep minimum at scattering angles between 100° – 150° becomes considerably more flat with increasing absorption. In the (12) element there is a fairly shallow minimum at scattering angles around 40° for non-absorbing, large particles (top right). As the particles become absorbing, this minimum deepens and shifts toward a scattering angle around 60° (bottom right).

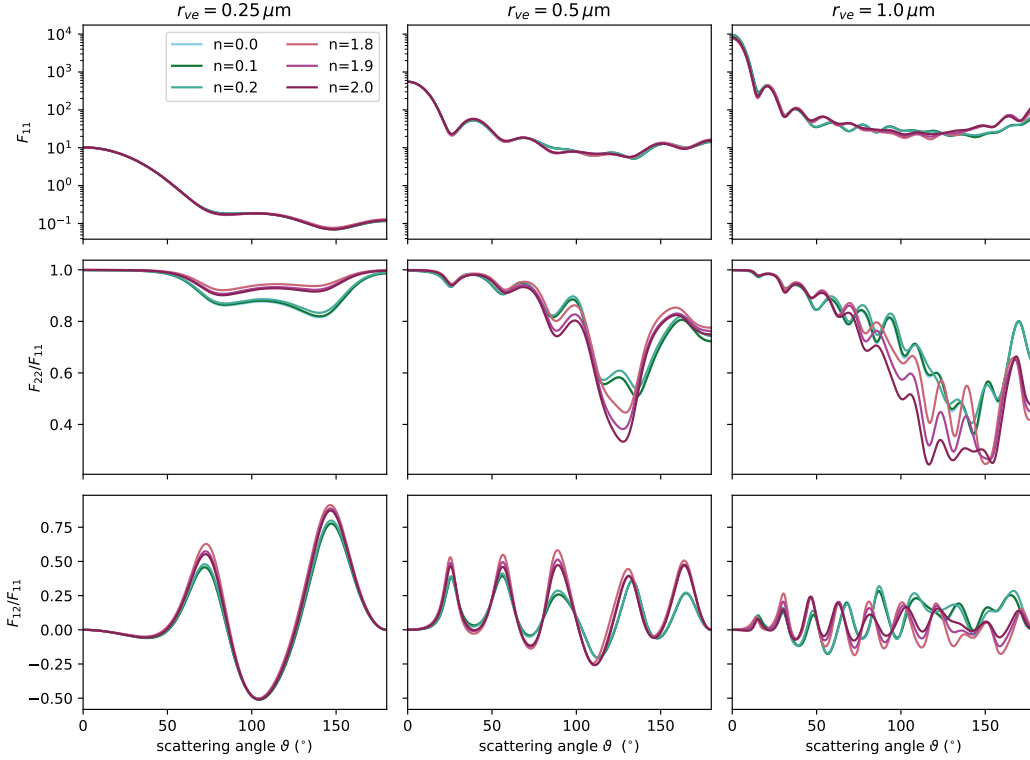


Figure 13. (11) (top row), (22) (centre row), and (12) (bottom row) elements of the normalised scattering matrix F for different superellipsoids with $n = e = 0.0$, corresponding to a cube (cyan), $n = e = 0.1$ (dark green), $n = e = 0.2$ (light green), $n = e = 1.8$ (light red), $n = e = 1.9$ (purple), and $n = e = 2.0$, corresponding to a octahedron (wine). The (22) and (12) elements are normalised with respect to the (11) element. The columns represent the three different volume-equivalent radii $r_{ve} = 0.25 \mu\text{m}$ (left column), $r_{ve} = 0.5 \mu\text{m}$ (centre column), and $r_{ve} = 1.0 \mu\text{m}$ (right column).

5 Discussion

516

517 Lidar field observations, as listed in Tab. 1, suggest that the linear backscattering
 518 depolarization ratio of marine aerosol lies in the range 0.08–0.20. Comparing the results
 519 of scattering calculations for single particle sizes with such field measurements can only
 520 serve as a consistency check, not as a conclusive validation. That being said, we do find
 521 in Fig. 14 that octahedral particles with or without rounded edges yield linear depolar-
 522 ization ratio that can far exceed the values reported in field measurements. Cubes with
 523 and without rounded edges lie closer to the reported range, although at the higher end.
 524 Similarly, we saw in Fig. 12 that, at least for large particle radii, δ_l modeled with Gaus-
 525 sian random cubes lies closer to typical field observations when assuming a correlation
 526 angle at the higher end, e.g. $\Gamma \sim 90^\circ$, and radial standard deviations not in excess of
 527 0.05. Small correlation angles can strongly enhance δ_l . We also saw in Fig. 8 that con-
 528 vex polyhedra that strongly deviate from cubical shape give unrealistically high δ_l val-
 529 ues. Irregular shapes that only mildly deviate from cubical shape are closer to $\delta_l=0.20$.
 530 All of these results point into the same direction, namely, that the depolarization of mar-
 531 ine aerosols is likely to be best described by particle shapes that display only mild de-
 532 viations from the shape of an ideal cube.

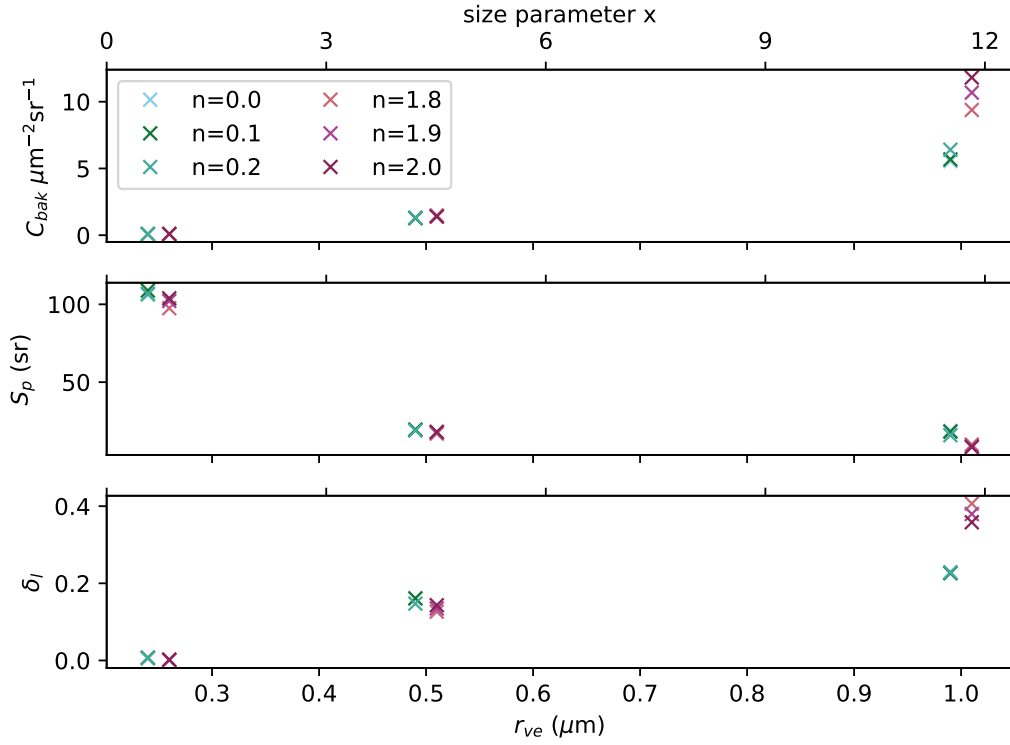


Figure 14. Size-dependent backscattering cross section C_{bak} (top row), extinction-to-backscatter ratio S_p (middle row), linear backscattering depolarization ratio δ_l (bottom row) for superellipsoids with different roundness parameters n . The colors are as in Fig. 13. To better distinguish the values the radius values were shifted around the actual radius.

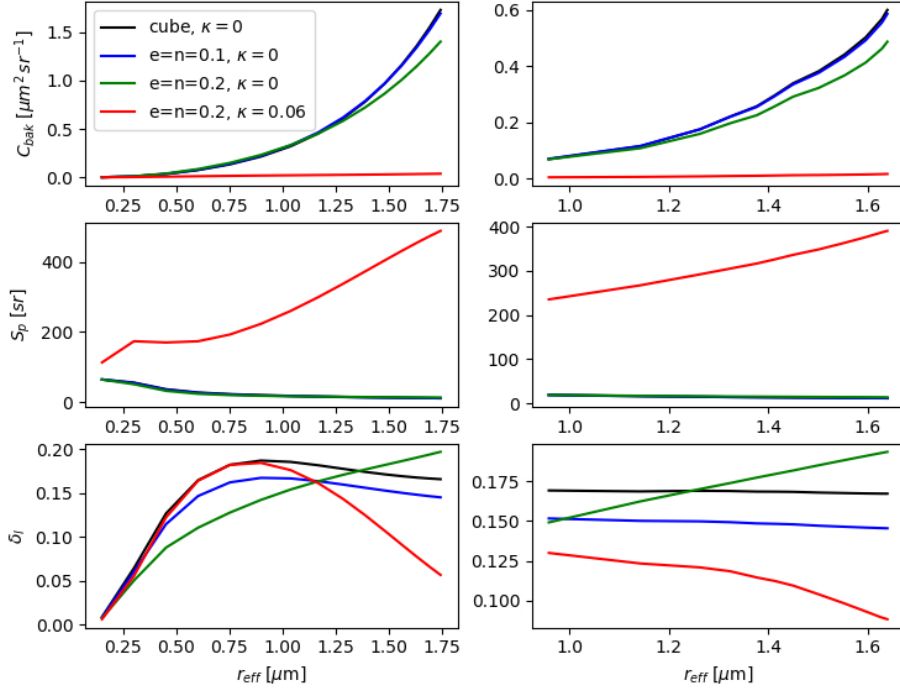


Figure 15. Size-averaged results for C_{bak} (top), S_p (centre), and δ_l (bottom) as a function of the effective radius r_{eff} . The lines show non-absorbing cubes with sharp edges (black), non-absorbing cubic superellipsoids with $e = n = 0.1$ (blue) and $n = e = 0.2$ (green), as well as absorbing superellipsoids ($e = n = 0.2$) with an imaginary part of the refractive index $\kappa = 0.06$ (red). The left row shows results averaged over log-normal monomodal size distributions, the right one over bimodal log-normal size distributions.

533 How can we explain field observations of δ_l as low as 0.08 as by Yin et al. (2019)?
 534 The bottom row in Fig. 15 suggests that there are several possible causes. Aerosol en-
 535 sembles dominated by small particles with effective radii up to $0.35\mu\text{m}$ can give rise to
 536 such low δ_l values. However, such a situation is unlikely to be encountered in the atmo-
 537 sphere, as we can see by inspecting the right column in Fig. 15. The range of effective
 538 radii on the x-axis are derived from the size distributions given by Porter and Clarke (1997),
 539 which include wind speeds as low as 0.4 m/s. Even under such conditions the marine aerosols
 540 rarely have effective radii less than $1\mu\text{m}$.

541 Another possible effect is observed for effective radii up to $1\mu\text{m}$. Rounding of edges
 542 can lower depolarization by an amount that depends on the degree of rounding, corrobor-
 543 ating results by Bi, Lin, Wang, et al. (2018). Further, for particles with r_{eff} larger than
 544 $0.9\mu\text{m}$, the presence of absorbing material can significantly quench depolarization. The
 545 exact chemical composition (and hence the refractive index) and its size dependence is
 546 unknown. However, as most marine aerosols can be assumed to be in the size range where
 547 absorption can become important, this is a potentially important topic.

548 Finally, for high relative humidity (RH) adsorption of water will inevitably sup-
 549 press depolarization, as the particles will become increasingly spherical. However, high

550 RH values were deliberately excluded in Table 1; marine aerosol with adsorbed water
551 are outside the scope of our discussion.

552 Measurements of the extinction-to-backscatter ratio of dried sea salt aerosol are
553 sparse. The two reported values, as can be inferred from Tab. 1, indicate a range between
554 13–25 sr. Owing to this limited amount of observations it is particularly challenging
555 to draw conclusions. Irrespective of the shape calculated values of the extinction-to-backscatter
556 ratio for $r_{ve} = 0.25 \mu\text{m}$ are in the order of ~ 100 sr and thereby exceed the range of
557 the reported values by far. For both $r_{ve} = 0.5 \mu\text{m}$ and $r_{ve} = 1.0 \mu\text{m}$ the values of S_p
558 are below 25 sr. A notable exception are the convex polyhedra with $N_c = 10$ and Gaus-
559 sian random cubes with small correlation angle and large radial standard deviation, both
560 types strongly deviate from the cubical base shape. Analogous to the values of the lin-
561 ear depolarization ratio Gaussian random cubes, which deviate less from the cubical shape
562 (i.e. have low radial standard deviations and high correlation angles) result in values of
563 the extinction-to-backscatter ratio, that are closest to the values obtained from cubes.
564 Thus, the results point in a similar direction as the results for the depolarization ratio;
565 the stronger the particle shape deviates from a cubical base shape, the stronger the de-
566 viation in extinction-to-backscatter ratio from the field observations. This implies that
567 strongly non-cubical shapes pose a risk of overestimating not only the depolarization ra-
568 tio, but also the extinction-to-backscatter ratio. However, the results for superellipsoids
569 in form of (rounded) octahedra with $r_{ve} = 1.0 \mu\text{m}$ give less clear indications. They re-
570 sult in lower values of the extinction-to-backscatter ratio (~ 8 sr), than (rounded) cubes
571 (~ 20 sr). At the same time they pose a risk of overestimating the values of the linear
572 depolarization ratio with $\delta_l = 0.36$ compared to $\delta_l = 0.23$ for cubes. While (rounded)
573 octahedra may help explaining values of the extinction-to-backscatter ratio of $S_p = 13 \pm$
574 3 sr as reported by Bohlmann et al. (2018), they are unlikely to explain the simultane-
575 ously low values of the linear depolarization ratio of $\delta_l = 0.09$ reported by Bohlmann
576 et al. (2018) for the same aerosol layer.

577 While the values of S_p for individual particles may exceed 25 sr, size averaging re-
578 duces the risk of overestimating S_p , as Fig. 15 indicates. Size distributions of non-absorbing
579 (rounded) cubes with effective radii smaller than $0.5 \mu\text{m}$, which are rare under atmospheric
580 conditions, still pose a risk of overestimating the extinction-to-backscatter ratio. How-
581 ever, for larger effective radii the size-averaged model results are in line with the lidar
582 field observations. However, the impact of size-averaging on the optical properties for
583 convex polyhedra, (rounded) octahedra and Gaussian random cubes has not been stud-
584 ied, Fig. 15 suggests, that high values of S_p for individual particles at a single size do
585 not allow for dismissing the entire geometry.

586 Further, cubical model particles, which follow the same size distribution as parti-
587 cles investigated during a laboratory experiment (reported by Sakai et al. (2010)), were
588 found to underestimate the measurements of the linear depolarization ratio in near-backscattering
589 direction (Bi, Lin, Wang, et al., 2018). (Bi, Lin, Wang, et al., 2018) reconciled measure-
590 ments and model results by modifying the particles' aspect ratio. After changing the as-
591 pect ratio of the superellipsoids the depolarization ratio may increase with increasing round-
592 ness parameter (Bi, Lin, Wang, et al., 2018). Superimposing Gaussian random pertur-
593 bations on a cube increases the linear depolarization ratio. Thus, they provide an ad-
594 ditional way of reducing the offset between laboratory measurements and model parti-
595 cles with respect to the depolarization ratio.

596 6 Conclusion

597 With exception of the study by Bi, Lin, Wang, et al. (2018), in which superellip-
598 soids were used, the linear depolarization ratio of sea salt particles was previously mod-
599 eled assuming cubes (Murayama et al., 1999; Sakai et al., 2010; David et al., 2013; Haarig
600 et al., 2017). Here the suitability of three different shape types, convex polyhedra, su-

601 perellipsoids, and Gaussian random cubes, to model both linear depolarization and extinction-
 602 to-backscatter ratio was investigated. In general the comparison of the modeling results
 603 with field and laboratory measurements reveals that geometries that depart too strongly
 604 from a cubical reference shape pose a high risk of overestimating linear depolarization
 605 and extinction-to-backscatter ratio. Compared to cubical reference geometries rounded
 606 cubes, obtained from superellipsoids, decrease the depolarization with increasing round-
 607 ness, while Gaussian random cubes increase the depolarization. An ensemble of random-
 608 ized, nearly cubical convex polyhedra yield linear depolarization ratio that appear to scat-
 609 ter uniformly about that of ideal cubes.

610 Thus, it appears that convex polyhedra can be employed for computing unbiased
 611 uncertainty estimates for cubical model particles, i.e., they can be employed for assess-
 612 ing the error introduced by neglecting random distortions and rounding of edges. Such
 613 uncertainty assessments would be useful for solving inverse problems, e.g., in retrieval
 614 algorithms or data assimilation of remote sensing observations of dried marine aerosol
 615 particles (e.g. Haarig et al., 2017). Both superellipsoids (see Bi, Lin, Wang, et al., 2018)
 616 and Gaussian random cubes can provide ways to reconcile measurements and model par-
 617 ticles by tuning the roundness and surface deformation parameters, respectively. Com-
 618 bining roundness and random surface distortions would provide us with another viable
 619 model to assess model errors. This is essential in inverse modeling. It is known from stud-
 620 ies on the depolarization properties of mineral dust (Kahnert et al., 2020) that unbiased
 621 error estimates are best obtained by combining different models of randomised geome-
 622 tries.

623 Owing to the high computational demands of the discrete dipole approximation,
 624 our study on size-averaged optical properties was limited to superellipsoids modeled with
 625 the T-matrix method. One of the main findings was that the presence of absorbing mat-
 626 erial in marine aerosols can dramatically increase the lidar ratio. Its effect on the de-
 627 polarisation ratio is dependent on the effective aerosol radius; but it is, generally, of com-
 628 parable magnitude as that related to rounding of edges.

629 Here only crystalline sea salt aerosol without any water coating was investigated.
 630 Adding a liquid water coating would extend the applicability of the model particles dis-
 631 cussed here towards higher values of relative humidity. Further laboratory studies com-
 632 bining measurements of the optical and the microphysical properties of dried sea salt aerosol
 633 particles can provide additional guidance regarding the choice and/or refinement of par-
 634 ticle models.

635 Acknowledgments

636 We acknowledge funding by the Swedish Research Council (*Vetenskapsrådet*, *dnr 2016-*
 637 *03499*) and by the Swedish National Space Agency (*Rymdstyrelsen*, *dnr 126/19*). The
 638 authors declare no conflicts of interest. The calculations were partially performed on re-
 639 sources at Chalmers Centre for Computational Science and Engineering (C3SE) provided
 640 by the Swedish National Infrastructure for Computing (SNIC). Maxim Yurkin and Al-
 641 fons Hoekstra are acknowledged for making their ADDA code publicly available. We are
 642 grateful to Karri Muionen for providing the G-sphere code. The data shown in the fig-
 643 ures is available under: <http://doi.org/10.5281/zenodo.3977898>

644 Appendix A Parameterisation of superellipsoids in spherical coordi- 645 nates

646 In Waterman’s T-matrix method, we need to evaluate vector products of vector spheri-
 647 cal wavefunctions $\Psi_{l,m,q}^{(j)}(r(\theta, \phi), \theta, \phi)$, where l, m, q are the degree, order, and mode, and
 648 where j denotes the kind of the vector wavefunctions. The surface integrals are evalu-

649 ated at the surface $r(\theta, \phi)$ of the particle. Thus, to use Waterman's method we need to
 650 have a parameterisation of the particle surface in spherical coordinates.

651 We start from the implicit equation (2) for the surface of a superellipsoid given in
 652 Cartesian coordinates by

$$653 \left(\left| \frac{x}{a} \right|^{2/e} + \left| \frac{y}{b} \right|^{2/e} \right)^{e/n} + \left| \frac{z}{c} \right|^{2/n} = 1. \quad (\text{A1})$$

654 The parameters a, b, c, n , and e are positive real numbers. a, b , and c characterise the
 655 extend of the particle along the three Cartesian axes, n is a roundness parameter in the
 656 polar (north-south) direction, and e is a roundness parameter in the azimuthal (east-west)
 657 direction. The superellipsoids are convex for $n, e \in (0, 2)$.

658 We introduce the following bracket notation:

$$659 [\xi]^\alpha = \text{sgn}(\xi)|\xi|^\alpha. \quad (\text{A2})$$

660 Then an explicit parameterisation is given by

$$661 x = a[\cos u]^n [\cos v]^e \quad (\text{A3})$$

$$662 y = b[\cos u]^n [\sin v]^e \quad (\text{A4})$$

$$663 z = c[\sin u]^n \quad (\text{A5})$$

$$664 u \in [-\pi/2, \pi/2], \quad v \in [-\pi, \pi]. \quad (\text{A6})$$

665 It is elementary to verify by direct substitution into (A1) that this parameterisation, in-
 666 deed, describes the surface of a superellipsoid. However, (u, v) are not spherical coordi-
 667 nates, as required by Waterman's T-matrix method.

668 To derive a parameterisation in spherical coordinates (θ, ϕ) , we need a parameter
 669 transformation $(u, v) \mapsto (\theta, \phi)$. To this end, we compute

$$670 \frac{y}{x} = \tan \phi = \frac{b}{a} [\tan(v + k\pi)]^e, \quad k \in \mathbb{Z}, \quad (\text{A7})$$

671 or

$$672 \tan(v + k\pi) = \left[\frac{a}{b} \tan \phi \right]^{1/e}, \quad (\text{A8})$$

673 where we explicitly indicated the periodicity of the tangent. The choice of k becomes im-
 674 portant when computing $\phi = \arctan(y/x)$. Making appropriate case distinctions for the
 675 four quadrants, we find that $k = 0$ for $\phi \in [0, \pi/2)$, $k = 1$ for $\phi \in [\pi/2, \pi)$, $k = -1$ for
 676 $\phi \in [\pi, 3\pi/2)$, and $k = -2$ for $\phi \in [3\pi/2, 2\pi)$. Thus we obtain the following param-
 677 eter transformation

$$678 v(\phi) = \arctan \left(\left[\frac{a}{b} \tan \phi \right]^{1/e} \right) + k\pi \quad (\text{A9})$$

$$679 k = \begin{cases} 0 & : \phi \in [0, \pi/2) \\ 1 & : \phi \in [\pi/2, \pi) \\ -1 & : \phi \in [\pi, 3\pi/2) \\ -2 & : \phi \in [3\pi/2, 2\pi) \end{cases} \quad (\text{A10})$$

680 To obtain an analogous parameter transformation for u , we consider

$$681 \frac{\sqrt{x^2 + y^2}}{z} = \tan \theta = \frac{1}{c} \frac{[\cos u]^n}{[\sin u]^n} \{a^2 |\cos v|^{2e} + b^2 |\sin v|^{2e}\}^{1/2}, \quad (\text{A11})$$

682 or

$$683 [\tan u]^n = \frac{1}{c} \cot \theta \sqrt{w}, \quad (\text{A12})$$

where

$$w(v(\phi)) = a^2 |\cos v|^{2e} + b^2 |\sin v|^{2e} \quad (\text{A13})$$

To solve for u , we make a case distinction. For $\theta \in [0, \pi/2)$, $\cot\theta > 0$. Then we must have $\tan u > 0$, which implies $u \in [0, \pi/2)$. Then $u = \arctan\{(1/c)\cot\theta\sqrt{w}\}^{1/n}$. Similarly, for $\theta \in [\pi/2, \pi)$ we find $u = -\arctan\{-(1/c)\cot\theta\sqrt{w}\}^{1/n}$. This can be summarised as follows

$$u(\theta, \phi) = S \arctan \left\{ \frac{S}{c} \cot\theta \sqrt{w(v(\phi))} \right\}^{1/n} \quad (\text{A14})$$

$$S = \begin{cases} 1 & : \theta \in [0, \pi/2) \\ -1 & : \theta \in [\pi/2, \pi) \end{cases} \quad (\text{A15})$$

Equations (A9), and (A14) in conjunction with (A10), (A13), and (A15) provide us with the desired parameter transformation $(u, v) \mapsto (\theta, \phi)$. Substitution into Eqs. (A3)–(A5) in conjunction with $r = \sqrt{x^2 + y^2 + z^2}$ gives us the required parameterisation $r(\theta, \phi)$ of the superellipsoid surface in spherical coordinates.

To evaluate the surface integrals in Waterman's method, we also need to express the surface element $d\sigma$ on the surface of the particle in spherical coordinates, i.e., we need to obtain $d\sigma = |\partial\mathbf{r}/\partial\theta \times \partial\mathbf{r}/\partial\phi| d\theta d\phi$. In principle, we could now proceed and compute expressions such as $\partial r/\partial\theta = (\partial r/\partial u)(\partial u/\partial\theta)$. It turns out that we encounter singularities in terms such as $\partial u/\partial\theta$. Therefore, we do well to first bring the parameter transformations into a more tractable form.

Inspection of Eqs. (A3)–(A5) shows that we never need the parameters u and v directly, but only $\cos u$, $\sin u$, $\cos v$ and $\sin v$. We can make use of the identities

$$\sin(\arctan x) = \frac{x}{\sqrt{1+x^2}} \quad (\text{A16})$$

$$\cos(\arctan x) = \frac{1}{\sqrt{1+x^2}}, \quad (\text{A17})$$

and we abbreviate

$$p = \left\{ S \frac{\sqrt{w}}{c} \cot\theta \right\}^{1/n} = \left[\frac{\sqrt{w}}{c} \cot\theta \right]^{1/n} \quad (\text{A18})$$

$$q = \left[\frac{a}{b} \tan\phi \right]^{1/e}. \quad (\text{A19})$$

This yields

$$\sin u = S \frac{p}{\sqrt{1+p^2}} \quad (\text{A20})$$

$$\cos u = \frac{1}{\sqrt{1+p^2}} \quad (\text{A21})$$

$$\sin v = (-1)^m \frac{q}{\sqrt{1+q^2}} \quad (\text{A22})$$

$$\cos v = (-1)^m \frac{1}{\sqrt{1+q^2}}, \quad (\text{A23})$$

whence

$$w = \frac{a^2 + b^2(q^2)^e}{(1+q^2)^e}. \quad (\text{A24})$$

and

$$\begin{aligned} r^2 &= x^2 + y^2 + z^2 \\ &= |\cos u|^{2n} (a^2 |\cos v|^{2e} + b^2 |\sin v|^{2e}) + c^2 |\sin u|^{2n} \\ &= \frac{w + c^2 (p^2)^n}{(1+p^2)^n}, \end{aligned} \quad (\text{A25})$$

720 where we have used the definition of w in Eq. (A13) as well as Eqs. (A20) and (A21).
 721 Backsubstitution of the definitions of p and q , Eqs. (A18) and (A19), into these expres-
 722 sions yields

$$723 \quad r(\theta, \phi) = \left\{ \frac{w}{\left\{ (\sin^2 \theta)^{1/n} + \left(\frac{w}{c^2} \cos^2 \theta \right)^{1/n} \right\}^n} \right\}^{1/2} \quad (\text{A26})$$

$$724 \quad w(\phi) = \frac{a^2(1 + \tan^2 \phi)}{\left\{ 1 + \left(\frac{a^2}{b^2} \tan^2 \phi \right)^{1/e} \right\}^e}. \quad (\text{A27})$$

725 The expression for r is manifestly regular for all θ . (Recall that $n > 0$.) Also, as we ap-
 726 proach a singularity of $\tan \phi$, w approaches b^2 . Thus, w and r are regular for all values
 727 of ϕ .

728 It is now straightforward, although a bit lengthy, to compute $\partial r / \partial \theta$ and $\partial r / \partial \phi = (\partial r / \partial w) (\partial w / \partial \phi)$.
 729 With the abbreviation

$$730 \quad t = \tan^2 \phi, \quad (\text{A28})$$

731 the final result is

$$732 \quad \frac{\partial r}{\partial \theta} = -\frac{w \cos \theta \left[\sin \theta \right]^{\frac{2}{n}-1} - \left(\frac{w}{c^2} \right)^{1/n} \sin \theta \left[\cos \theta \right]^{\frac{2}{n}-1}}{r \left\{ (\sin^2 \theta)^{1/n} + \left(\frac{w}{c^2} \cos^2 \theta \right)^{1/n} \right\}^{n+1}} \quad (\text{A29})$$

$$733 \quad \frac{\partial r}{\partial \phi} = \frac{a^2}{r} \frac{(\sin^2 \theta)^{1/n}}{\left\{ (\sin^2 \theta)^{1/n} + \left(\frac{w}{c^2} \cos^2 \theta \right)^{1/n} \right\}^{n+1}} \sqrt{t}(1+t) \frac{1 - \left(\frac{a^2}{b^2} \right)^{1/e} t^{\frac{1}{e}-1}}{\left\{ 1 + \left(\frac{a^2}{b^2} t \right)^{1/e} \right\}^{e+1}} \quad (\text{A30})$$

734

735 $\partial r / \partial \phi$ is regular for all values of θ . $\partial r / \partial \theta$ is also regular for all θ , provided that
 736 $n < 2$. Further, it is straightforward to show that the term dependent on $t = \tan^2 \phi$
 737 approaches 0 as $t \rightarrow \infty$ provided that $e < 2$. Thus, for convex particles ($0 < n, e < 2$)
 738 the partial derivatives of r are regular for all values of θ and ϕ .

739 The surface parameterisations derived here, as well as their partial derivatives, have
 740 been implemented into the most recent version of the Tsym program.

741 References

- 742 Adachi, K., & Buseck, P. R. (2015). Changes in shape and composition of sea-salt
 743 particles upon aging in an urban atmosphere. *Atmos. Environ.*, *100*, 1 - 9. doi:
 744 10.1016/j.atmosenv.2014.10.036
- 745 Barber, C. B., Dobkin, D. P., & Huhdanpaa, H. (1996). The quickhull algorithm for
 746 convex hulls. *ACM Trans. Math. Softw.*, *22*(4), 469–483. doi: 10.1145/235815
 747 .235821
- 748 Barr, A. H. (1981). Superquadrics and angle-preserving transformations. *IEEE*
 749 *Comput. Graphics Appl.*, *1*(1), 11-23. doi: 10.1109/MCG.1981.1673799
- 750 Bi, L., Lin, W., Liu, D., & Zhang, K. (2018). Assessing the depolarization capabil-
 751 ities of nonspherical particles in a super-ellipsoidal shape space. *Opt. Express*,
 752 *26*(2), 1726–1742. doi: 10.1364/OE.26.001726
- 753 Bi, L., Lin, W., Wang, Z., Tang, X., Zhang, X., & Yi, B. (2018). Optical
 754 modeling of sea salt aerosols: The effects of nonsphericity and inhomog-
 755 eneity. *J. Geophys. Res.*, *123*(1), 543-558. Retrieved from [https://](https://agupubs.onlinelibrary.wiley.com/doi/abs/10.1002/2017JD027869)
 756 agupubs.onlinelibrary.wiley.com/doi/abs/10.1002/2017JD027869 doi:
 757 10.1002/2017JD027869

- 758 Bohlmann, S., Baars, H., Radenz, M., Engelmann, R., & Macke, A. (2018). Ship-
 759 borne aerosol profiling with lidar over the atlantic ocean: from pure marine
 760 conditions to complex dust–smoke mixtures. *Atmos. Chem. Phys.*, *18*(13),
 761 9661–9679. Retrieved from [https://www.atmos-chem-phys.net/18/9661/](https://www.atmos-chem-phys.net/18/9661/2018/)
 762 2018/ doi: 10.5194/acp-18-9661-2018
- 763 Boucher, O. (2015). *Atmospheric aerosols - properties and climate impacts*. Springer,
 764 Dordrecht. doi: 10.1007/978-94-017-9649-1
- 765 Buseck, P. R., & Pósfai, M. (1999). Airborne minerals and related aerosol particles:
 766 Effects on climate and the environment. *Proceedings of the National Academy*
 767 *of Sciences of the United States of America*, *96*(7), 3372–3379.
- 768 Carrillo, J., Guerra, J. C., Cuevas, E., & Barrancos, J. (2016, Feb 01). Charac-
 769 terization of the marine boundary layer and the trade-wind inversion over
 770 the sub-tropical north atlantic. *Boundary Layer Meteorol.*, *158*(2), 311-
 771 330. Retrieved from <https://doi.org/10.1007/s10546-015-0081-1> doi:
 772 10.1007/s10546-015-0081-1
- 773 Chamaillard, K., Kleefeld, C., Jennings, S., Ceburnis, D., & O’Dowd, C. (2006).
 774 Light scattering properties of sea-salt aerosol particles inferred from modeling
 775 studies and ground-based measurements. *J. Quant. Spectrosc. Radiat. Trans-*
 776 *fer*, *101*(3), 498 - 511. Retrieved from [http://www.sciencedirect.com/](http://www.sciencedirect.com/science/article/pii/S0022407306000616)
 777 [science/article/pii/S0022407306000616](http://www.sciencedirect.com/science/article/pii/S0022407306000616) (Light in Planetary At-
 778 mospheres and Other Particulate Media) doi: [https://doi.org/10.1016/](https://doi.org/10.1016/j.jqsrt.2006.02.062)
 779 [j.jqsrt.2006.02.062](https://doi.org/10.1016/j.jqsrt.2006.02.062)
- 780 Chi, J. W., Li, W. J., Zhang, D. Z., Zhang, J. C., Lin, Y. T., Shen, X. J., ... Wang,
 781 W. X. (2015). Sea salt aerosols as a reactive surface for inorganic and organic
 782 acidic gases in the arctic troposphere. *Atmos. Chem. Phys.*, *15*(19), 11341–
 783 11353. Retrieved from <https://www.atmos-chem-phys.net/15/11341/2015/>
 784 doi: 10.5194/acp-15-11341-2015
- 785 Cooper, D., Davis, J., & Byers, R. (1974). Measurements of depolarization by dry
 786 and humidified salt aerosols using a lidar analogue. *J. Aerosol Sci.*, *5*(2), 117 -
 787 123. Retrieved from [http://www.sciencedirect.com/science/article/pii/](http://www.sciencedirect.com/science/article/pii/0021850274900433)
 788 [0021850274900433](http://www.sciencedirect.com/science/article/pii/0021850274900433) doi: [https://doi.org/10.1016/0021-8502\(74\)90043-3](https://doi.org/10.1016/0021-8502(74)90043-3)
- 789 Cotterell, M. I., Willoughby, R. E., Bzdek, B. R., Orr-Ewing, A. J., & Reid, J. P.
 790 (2017). A complete parameterisation of the relative humidity and wavelength
 791 dependence of the refractive index of hygroscopic inorganic aerosol parti-
 792 cles. *Atmos. Chem. Phys.*, *17*(16), 9837–9851. Retrieved from [https://](https://www.atmos-chem-phys.net/17/9837/2017/)
 793 www.atmos-chem-phys.net/17/9837/2017/ doi: 10.5194/acp-17-9837-2017
- 794 David, G., Thomas, B., Nousiainen, T., Miffre, A., & Rairoux, P. (2013). Retrieving
 795 simulated volcanic, desert dust and sea-salt particle properties from two/three-
 796 component particle mixtures using uv-vis polarization lidar and t matrix.
 797 *Atmos. Chem. Phys.*, *13*, 6757–6776. doi: 10.5194/acp-13-6757-2013
- 798 Eldridge, J., & Palik, E. D. (1997). - sodium chloride (nacl). In E. D. Palik (Ed.),
 799 *Handbook of optical constants of solids* (p. 775 - 793). Burlington: Academic
 800 Press. Retrieved from [http://www.sciencedirect.com/science/article/](http://www.sciencedirect.com/science/article/pii/B9780125444156500418)
 801 [pii/B9780125444156500418](http://www.sciencedirect.com/science/article/pii/B9780125444156500418) doi: [https://doi.org/10.1016/B978-012544415-6](https://doi.org/10.1016/B978-012544415-6.50041-8)
 802 [.50041-8](https://doi.org/10.1016/B978-012544415-6.50041-8)
- 803 Eloranta, E. E. (2005). High spectral resolution lidar. In C. Weitkamp (Ed.), *Lidar:*
 804 *Range-resolved optical remote sensing of the atmosphere* (pp. 143–163). New
 805 York, NY: Springer New York. Retrieved from [https://doi.org/10.1007/0-](https://doi.org/10.1007/0-387-25101-4_5)
 806 [387-25101-4_5](https://doi.org/10.1007/0-387-25101-4_5) doi: 10.1007/0-387-25101-4_5
- 807 Foltescu, V., Pryor, S. C., & Bennet, C. (2005). Sea salt generation, dispersion and
 808 removal on the regional scale. *Atmos. Environ.*, *39*, 2123-2133.
- 809 Gasteiger, J., Wiegner, M., Groß, S., Freudenthaler, V., Toledano, C., Tesche,
 810 M., & Kandler, K. (2011). Modelling lidar-relevant optical proper-
 811 ties of complex mineral dust aerosols. *Tellus B*, *63*(4), 725–741. doi:
 812 10.1111/j.1600-0889.2011.00559.x

- 813 Groß, S., Esselborn, M., Weinzierl, B., Wirth, M., Fix, A., & Petzold, A. (2013).
 814 Aerosol classification by airborne high spectral resolution lidar observations.
 815 *Atmos. Chem. Phys.*, *13*(5), 2487–2505. doi: 10.5194/acp-13-2487-2013
- 816 Gwaze, P., Helas, G. A., Annegarn, H. J., Huth, J., & Piketh, S. J. (2007). Physical,
 817 chemical and optical properties of aerosol particles collected over Cape Town
 818 during winter haze episodes. *S. Afr. J. Sci.*, *103*, 35 - 43. Retrieved from
 819 [http://www.scielo.org.za/scielo.php?script=sci_arttext&pid=S0038-](http://www.scielo.org.za/scielo.php?script=sci_arttext&pid=S0038-23532007000100010&nrm=iso)
 820 [-23532007000100010&nrm=iso](http://www.scielo.org.za/scielo.php?script=sci_arttext&pid=S0038-23532007000100010&nrm=iso)
- 821 Haarig, M., Ansmann, A., Gasteiger, J., Kandler, K., Althausen, D., Baars, H., ...
 822 Farrell, D. A. (2017). Dry versus wet marine particle optical properties: Rh
 823 dependence of depolarization ratio, backscatter, and extinction from multi-
 824 wavelength lidar measurements during saltrace. *Atmos. Chem. Phys.*, *17*(23),
 825 14199–14217. doi: 10.5194/acp-17-14199-2017
- 826 Hänel, G. (1976). The properties of atmospheric aerosol particles as functions of the
 827 relative humidity at thermodynamic equilibrium with the surrounding moist
 828 air. In H. Landsberg & J. V. Mieghem (Eds.), (Vol. 19, p. 73 - 188). Elsevier.
 829 Retrieved from [http://www.sciencedirect.com/science/article/pii/](http://www.sciencedirect.com/science/article/pii/S0065268708601429)
 830 [S0065268708601429](http://www.sciencedirect.com/science/article/pii/S0065268708601429) doi: [https://doi.org/10.1016/S0065-2687\(08\)60142-9](https://doi.org/10.1016/S0065-2687(08)60142-9)
- 831 Irshad, R., Grainger, R. G., Peters, D. M., McPheat, R. A., Smith, K. M., &
 832 Thomas, G. (2009). Laboratory measurements of the optical properties of
 833 sea salt aerosol. *Atmos. Chem. Phys.*, *9*(1), 221–230. Retrieved from [https://](https://www.atmos-chem-phys.net/9/221/2009/)
 834 www.atmos-chem-phys.net/9/221/2009/ doi: 10.5194/acp-9-221-2009
- 835 Järvinen, E., Kemppinen, O., Nousiainen, T., Kociok, T., Möhler, O., Leisner, T.,
 836 & Schnaiter, M. (2016). Laboratory investigations of mineral dust near-
 837 backscattering depolarization ratios. *J. Quant. Spectrosc. Radiat. Transfer*,
 838 *178*, 192 - 208. Retrieved from [http://www.sciencedirect.com/science/](http://www.sciencedirect.com/science/article/pii/S0022407315301722)
 839 [article/pii/S0022407315301722](http://www.sciencedirect.com/science/article/pii/S0022407315301722) (Electromagnetic and light scattering by
 840 nonspherical particles XV: Celebrating 150 years of Maxwell’s electromagnet-
 841 ics) doi: <https://doi.org/10.1016/j.jqsrt.2016.02.003>
- 842 Kahnert, M. (2005). Irreducible representations of finite groups in the T matrix for-
 843 mulation of the electromagnetic scattering problem. *J. Opt. Soc. Am. A*, *22*,
 844 1187-1199.
- 845 Kahnert, M. (2013). The T-matrix code Tsym for homogeneous dielectric particles
 846 with finite symmetries. *J. Quant. Spectrosc. Radiat. Transfer*, *123*, 62-78.
- 847 Kahnert, M., Kanngießer, F., Järvinen, E., & Schnaiter, M. (2020). Aerosol-
 848 optics model for the backscatter depolarisation ratio of mineral dust parti-
 849 cles. *J. Quant. Spectrosc. Radiat. Transfer*, *254*, 107177. Retrieved from
 850 <http://www.sciencedirect.com/science/article/pii/S0022407320303502>
 851 doi: <https://doi.org/10.1016/j.jqsrt.2020.107177>
- 852 Kahnert, M., & Kanngießer, F. (2020). Modelling optical properties of atmospheric
 853 black carbon aerosols. *J. Quant. Spectrosc. Radiat. Transfer*, *244*, 106849.
 854 Retrieved from [http://www.sciencedirect.com/science/article/pii/](http://www.sciencedirect.com/science/article/pii/S0022407319309550)
 855 [S0022407319309550](http://www.sciencedirect.com/science/article/pii/S0022407319309550) doi: <https://doi.org/10.1016/j.jqsrt.2020.106849>
- 856 King, S. M., Butcher, A. C., Rosenoern, T., Coz, E., Lieke, K. I., de Leeuw, G., ...
 857 Bilde, M. (2012, 02). Investigating primary marine aerosol properties: Ccn ac-
 858 tivity of sea salt and mixed inorganic-organic particles. *Environ. Sci. Technol.*,
 859 *46*(19), 10405-10412. Retrieved from <https://doi.org/10.1021/es300574u>
 860 doi: 10.1021/es300574u
- 861 Krishnamurti, T. N., Stefanova, L., & vasubandhu Misra. (2013). *Tropical meteorol-*
 862 *ogy: An introduction*. New York, NY: Springer New York. doi: 10.1007/978-1
 863 -4614-7409-8
- 864 McInnes, L. M., Covert, D. S., Quinn, P. K., & Germani, M. S. (1994). Measure-
 865 ments of chloride depletion and sulfur enrichment in individual sea-salt parti-
 866 cles collected from the remote marine boundary layer. *Journal of Geophysical*
 867 *Research: Atmospheres*, *99*(D4), 8257-8268. doi: 10.1029/93JD03453

- 868 Meira, G., Andrade, C., Alonso, C., Padaratz, I., & Borba, J. (2008). Mod-
 869 elling sea-salt transport and deposition in marine atmosphere zone – a tool
 870 for corrosion studies. *Corros. Sci.*, *50*(9), 2724 - 2731. Retrieved from
 871 <http://www.sciencedirect.com/science/article/pii/S0010938X08002333>
 872 doi: <https://doi.org/10.1016/j.corsci.2008.06.028>
- 873 Mishchenko, M. I., & Hovenier, J. W. (1995). Depolarization of light backscattered
 874 by randomly oriented nonspherical particles. *Opt. Lett.*, *20*(12), 1356–1358.
 875 doi: [10.1364/OL.20.001356](https://doi.org/10.1364/OL.20.001356)
- 876 Mishchenko, M. I., Travis, L. D., & Lacis, A. A. (2002). *Scattering, absorption, and*
 877 *emission of light by small particles*. CAMBRIDGE UNIVERSITY PRESS.
- 878 Muinonen, K., Nousiainen, T., Fast, P., Lumme, K., & Peltoniemi, J. (1996).
 879 Light scattering by gaussian random particles: Ray optics approximation. *J.*
 880 *Quant. Spectrosc. Radiat. Transfer*, *55*(5), 577 - 601. Retrieved from [http://](http://www.sciencedirect.com/science/article/pii/0022407396000039)
 881 www.sciencedirect.com/science/article/pii/0022407396000039 (Light
 882 Scattering by Non-Spherical Particles) doi: [10.1016/0022-4073\(96\)00003-9](https://doi.org/10.1016/0022-4073(96)00003-9)
- 883 Murayama, T. H., Okamoto, H., Kaneyasu, N., Kamataki, H., & Miura, K. (1999).
 884 Application of lidar depolarization measurement in the atmospheric bound-
 885 ary layer: Effects of dust and sea-salt particles. *J. Geophys. Res.*, *104*(D24),
 886 31781-31792. Retrieved from [https://agupubs.onlinelibrary.wiley.com/](https://agupubs.onlinelibrary.wiley.com/doi/abs/10.1029/1999JD900503)
 887 [doi/abs/10.1029/1999JD900503](https://agupubs.onlinelibrary.wiley.com/doi/abs/10.1029/1999JD900503) doi: [10.1029/1999JD900503](https://doi.org/10.1029/1999JD900503)
- 888 Murphy, D. M., Anderson, J. R., Quinn, P. K., McInnes, L. M., Brechtel, F. J.,
 889 Kreidenweis, S. M., ... Buseck, P. R. (1998, Mar 01). Influence of sea-salt
 890 on aerosol radiative properties in the southern ocean marine boundary layer.
 891 *Nature*, *392*(6671), 62-65. Retrieved from <https://doi.org/10.1038/32138>
 892 doi: [10.1038/32138](https://doi.org/10.1038/32138)
- 893 Nousiainen, T., & Kandler, K. (2015). Light scattering by atmospheric mineral dust
 894 particles. In A. A. Kokhanovsky (Ed.), *Light scattering reviews 9: Light scat-*
 895 *tering and radiative transfer* (pp. 3–52). Berlin, Heidelberg: Springer Berlin
 896 Heidelberg. Retrieved from https://doi.org/10.1007/978-3-642-37985-7_1
 897 doi: [10.1007/978-3-642-37985-7_1](https://doi.org/10.1007/978-3-642-37985-7_1)
- 898 Patterson, J. P., Collins, D. B., Michaud, J. M., Axson, J. L., Sultana, C. M., Moser,
 899 T., ... Gianneschi, N. C. (2016, 27). Sea spray aerosol structure and compo-
 900 sition using cryogenic transmission electron microscopy. *ACS Cent. Sci.*, *2*(1),
 901 40-47. Retrieved from <https://doi.org/10.1021/acscentsci.5b00344> doi:
 902 [10.1021/acscentsci.5b00344](https://doi.org/10.1021/acscentsci.5b00344)
- 903 Peart, A., & Evans, J. R. G. (2011). Study of sea salt particles launched by bub-
 904 ble burst. *Bub. Sci. Eng. Technol.*, *3*(2), 64-72. Retrieved from [https://](https://www.tandfonline.com/doi/abs/10.1179/1758897911Y.0000000004)
 905 www.tandfonline.com/doi/abs/10.1179/1758897911Y.0000000004 doi: [10](https://doi.org/10.1179/1758897911Y.0000000004)
 906 [.1179/1758897911Y.0000000004](https://doi.org/10.1179/1758897911Y.0000000004)
- 907 Porter, J. N., & Clarke, A. D. (1997). Aerosol size distribution models based on in
 908 situ measurements. *J. Geophys. Res.*, *109*, 6035–6045.
- 909 Pósfai, M., Anderson, J. R., Buseck, P. R., & Sievering, H. (1995). Com-
 910 positional variations of sea-salt-mode aerosol particles from the north
 911 atlantic. *J. Geophys. Res.*, *100*(D11), 23063-23074. Retrieved from
 912 <https://agupubs.onlinelibrary.wiley.com/doi/abs/10.1029/95JD01636>
 913 doi: [10.1029/95JD01636](https://doi.org/10.1029/95JD01636)
- 914 Sakai, T., Nagai, T., Mano, Y., Zaizen, Y., & Inomata, Y. (2012). Aerosol optical
 915 and microphysical properties as derived from collocated measurements us-
 916 ing polarization lidar and direct sampling. *Atmos. Environ.*, *60*, 419 - 427.
 917 Retrieved from [http://www.sciencedirect.com/science/article/pii/](http://www.sciencedirect.com/science/article/pii/S1352231012006528)
 918 [S1352231012006528](http://www.sciencedirect.com/science/article/pii/S1352231012006528) doi: <https://doi.org/10.1016/j.atmosenv.2012.06.068>
- 919 Sakai, T., Nagai, T., Zaizen, Y., & Mano, Y. (2010). Backscattering linear de-
 920 polarization ratio measurements of mineral, sea-salt, and ammonium sulfate
 921 particles simulated in a laboratory chamber. *Appl. Opt.*, *49*(23), 4441–4449.
 922 Retrieved from <http://ao.osa.org/abstract.cfm?URI=ao-49-23-4441> doi:

- 10.1364/AO.49.004441
- 923
924 Sakai, T., Shibata, T., Kwon, S.-A., Kim, Y.-S., Tamura, K., & Iwasaka, Y. (2000).
925 Free tropospheric aerosol backscatter, depolarization ratio, and relative hu-
926 midity measured with the raman lidar at nagoya in 1994–1997: contributions
927 of aerosols from the asian continent and the pacific ocean. *Atmos. Envi-
928 ron.*, *34*(3), 431 - 442. Retrieved from [http://www.sciencedirect.com/
929 science/article/pii/S1352231099003283](http://www.sciencedirect.com/science/article/pii/S1352231099003283) doi: [https://doi.org/10.1016/
930 S1352-2310\(99\)00328-3](https://doi.org/10.1016/S1352-2310(99)00328-3)
- 931 Schulz, F. M., Stamnes, K., & Stamnes, J. J. (1999). Point group symmetries in
932 electromagnetic scattering. *J. Opt. Soc. Am. A*, *16*, 853-865.
- 933 Shettle, E. P., & Fenn, R. W. (1979). *Models for the aerosols of the lower atmo-
934 sphere and the effects of humidity variations on their optical properties* (AFGL
935 Technical Report No. AFGL-TR-79-021A). Air Force Geophysics Laboratory.
936 Retrieved from <https://apps.dtic.mil/docs/citations/ADA08595>
- 937 Tang, I. N., Tridico, A. C., & Fung, K. H. (1997). Thermodynamic and optical
938 properties of sea salt aerosols. *Journal of Geophysical Research: Atmospheres*,
939 *102*(D19), 23269-23275. Retrieved from [https://agupubs.onlinelibrary
940 .wiley.com/doi/abs/10.1029/97JD01806](https://agupubs.onlinelibrary.wiley.com/doi/abs/10.1029/97JD01806) doi: 10.1029/97JD01806
- 941 Torge, A., Macke, A., Heinold, B., & Wauer, J. (2011). Solar radiative transfer simu-
942 lations in saharan dust plumes: particle shapes and 3-d effect. *Tellus B*, *63*(4),
943 770-780. Retrieved from [https://onlinelibrary.wiley.com/doi/abs/
944 10.1111/j.1600-0889.2011.00560.x](https://onlinelibrary.wiley.com/doi/abs/10.1111/j.1600-0889.2011.00560.x) doi: 10.1111/j.1600-0889.2011.00560.x
- 945 Ueda, S., Hirose, Y., Miura, K., & Okochi, H. (2014). Individual aerosol particles
946 in and below clouds along a mt. fuji slope: Modification of sea-salt-containing
947 particles by in-cloud processing. *Atmos. Res.*, *137*, 216 - 227. Retrieved from
948 <http://www.sciencedirect.com/science/article/pii/S0169809513002846>
949 doi: <https://doi.org/10.1016/j.atmosres.2013.10.011>
- 950 Virtanen, P., Gommers, R., Oliphant, T. E., Haberland, M., Reddy, T., Courn-
951 peau, D., ... SciPy 1.0 Contributors (2020, Mar 01). Scipy 1.0: fundamental
952 algorithms for scientific computing in python. *Nature Methods*, *17*(3), 261-
953 272. Retrieved from <https://doi.org/10.1038/s41592-019-0686-2> doi:
954 10.1038/s41592-019-0686-2
- 955 Wandinger, U. (2005). Raman lidar. In C. Weitkamp (Ed.), *Lidar: Range-
956 resolved optical remote sensing of the atmosphere* (pp. 241–271). New
957 York, NY: Springer New York. Retrieved from [https://doi.org/10.1007/
958 0-387-25101-4_9](https://doi.org/10.1007/0-387-25101-4_9) doi: 10.1007/0-387-25101-4_9
- 959 Wang, Z., Bi, L., Yi, B., & Zhang, X. (2019). How the inhomogeneity of wet sea
960 salt aerosols affects direct radiative forcing. *Geophys. Res. Lett.*, *46*(3), 1805-
961 1813. Retrieved from [https://agupubs.onlinelibrary.wiley.com/doi/abs/
962 10.1029/2018GL081193](https://agupubs.onlinelibrary.wiley.com/doi/abs/10.1029/2018GL081193) doi: 10.1029/2018GL081193
- 963 Wells, N. C. (2011). *The atmosphere and ocean: A physical introduction* (3rd Edi-
964 tion ed.). John Wiley & Sons, Inc.
- 965 Wise, M. E., Biskos, G., Martin, S. T., Russell, L. M., & Buseck, P. R. (2005).
966 Phase transitions of single salt particles studied using a transmission electron
967 microscope with an environmental cell. *Aerosol Sci. Technol.*, *39*(9), 849-
968 856. Retrieved from <https://doi.org/10.1080/02786820500295263> doi:
969 10.1080/02786820500295263
- 970 Wriedt, T. (2002). Using the t-matrix method for light scattering computations by
971 non-axisymmetric particles: Superellipsoids and realistically shaped particles.
972 *Part. Part. Sys. Charact.*, *19*(4), 256-268. doi: 10.1002/1521-4117(200208)19:
973 4<256::AID-PPSC256>3.0.CO;2-8
- 974 Yin, Z., Ansmann, A., Baars, H., Seifert, P., Engelmann, R., Radenz, M., ...
975 Maupin, F. (2019). Aerosol measurements with a shipborne sun–sky–
976 lunar photometer and collocated multiwavelength raman polarization li-
977 dar over the atlantic ocean. *Atmos. Meas. Tech.*, *12*(10), 5685–5698. Re-

- 978 trieved from <https://www.atmos-meas-tech.net/12/5685/2019/> doi:
979 10.5194/amt-12-5685-2019
- 980 Yurkin, M. A., & Hoekstra, A. G. (2007). The discrete dipole approximation: An
981 overview and recent developments. *J. Quant. Spectrosc. Radiat. Transfer*,
982 106(1), 558–589. (IX Conference on Electromagnetic and Light Scattering by
983 Non-Spherical Particles) doi: 10.1016/j.jqsrt.2007.01.034
- 984 Yurkin, M. A., & Hoekstra, A. G. (2011). The discrete-dipole-approximation code
985 adda: Capabilities and known limitations. *J. Quant. Spectrosc. Radiat. Trans-*
986 *fer*, 112(13). doi: 10.1016/j.jqsrt.2011.01.031
- 987 Yurkin, M. A., Maltsev, V. P., & Hoekstra, A. G. (2006, Oct). Convergence
988 of the discrete dipole approximation. ii. an extrapolation technique to in-
989 crease the accuracy. *J. Opt. Soc. Am. A*, 23(10), 2592–2601. Retrieved
990 from <http://josaa.osa.org/abstract.cfm?URI=josaa-23-10-2592> doi:
991 10.1364/JOSAA.23.002592
- 992 Zeng, J., Zhang, G., Long, S., Liu, K., Cao, L., Bao, L., & Li, Y. (2013). Sea salt
993 deliquescence and crystallization in atmosphere: an in situ investigation using
994 x-ray phase contrast imaging. *Surface and Interface Analysis*, 45(5), 930-
995 936. Retrieved from <https://onlinelibrary.wiley.com/doi/abs/10.1002/sia.5184> doi: 10.1002/sia.5184
- 996 Zieger, P., Väisänen, O., Corbin, J. C., Partridge, D. G., Bastelberger, S., Mousavi-
997 Fard, M., ... Salter, M. E. (2017). Revising the hygroscopicity of inorganic sea
998 salt particles. *Nat. Commun.*, 8(1), 15883. doi: 10.1038/ncomms15883
- 999

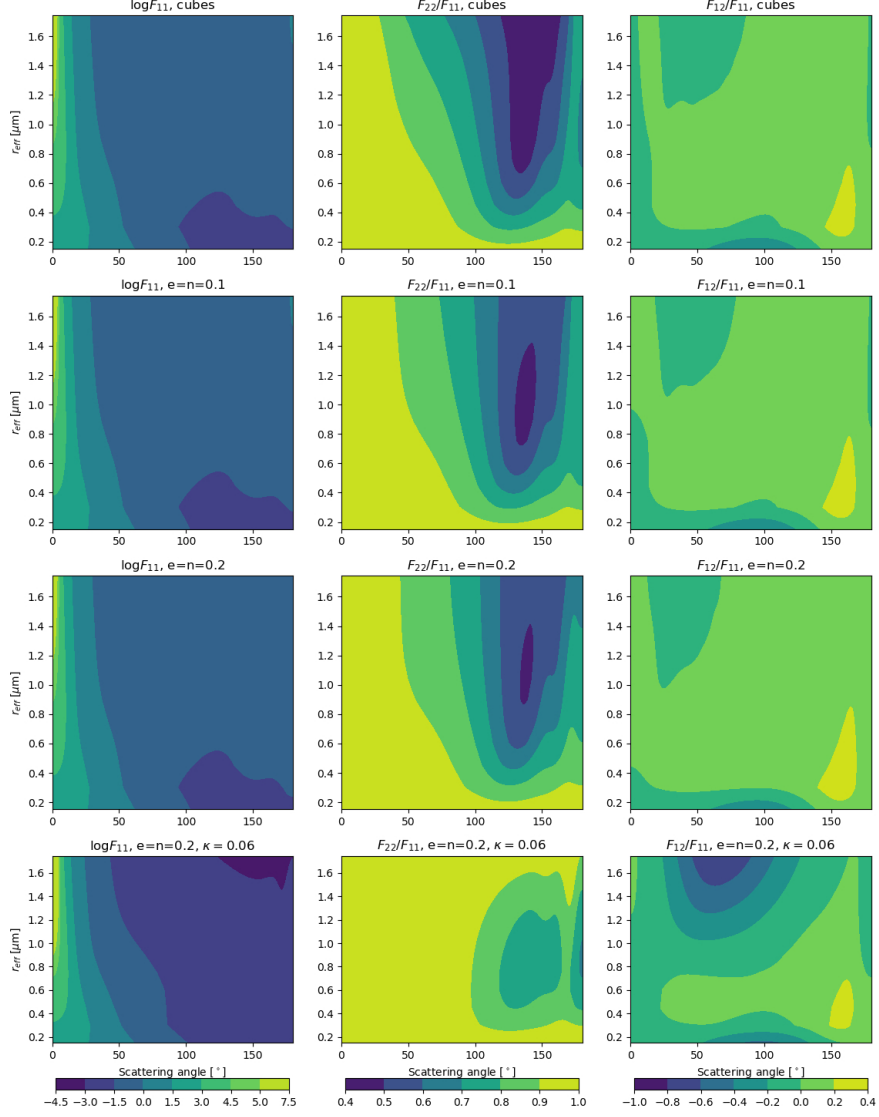
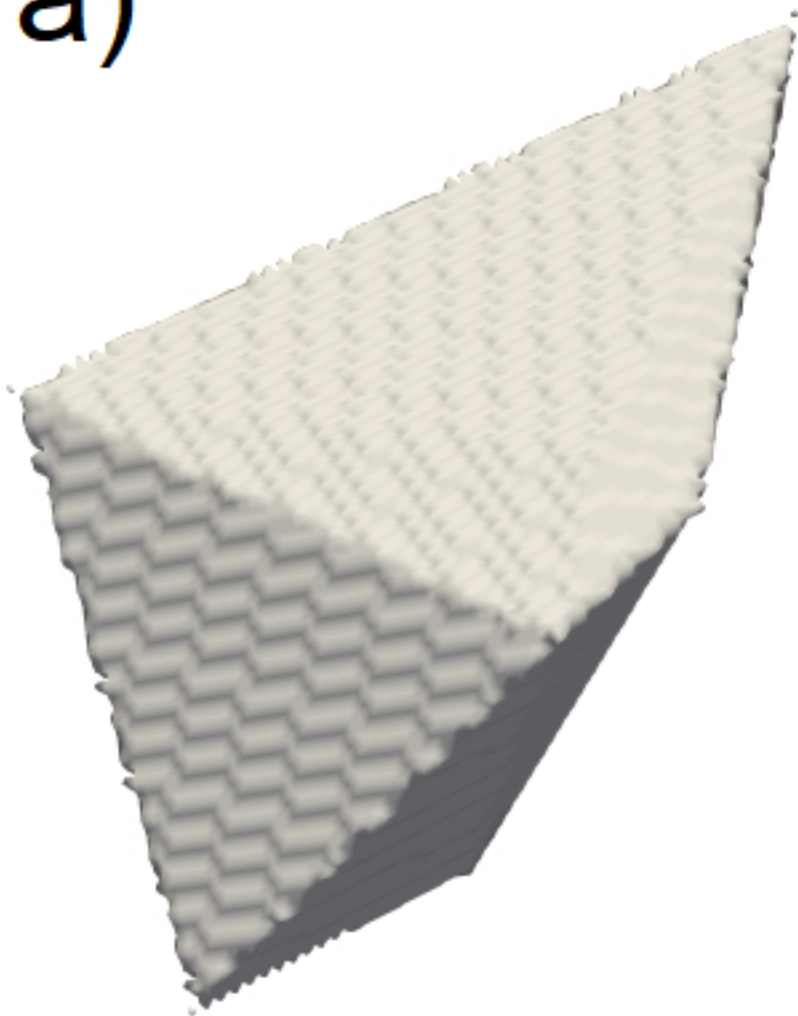


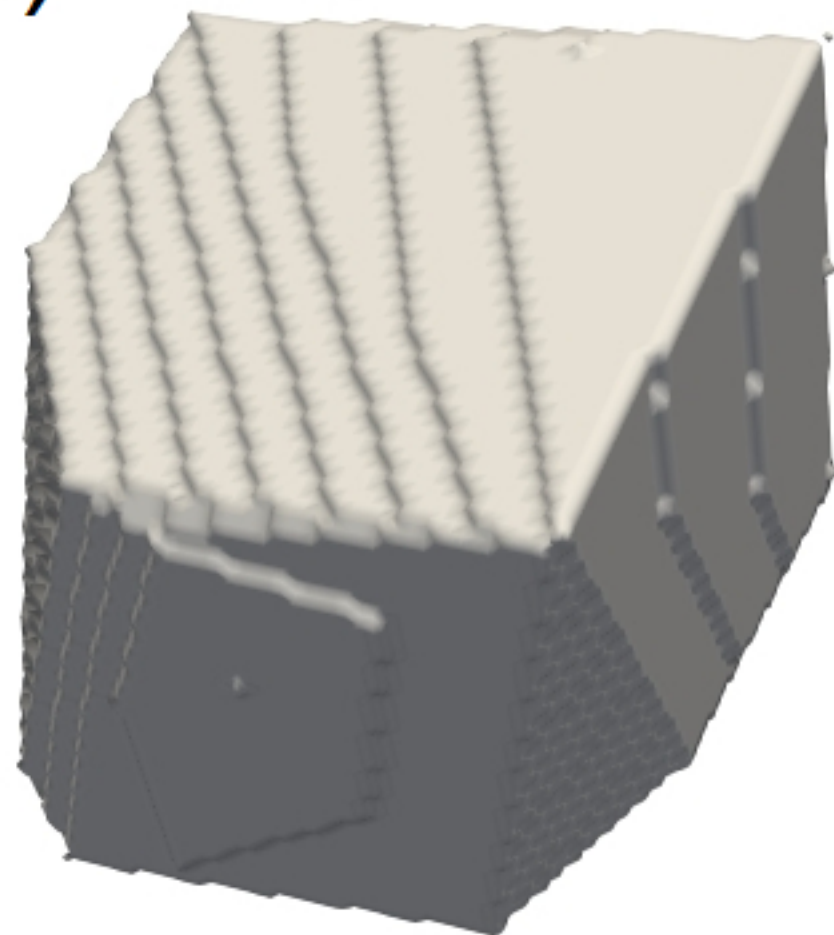
Figure 16. Elements of the Stokes scattering matrix as a function of scattering angle and effective radius r_{eff} . The three columns show the elements $\log F_{11}$ (left), F_{22}/F_{11} (centre), and F_{12}/F_{11} (right). The rows show results for an imaginary part of the refractive index $\kappa = 0$ (rows 1–3), and $\kappa = 0.06$ (row 4), as well as for roundness parameters $e = n = 0$ (rows 1 and 4), $e = n = 0.1$ (row 2), and $e = n = 0.2$ (row 3).

Figure 1.

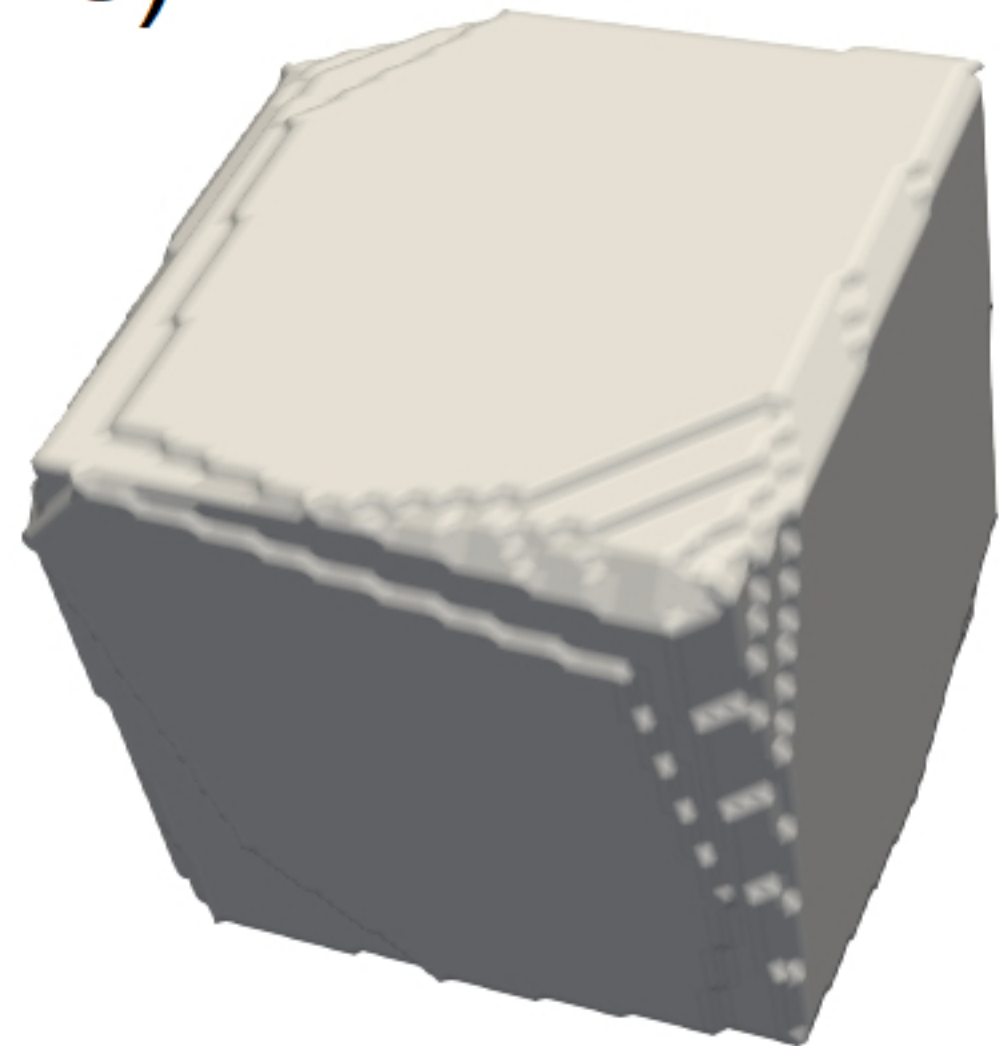
a)



b)



c)



d)

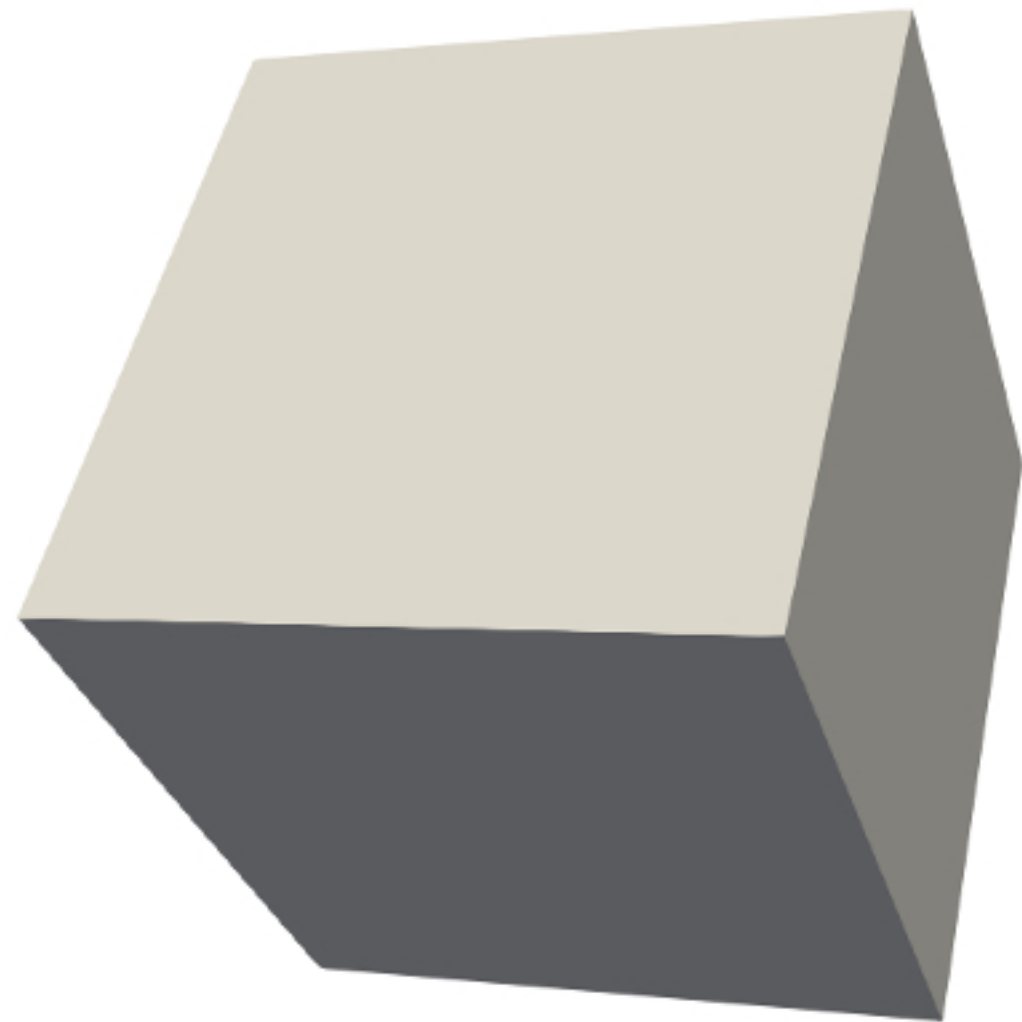
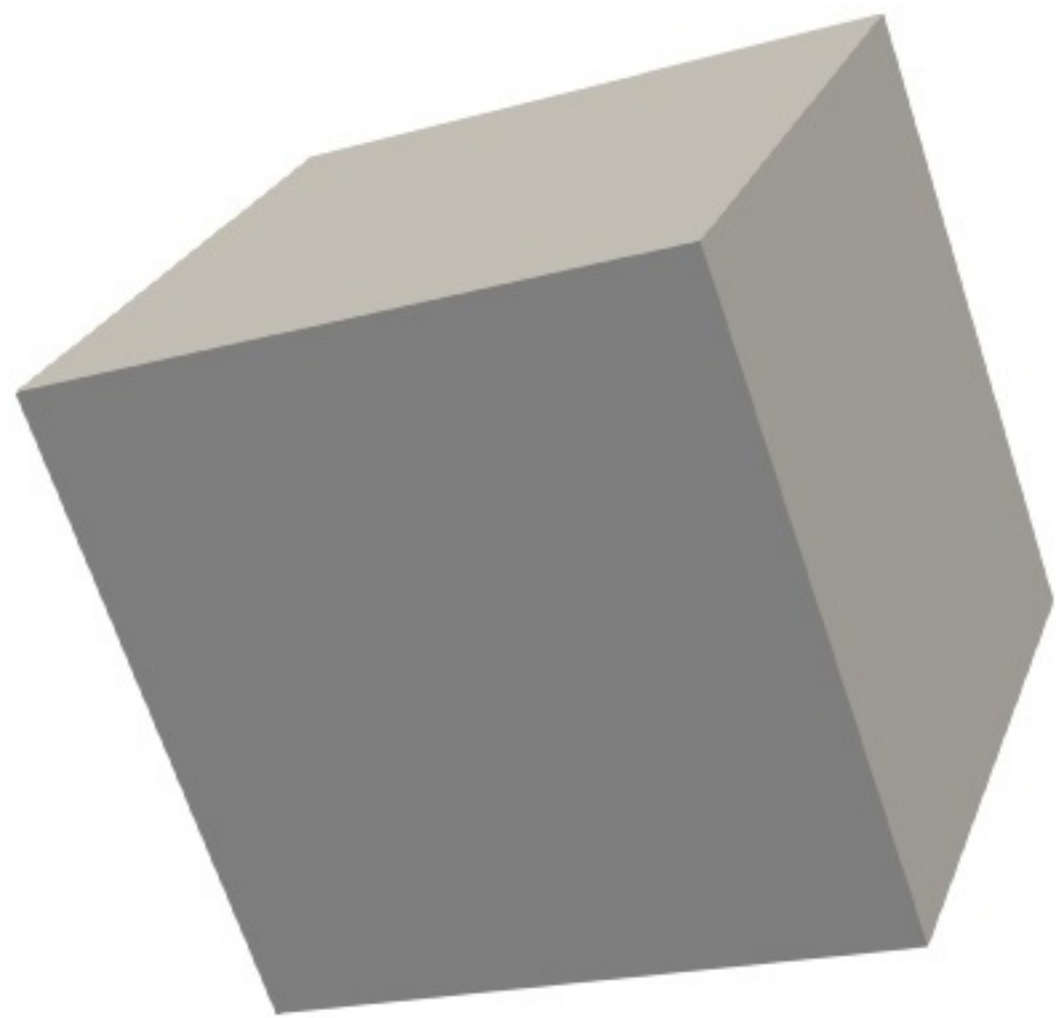
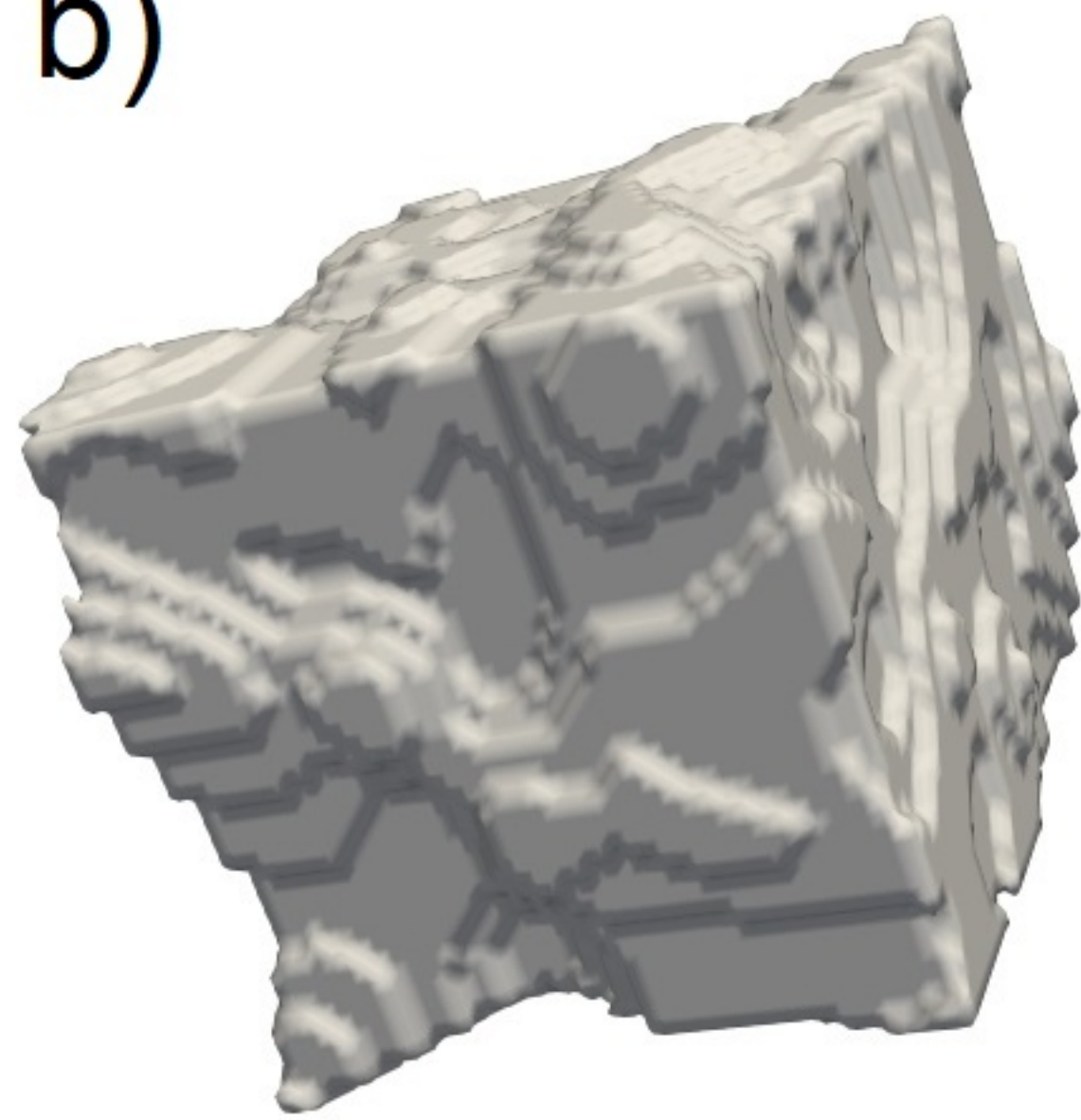


Figure 2.

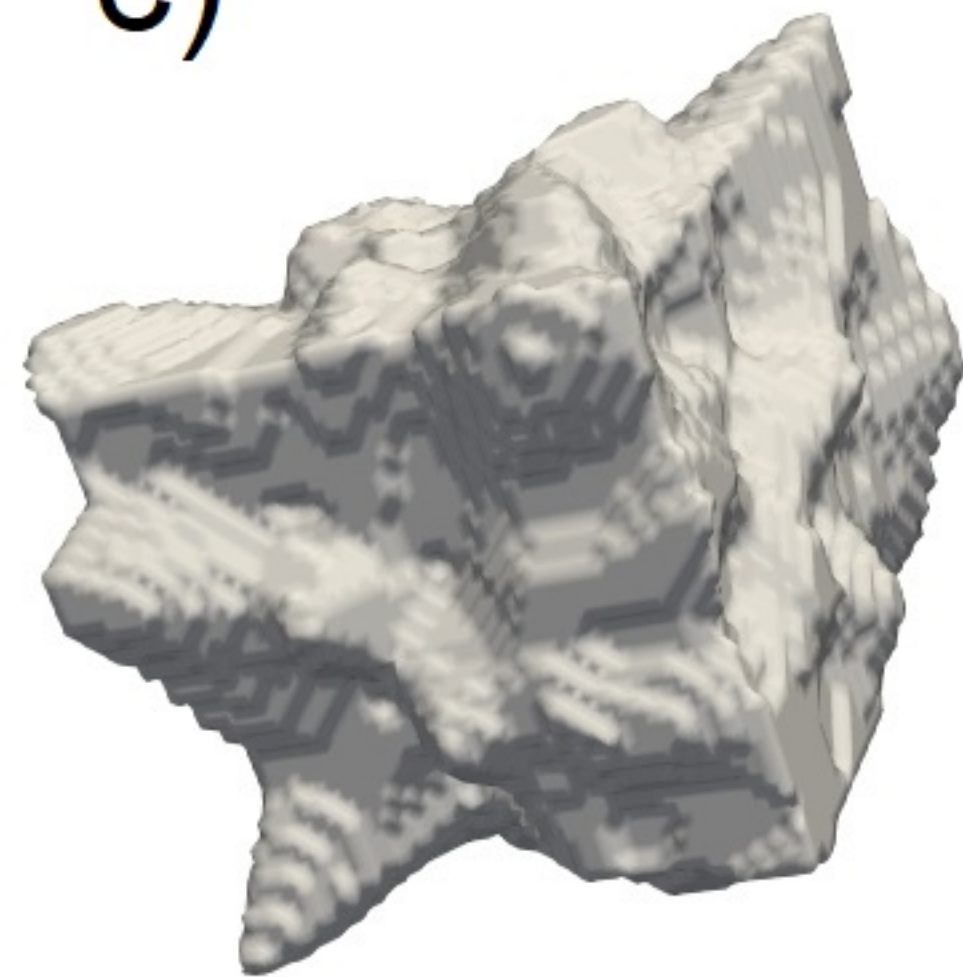
a)



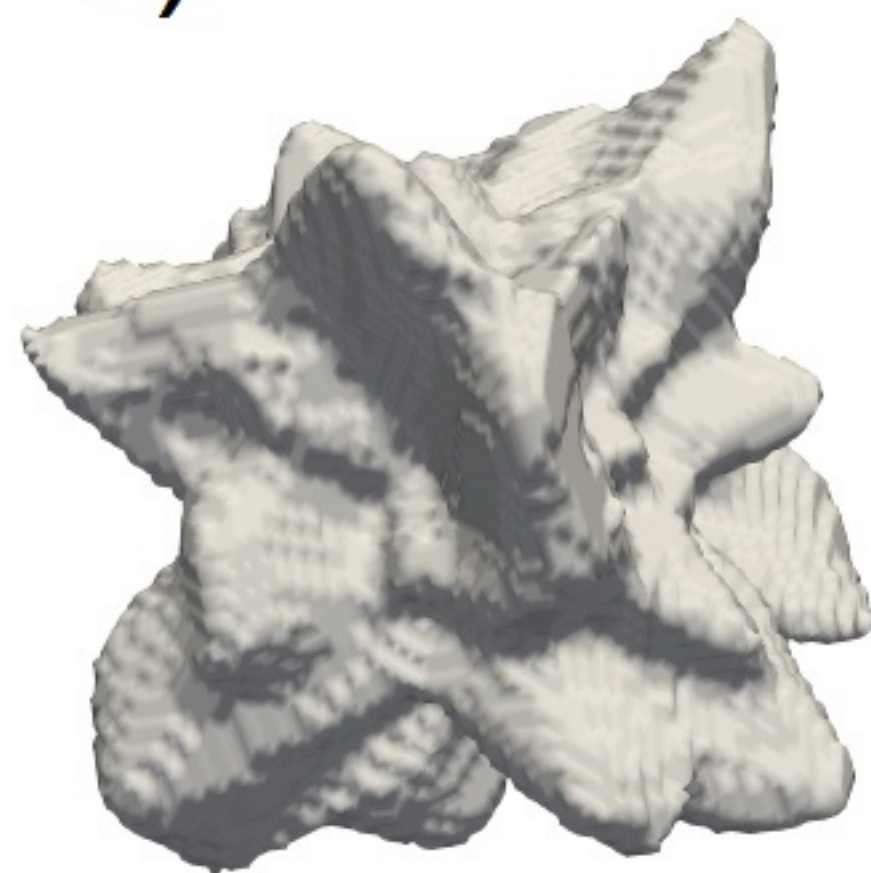
b)



c)



d)



e)



Figure 3.

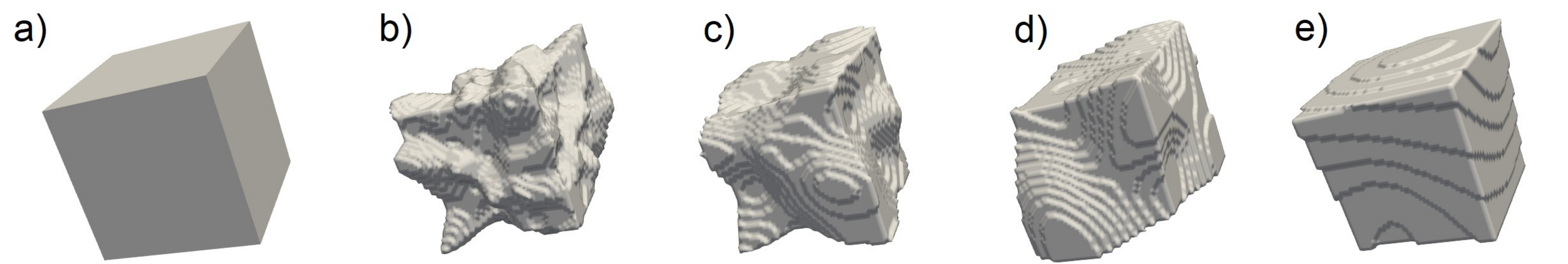
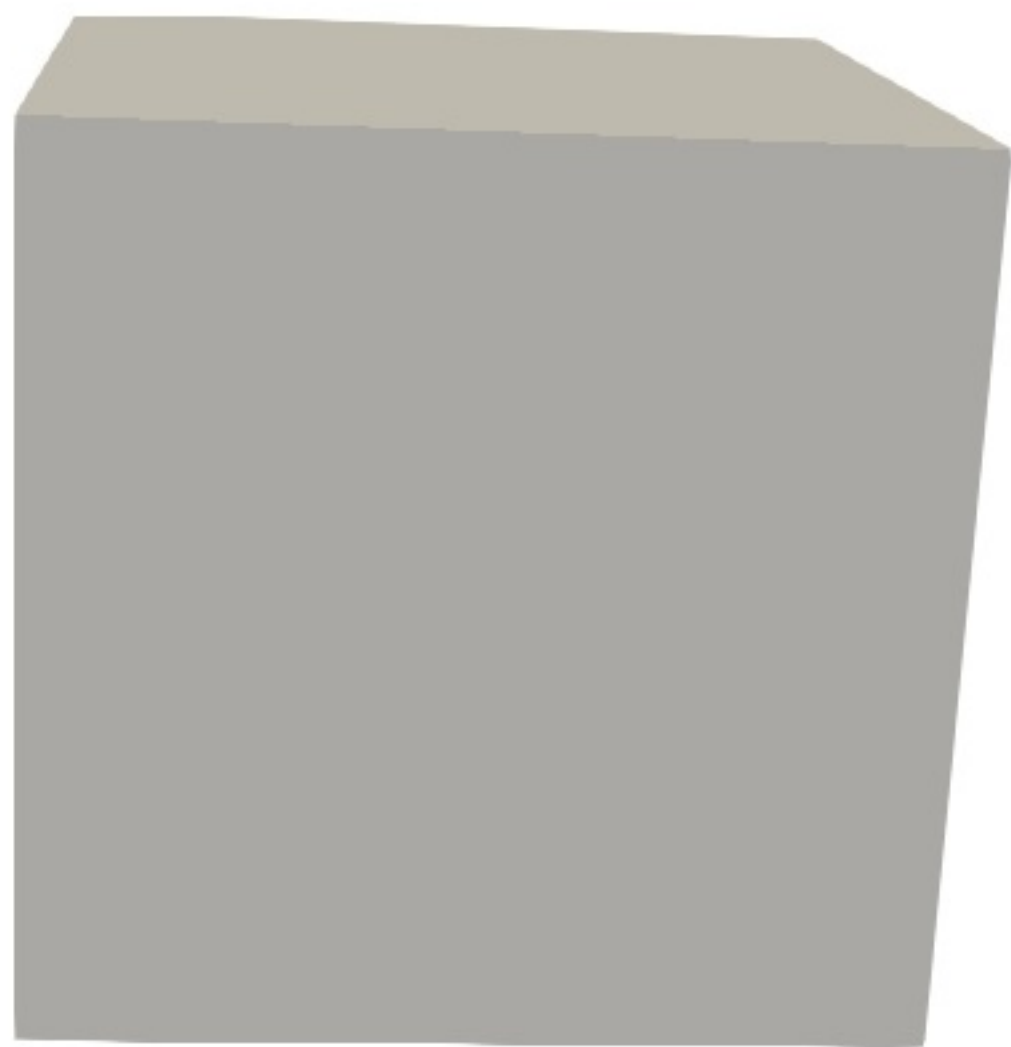


Figure 4.

a)



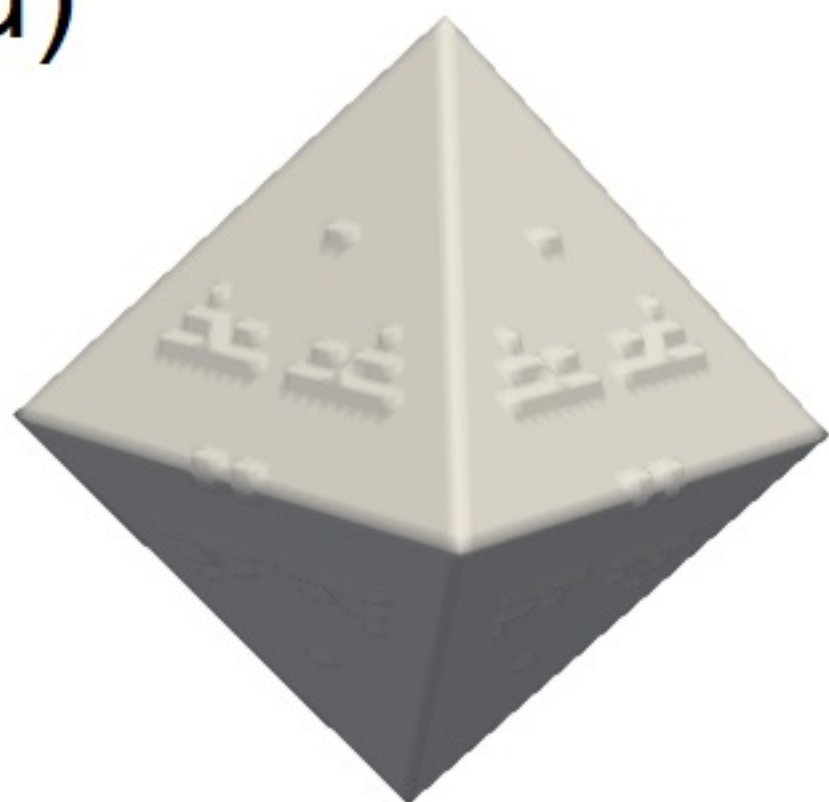
b)



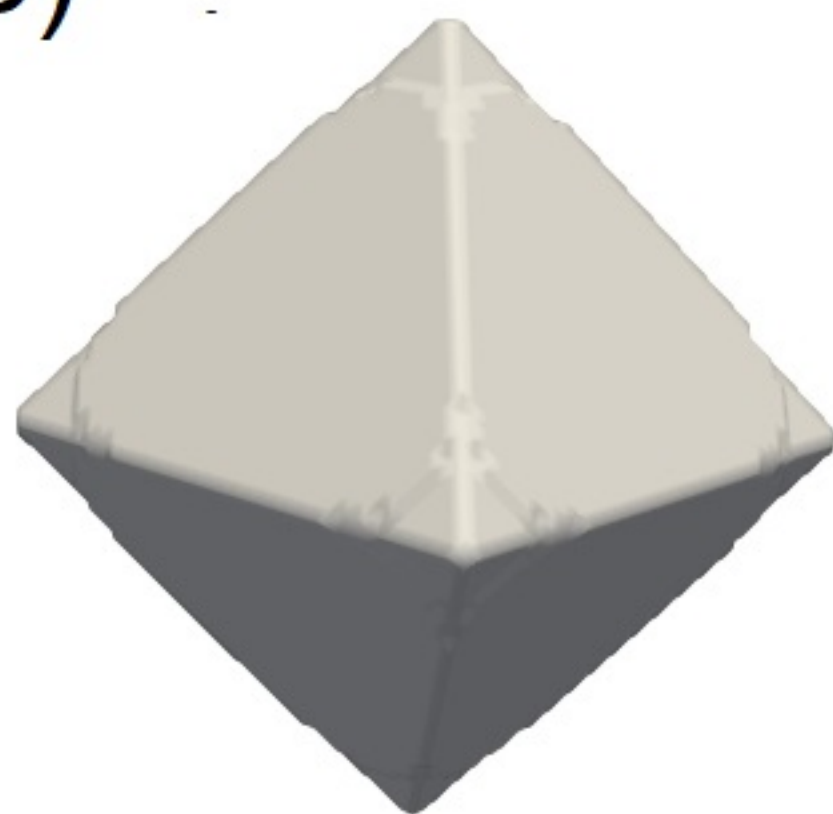
c)



d)



e)



f)

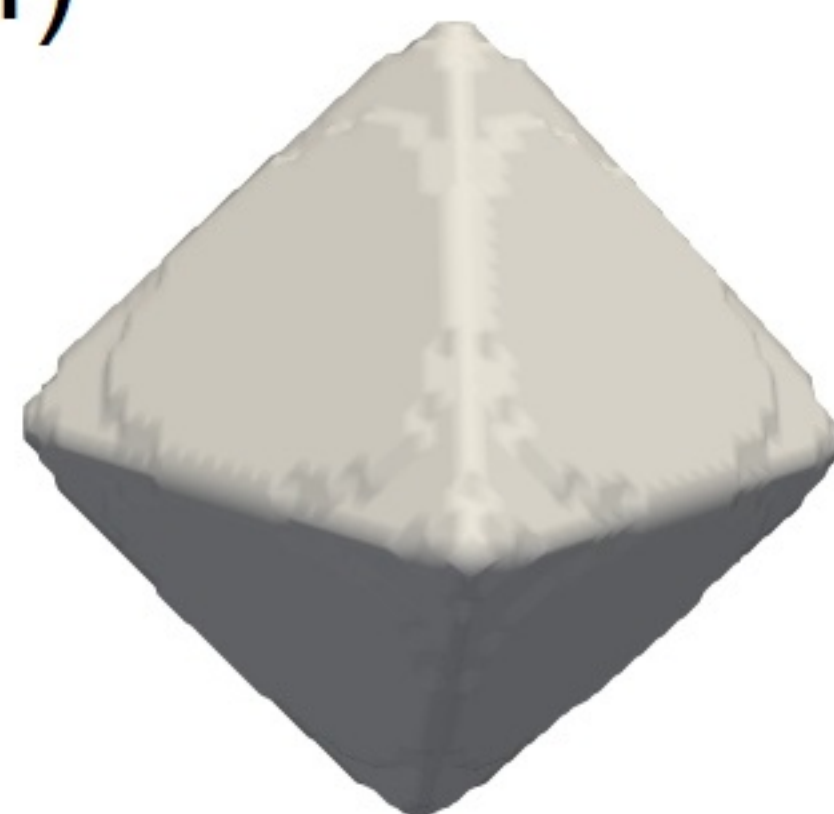


Figure 5.

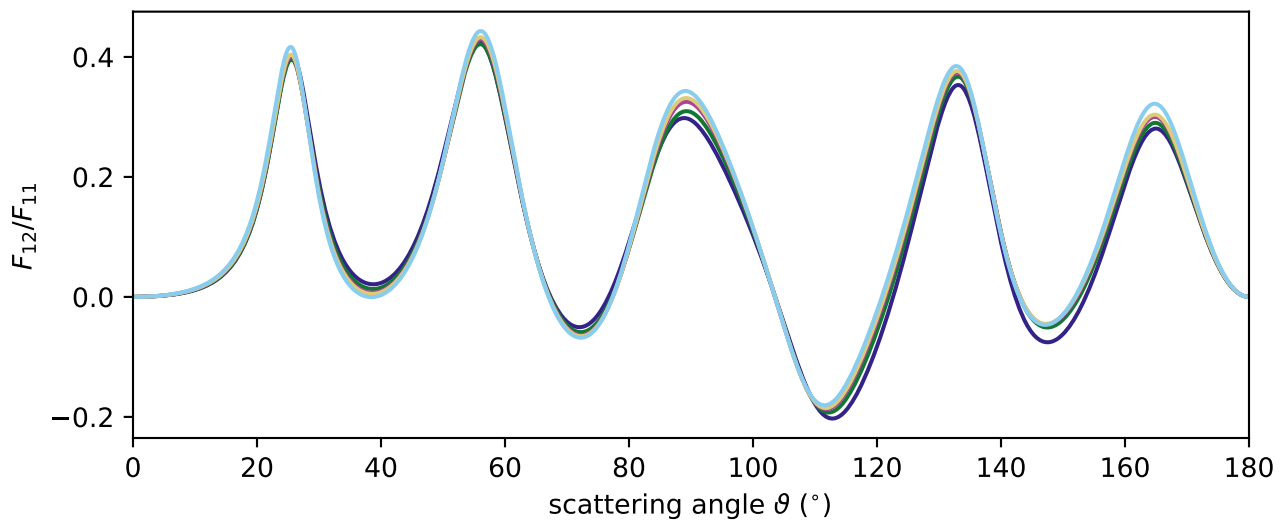
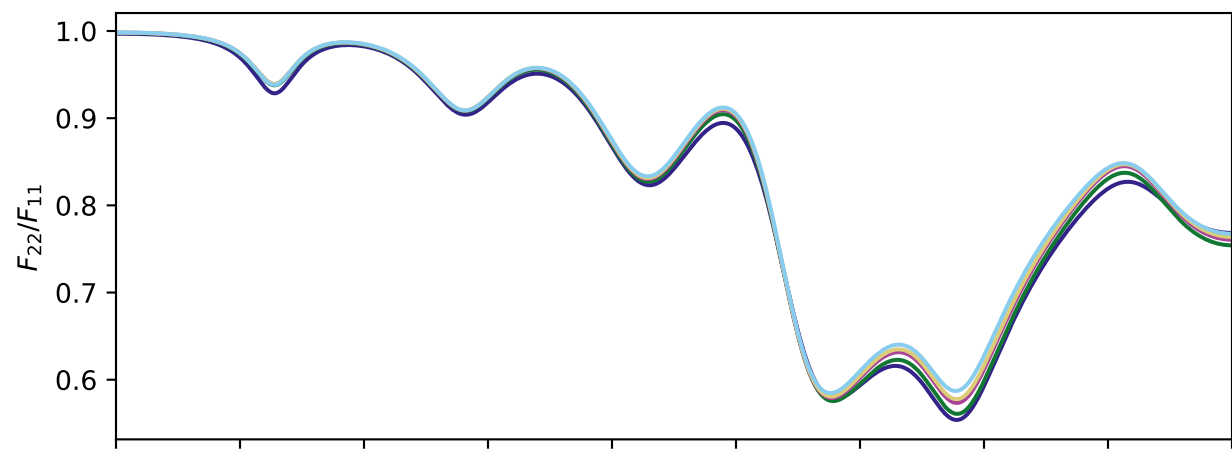
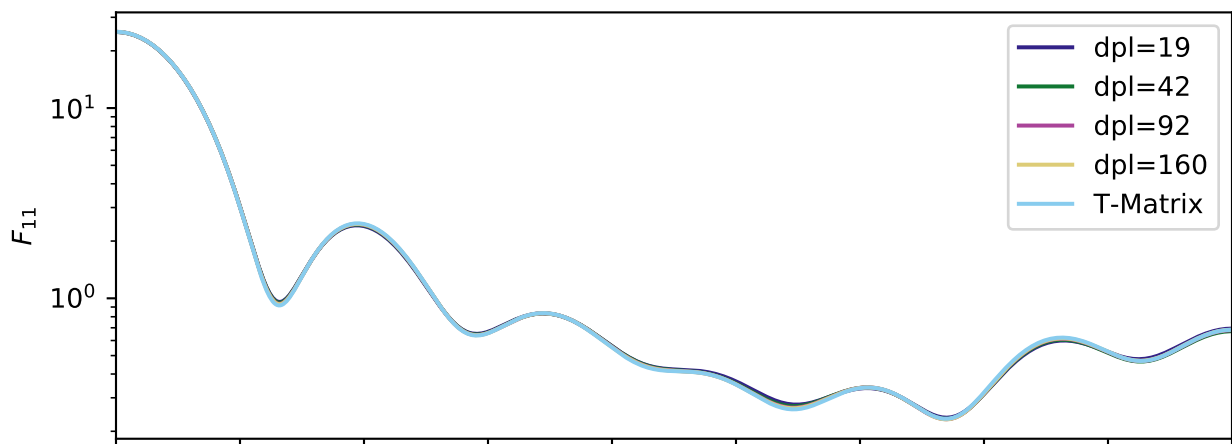


Figure 6.

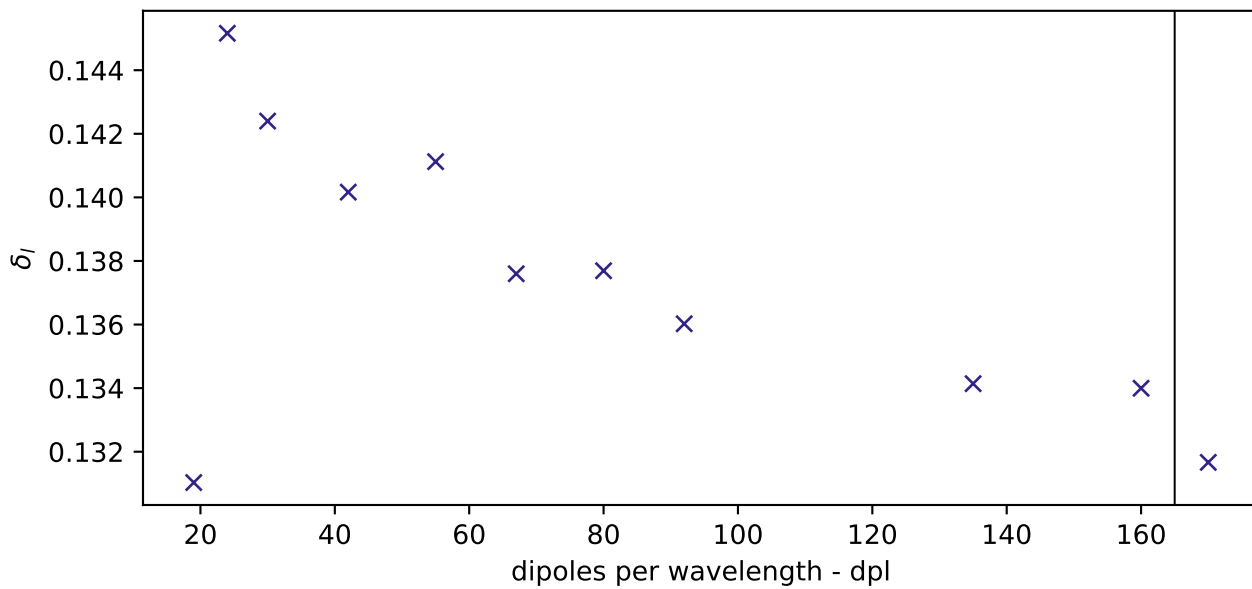
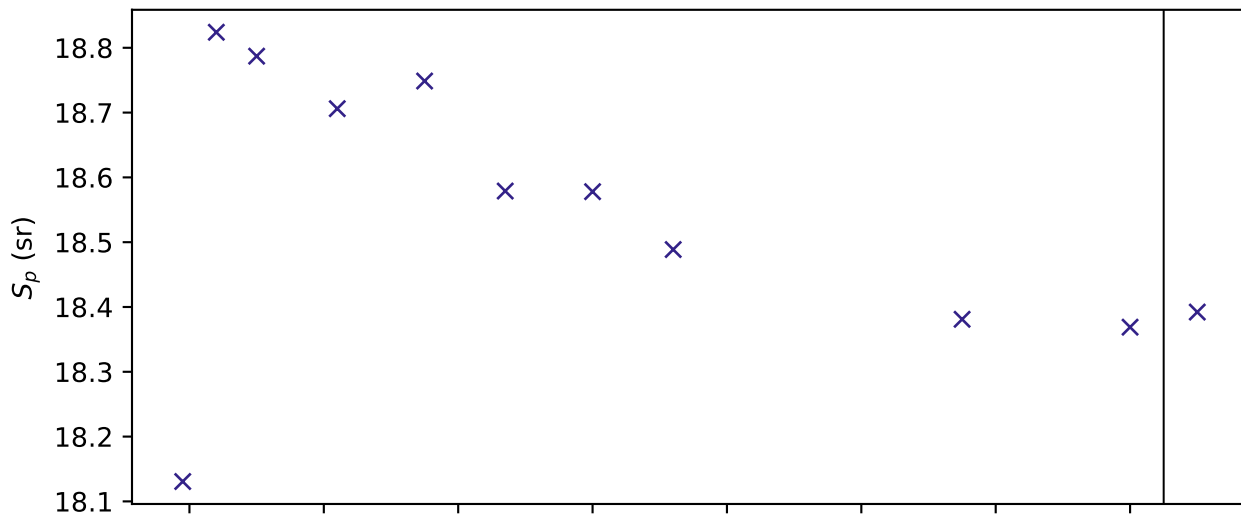


Figure 7.

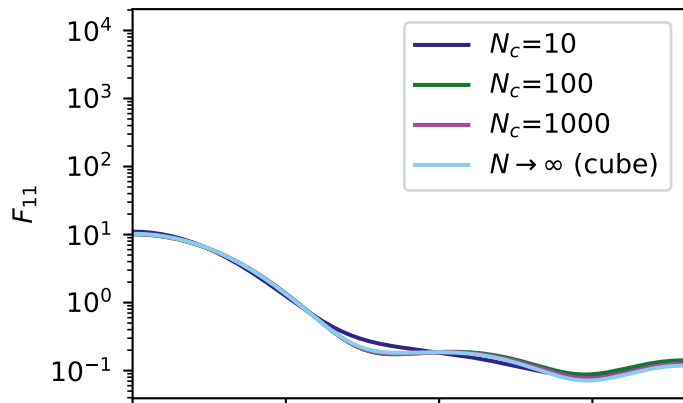
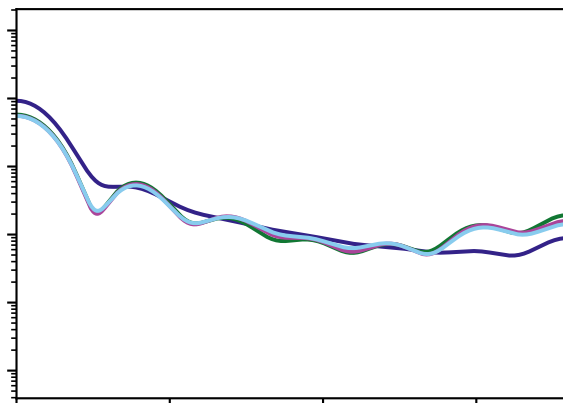
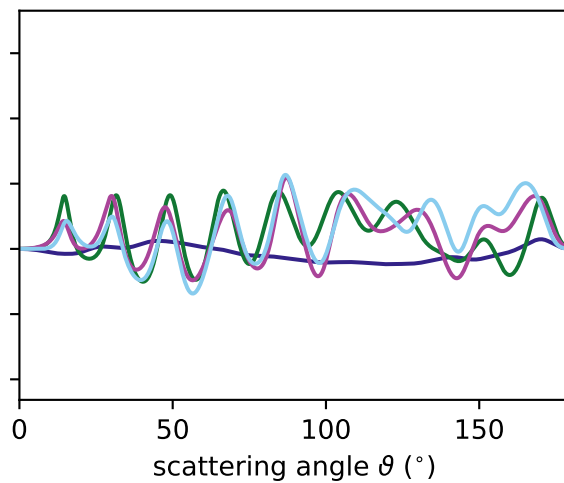
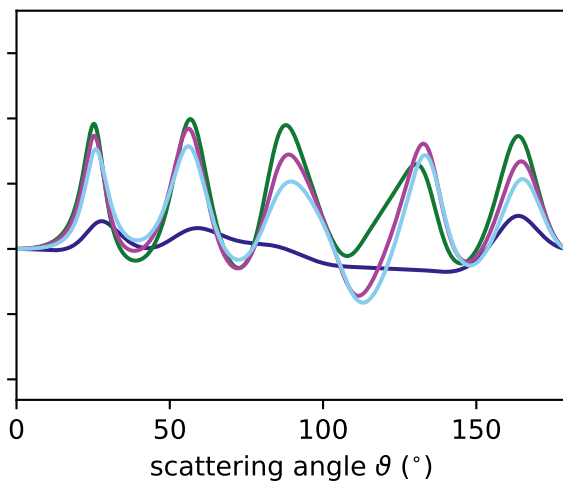
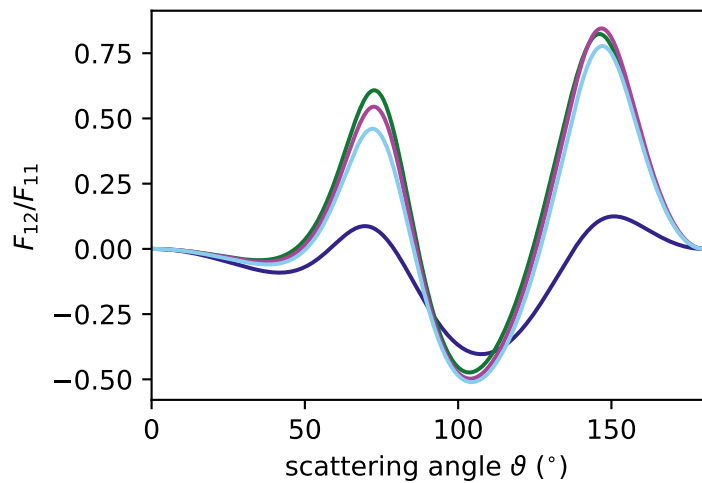
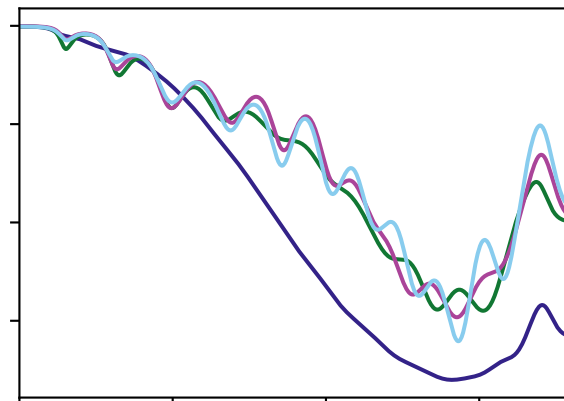
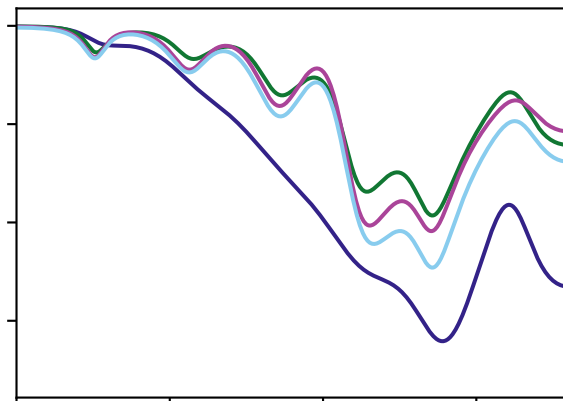
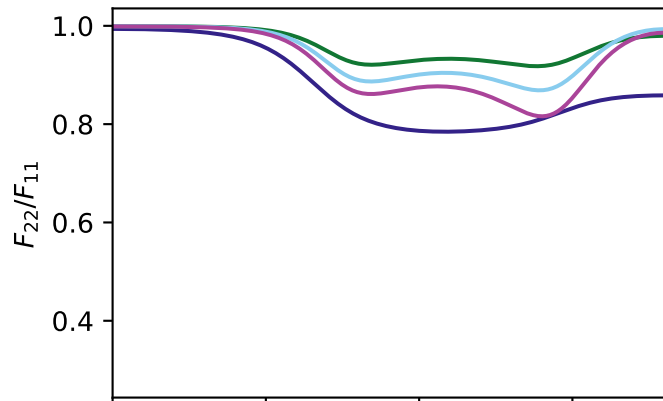
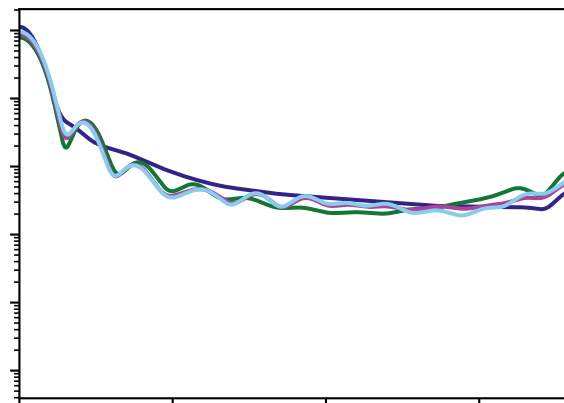
$r_{ve}=0.25\ \mu\text{m}$  $r_{ve}=0.5\ \mu\text{m}$  $r_{ve}=1.0\ \mu\text{m}$ 

Figure 8.

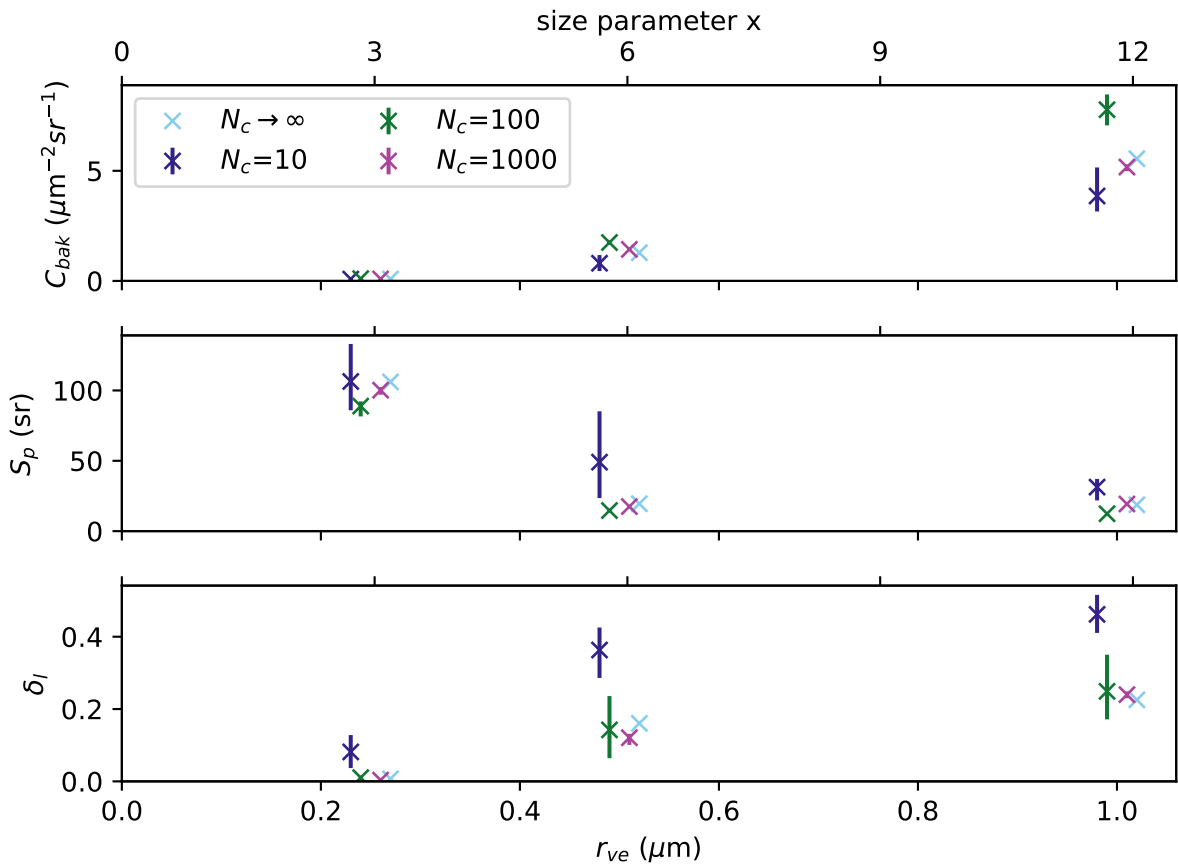


Figure 9.

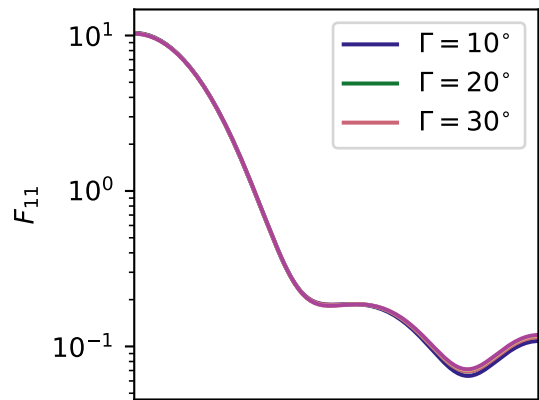
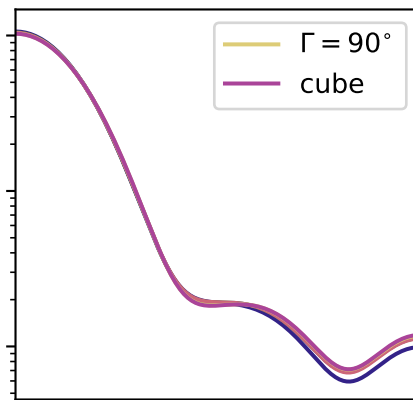
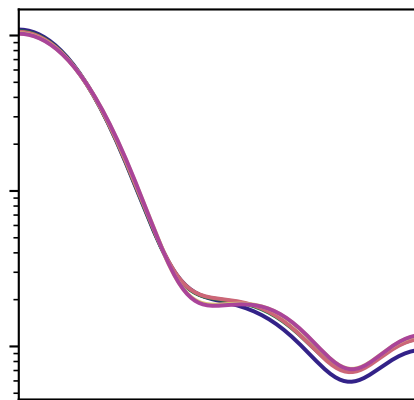
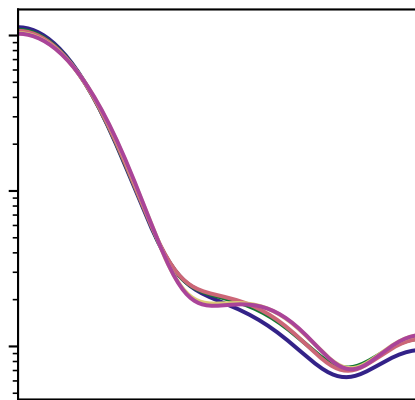
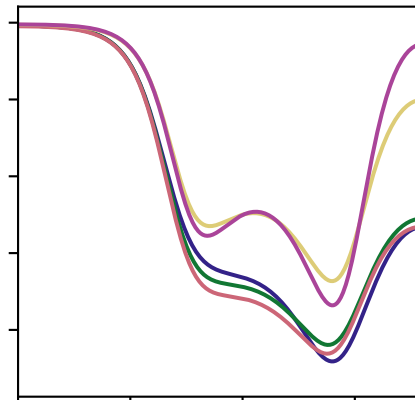
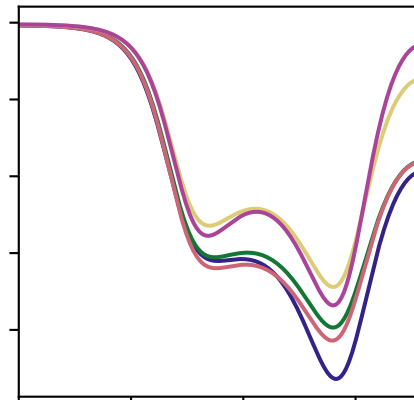
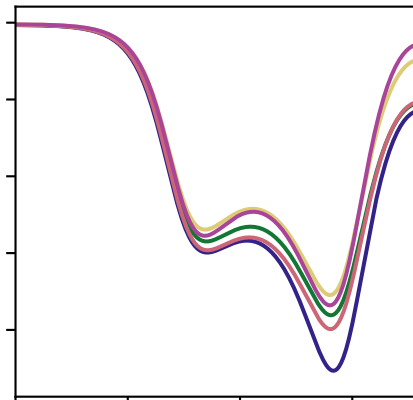
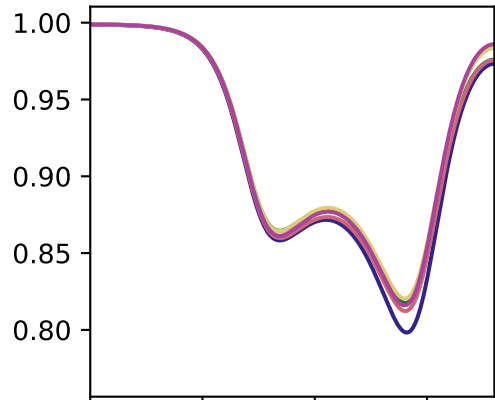
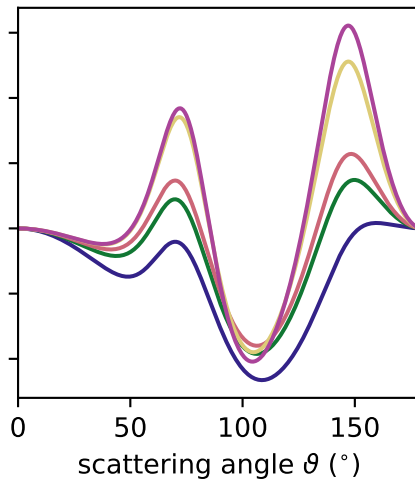
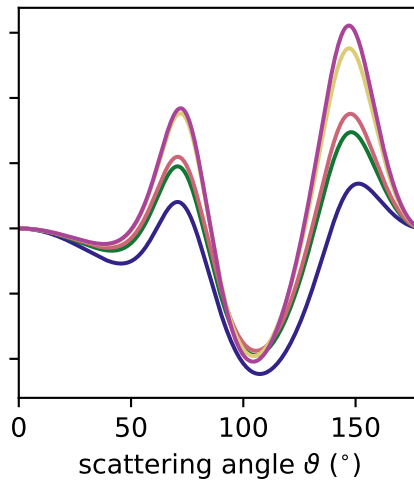
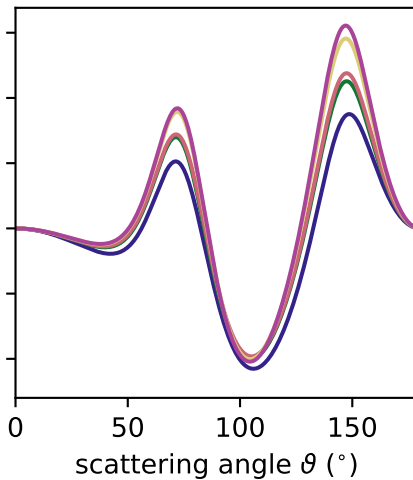
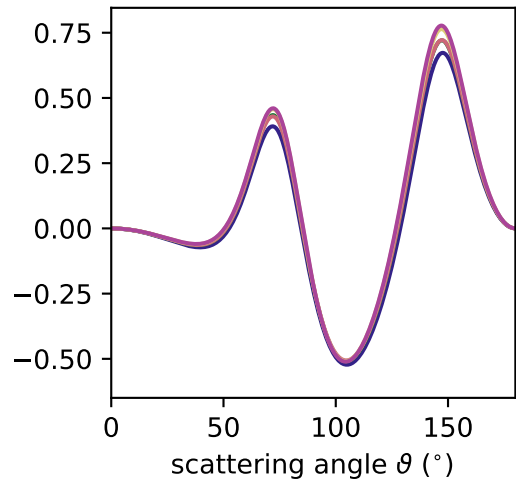
$\sigma = 0.05$  $\sigma = 0.10$  $\sigma = 0.15$  $\sigma = 0.2$  F_{22}/F_{11}  F_{12}/F_{11} scattering angle θ ($^\circ$)scattering angle θ ($^\circ$)scattering angle θ ($^\circ$)scattering angle θ ($^\circ$)

Figure 10.

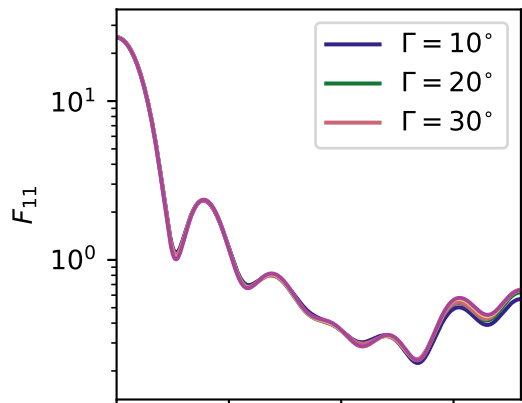
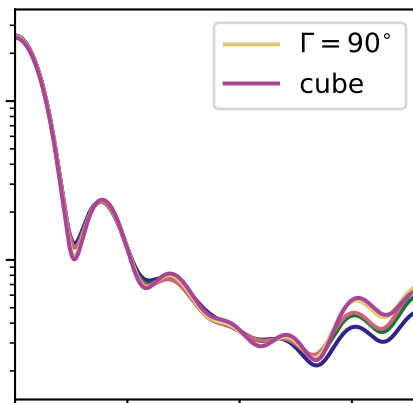
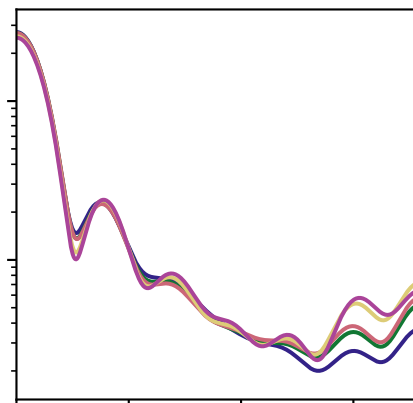
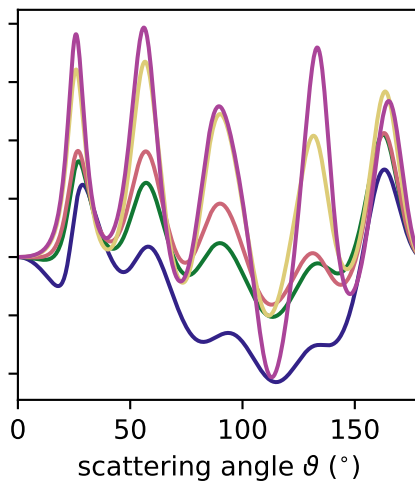
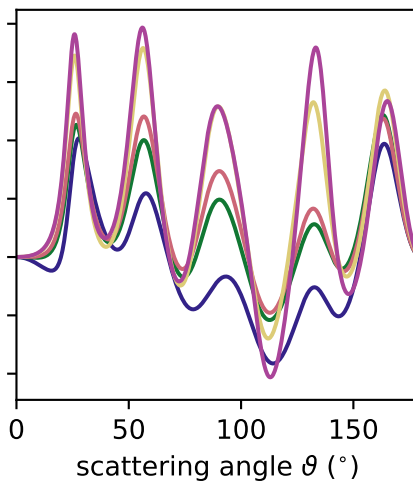
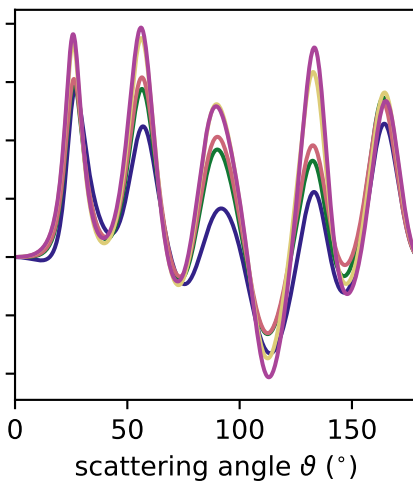
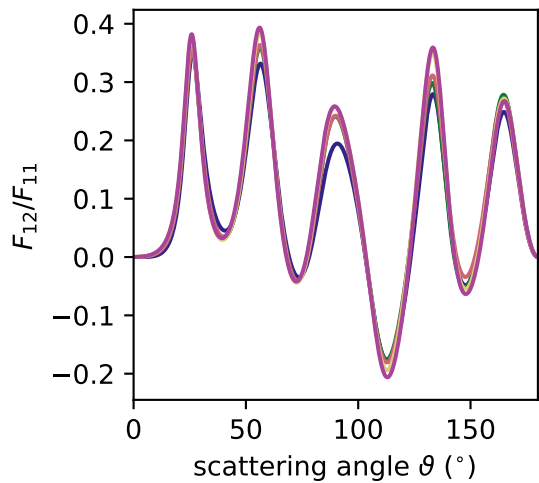
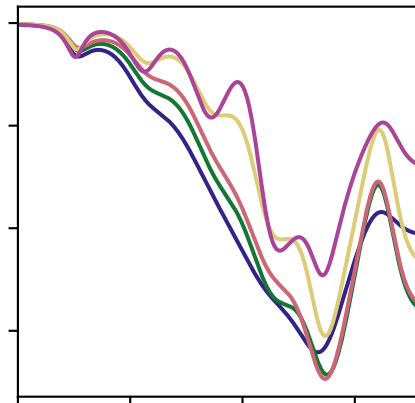
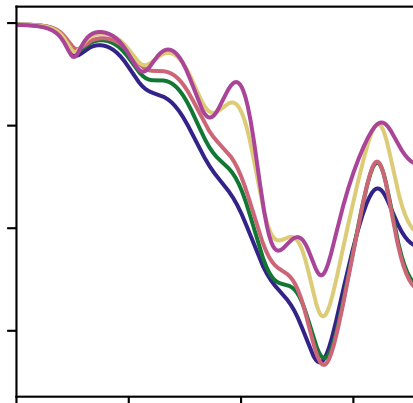
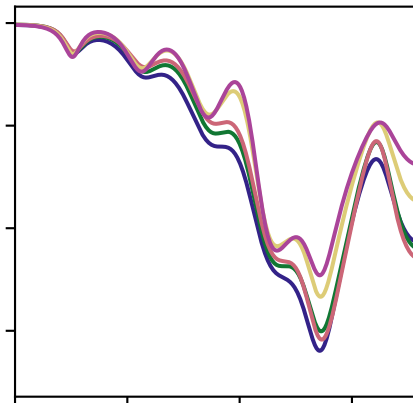
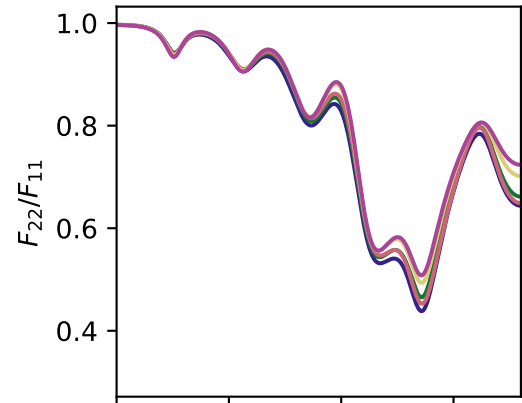
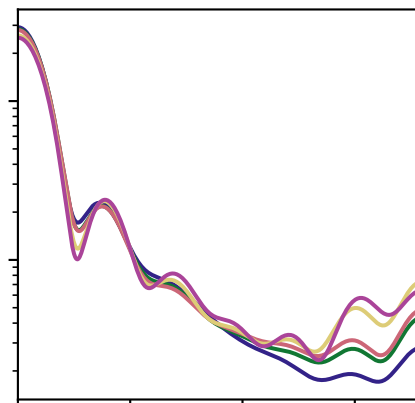
$\sigma = 0.05$  $\sigma = 0.10$  $\sigma = 0.15$  $\sigma = 0.2$ 

Figure 11.

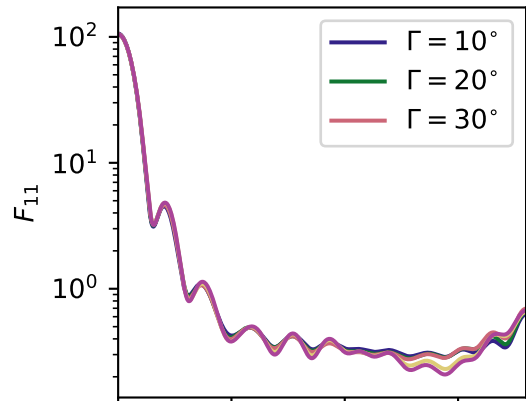
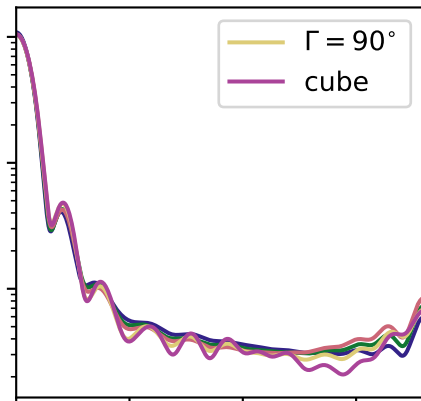
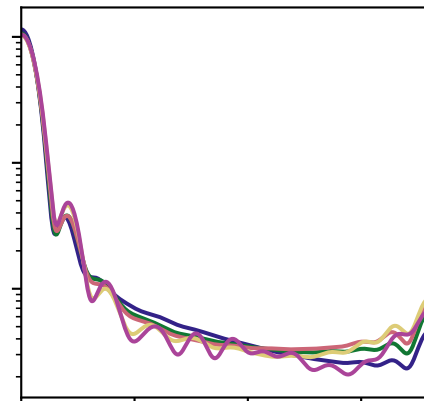
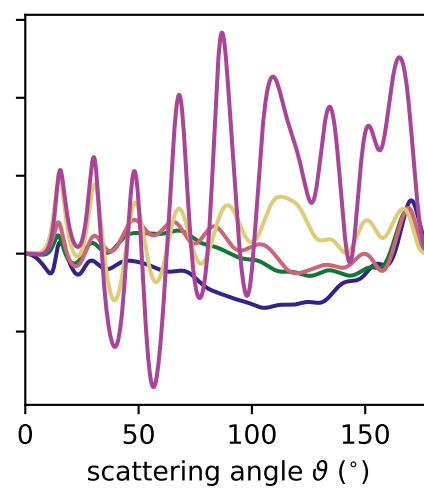
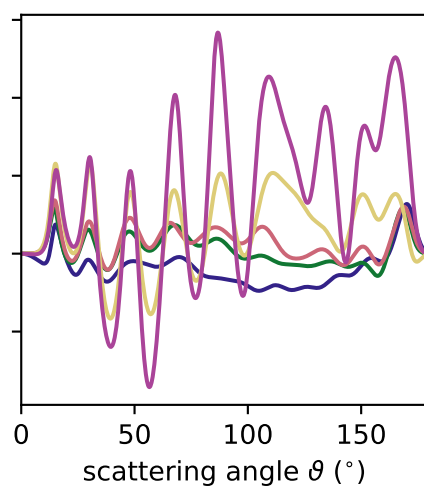
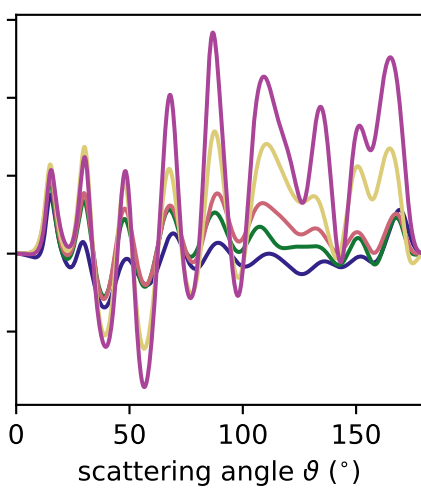
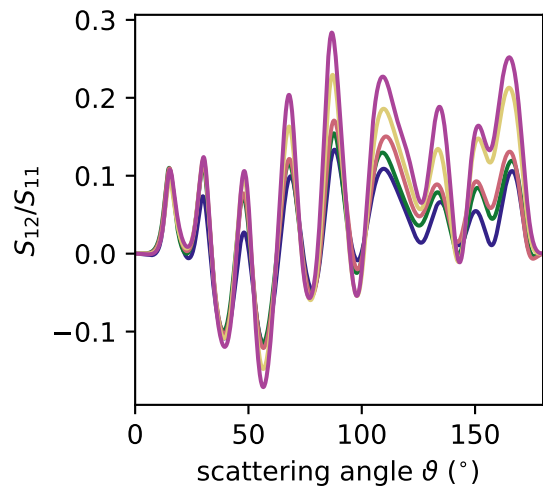
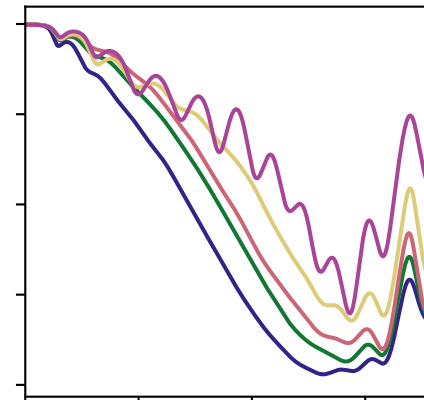
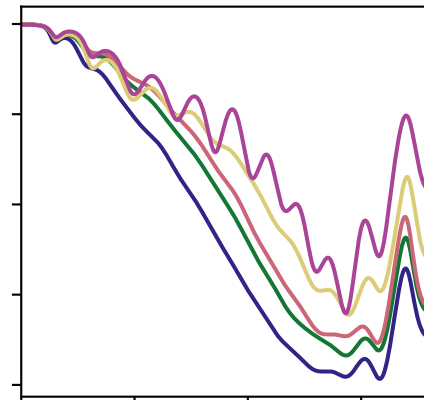
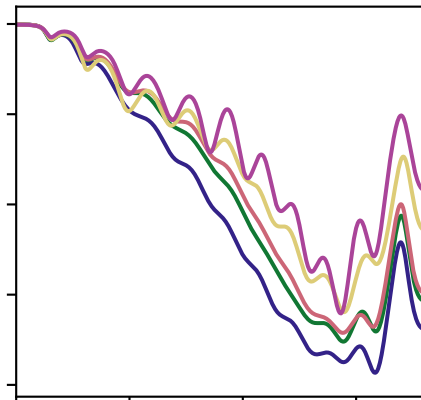
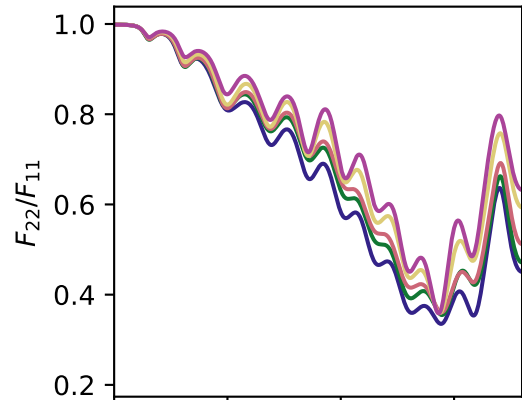
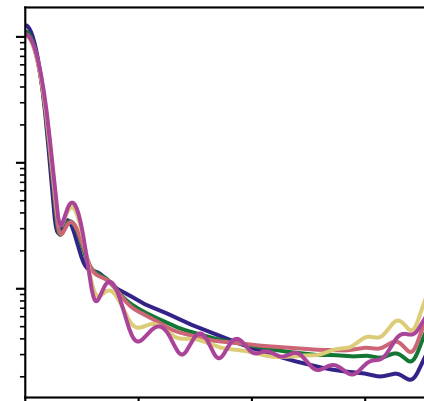
$\sigma = 0.05$  $\sigma = 0.10$  $\sigma = 0.15$  $\sigma = 0.2$ 

Figure 12.

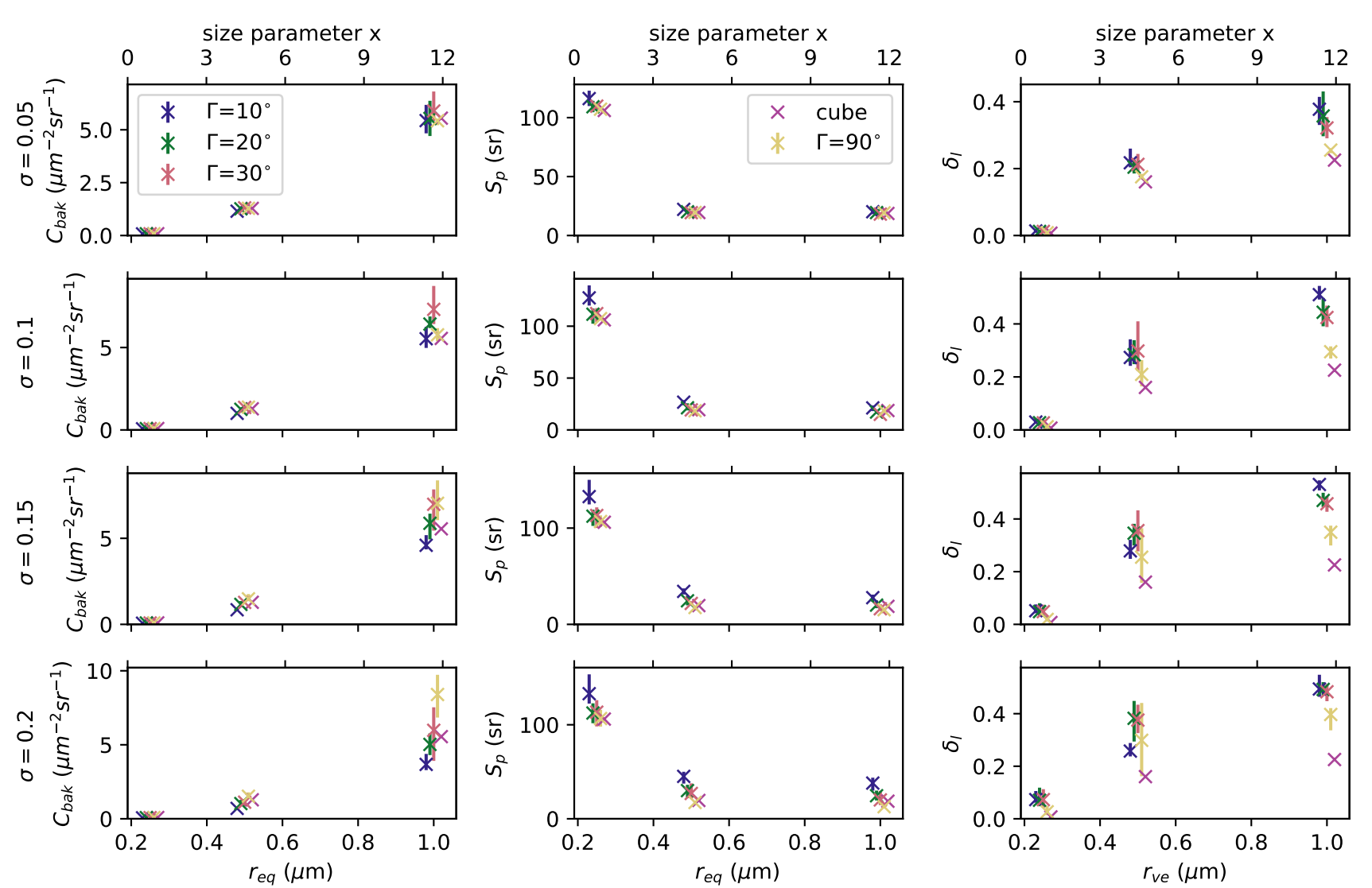


Figure 13.

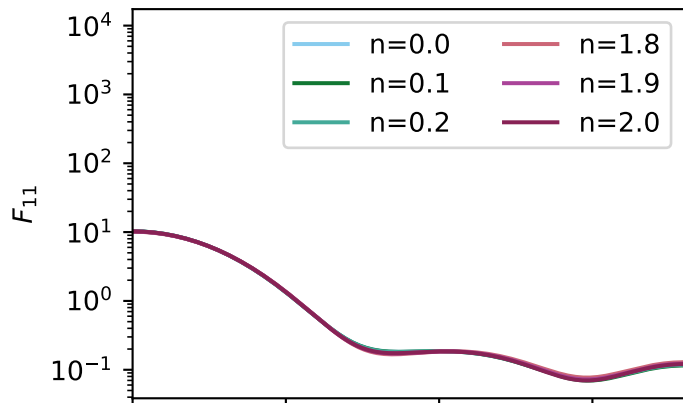
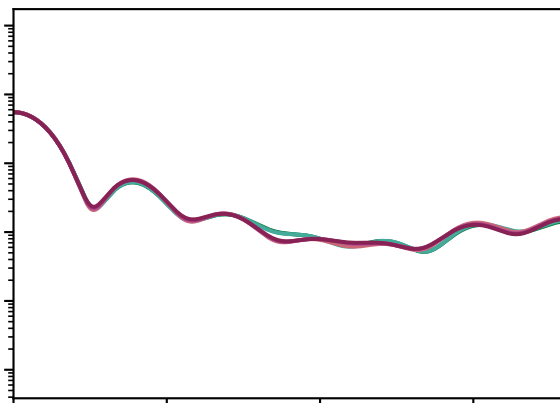
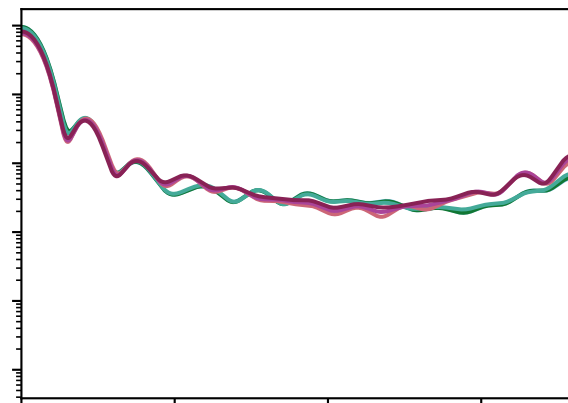
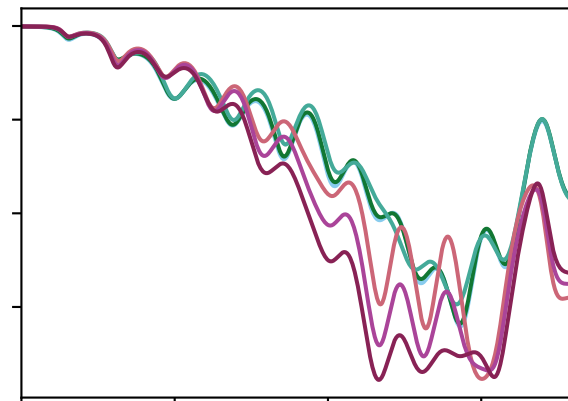
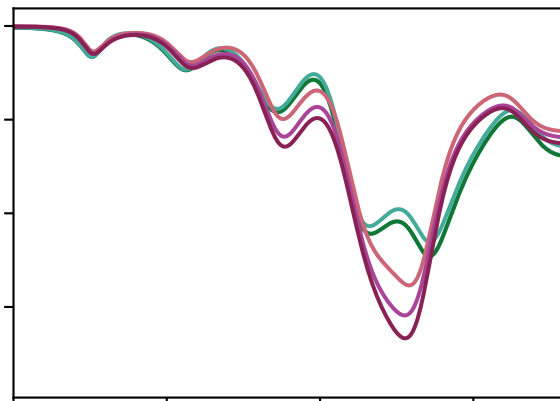
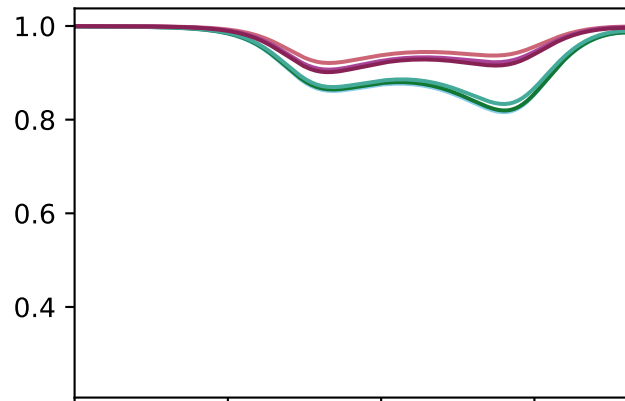
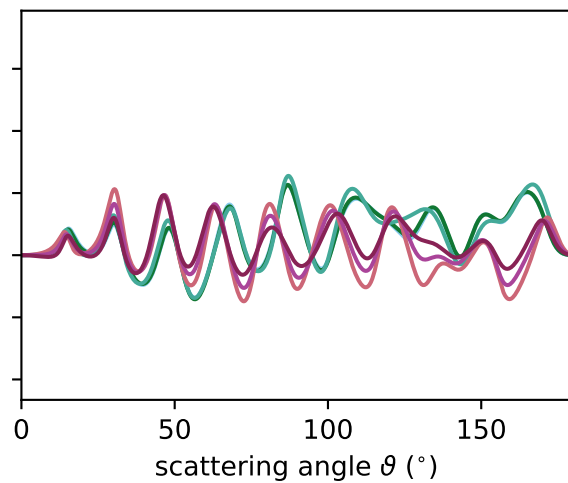
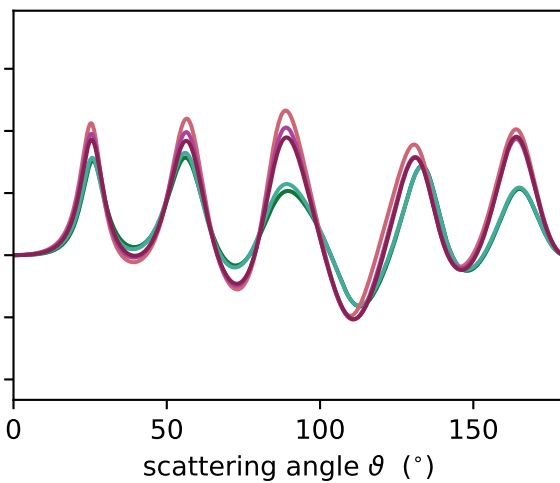
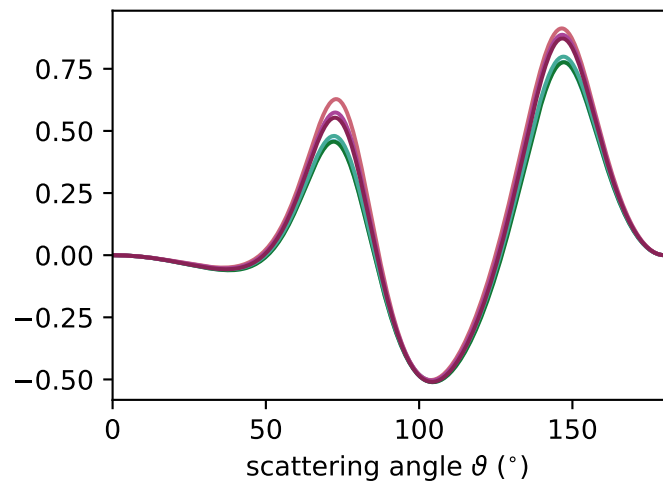
$r_{ve} = 0.25 \mu\text{m}$  $r_{ve} = 0.5 \mu\text{m}$  $r_{ve} = 1.0 \mu\text{m}$  F_{22}/F_{11}  F_{12}/F_{11} 

Figure 14.

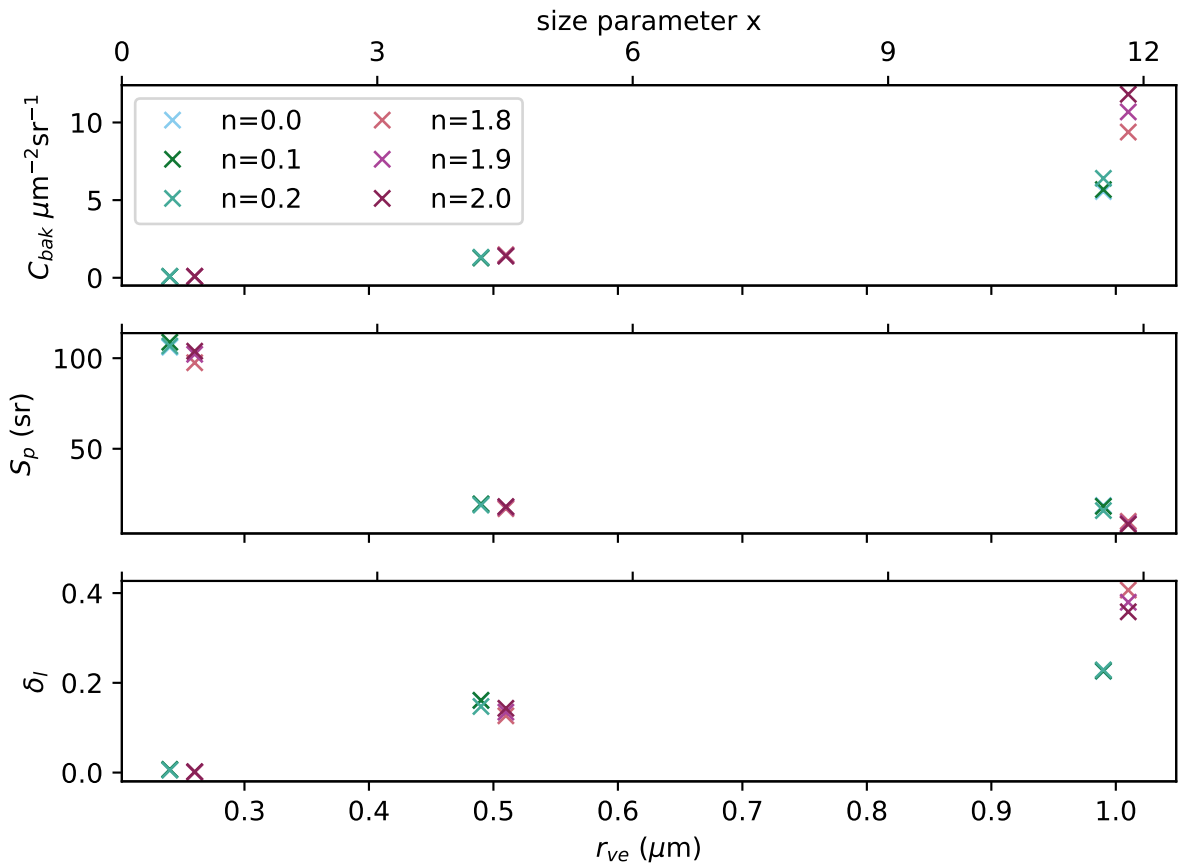


Figure 15.

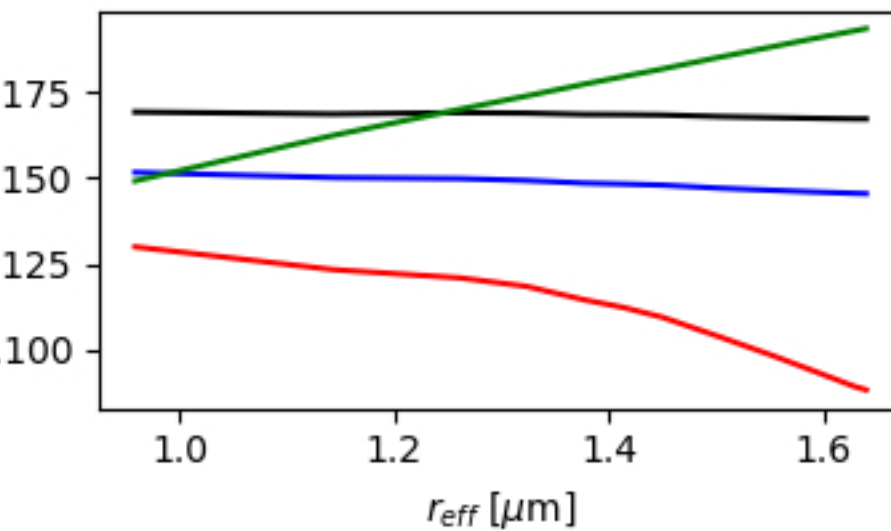
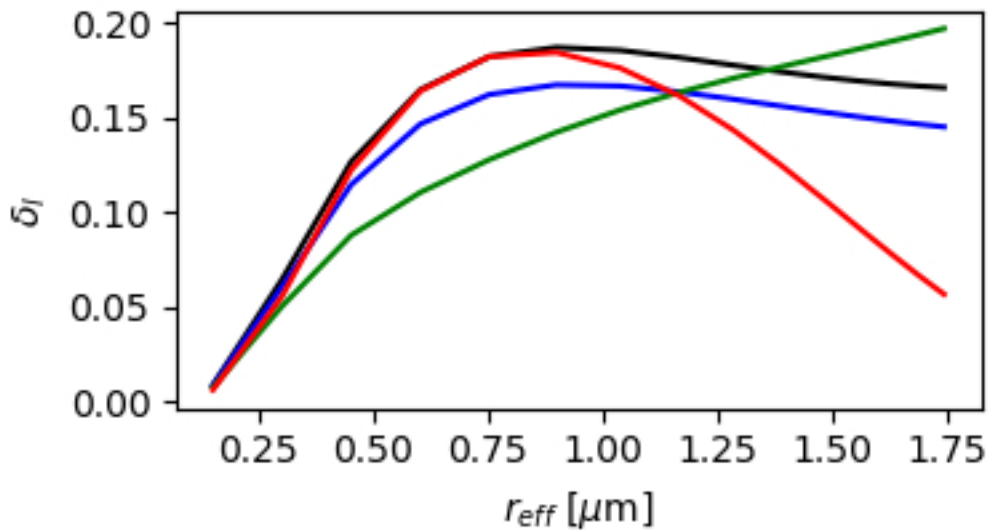
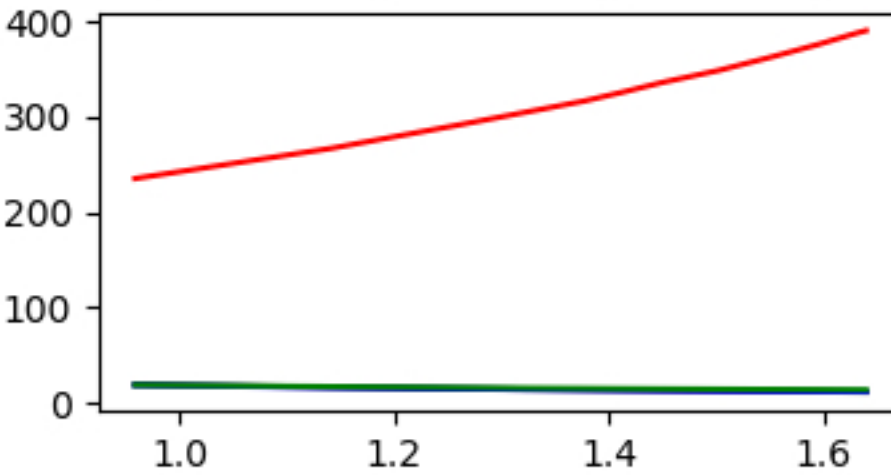
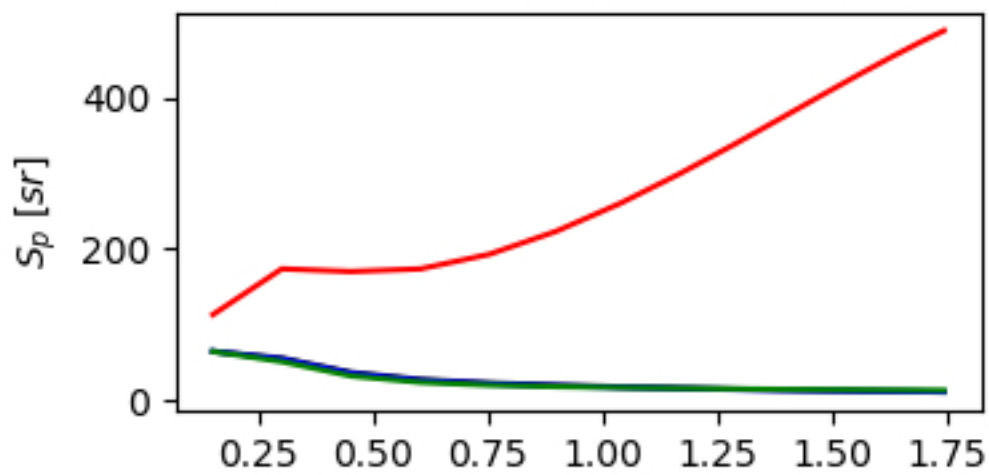
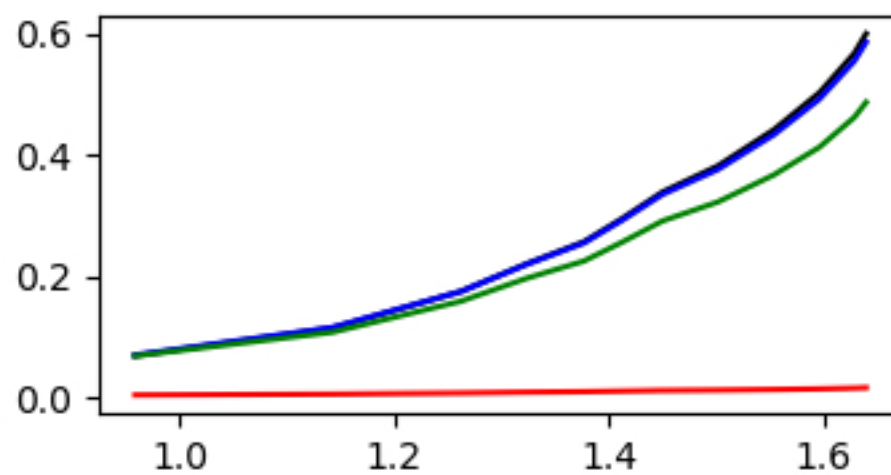
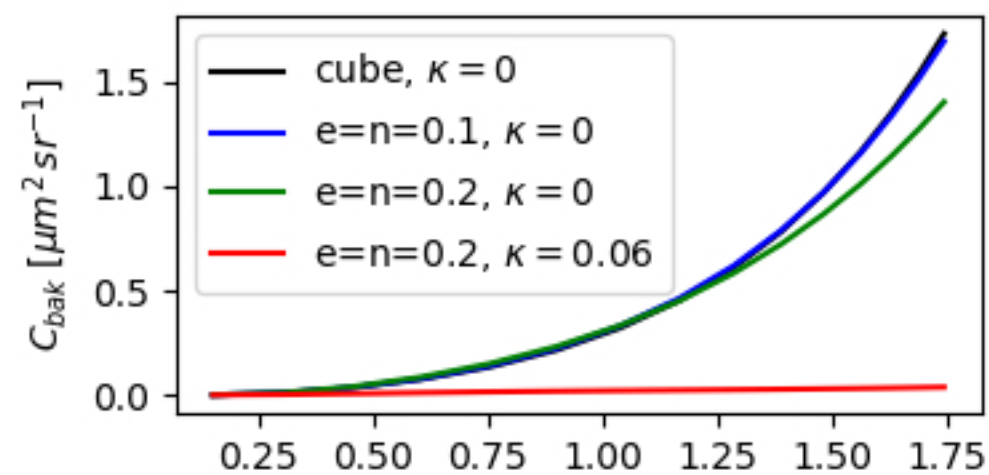


Figure 16.

